An Experimental Study of Hydrodynamic Forces on Cylinders and Cables in Near Axial Flow

Dr. ing. thesis

Svein Ersdal

Trondheim, September 15, 2004

Department of Marine Technology
Faculty of Engineering Science and Technology
Norwegian University of Science and Technology

Acknowledgments

This work have been carried out under the supervision of Professor Odd M. Faltinsen at the Department of Marine Hydrodynamics, Norwegian University of Science and Technology, whose guidance and comments have been highly appreciated. I would also like to thank him, Professor Asgeir Srensen, Professor Carl M. Larsen and the staff at the department of Marine Hydrodynamics for their enthusiasm and ingenuity with regard to additional funding. This also goes for Kjell Holden at MARINTEK.

The experiments could not have been conducted without the help of the staff in the laboratories at NTNU and MARINTEK. I would especially like to mention Knut Arne Hegstad and Torgeir Wahl for their enthusiasm and guidance in setting up the experiments.

Thanks also to family, friends and colleagues for your contributions and encouragement during this time.

This work is part of the Strategic University Program in Marine Cybernetics, sponsored by the Research Council of Norway. Funding is also received from the Strong Point Center on Hydroelasticity funded by NTNU and MARINTEK.

Abstract

The present thesis addresses the hydrodynamic forces on cylinders where the angle between incoming flow and the cylinder axis is low. The normal viscous force is expressed in terms of this angle, called the angle of attack, rather than in terms of the normal component of the incoming velocity which is more common for large angles of attack.

Measured results for a rigid cylinder with length to diameter ratio of 40 towed at constant angle of attack are used to discuss the applicability of suggested methods like the cross flow or the 2D+t principle. The results indicate that for large angles the independence principle holds, but the drag coefficient used for the transverse flow do depend on the Reynolds number of the longitudinal flow. This is particularly the case for the drag crisis known from a cylinder in 2D cross flow. The importance of the flow pattern initiated at the nose of the cylinder is clearly illustrated in these results where the forces on the cylinder increased significantly when an asymmetric vortex pair was initiated.

By oscillating the cylinder in a transverse direction while towing it in the axial direction, the force coefficient in the case of oscillating angle of attack was found. The reduction in added mass known for cylinders in 2D cross flow at small KC numbers are shown to disappear when an axial flow component is present. At the highest tow speed, also the drag coefficient becomes independent of the KC number. For small amplitudes the drag is better modeled by the sine of the angle of attack, rather than the square of the sine associated with the quadratic drag term in Morison's equation.

A combination of linear and quadratic dependence on the sine of the angle is used to model the response of a flexible cylinder with forced oscillation of the tow point. The result is compared to experimental result for a flexible cylinder with length to diameter ratio of 1100 and Reynolds numbers in and above the critical range. The linear term are found to be 8-10 times larger than the skin friction coefficient normally used for this term in modeling of cables. The cylinder is simulated in time domain with a Finite Element Method with second order elements. As an example of practical application of the model, the response of a part of a full scale streamer subject to irregular waves and a control device is investigated. In realistic sea states the response is found to be rather small, but not damped by the control device.

Contents

Nomenclature

General

- Symbols are generally defined where they appear in the text for the first time.
- Only the most frequent use of symbols are listed here
- Matrices are represented by bold characters, e.g $\boldsymbol{A}$
- The vector symbol $\vec{a}$ is used for vectors in space only. Other vectors are represented by bold characters.
- Overdots signify differentiation with respect to time, e.g $\dot{a}$, $\ddot{a}$
- Superscript prime is used for differentiation with respect to coordinate along cable.
- Subscripts t, n, and b denotes tangent, normal and bi-normal directions in local coordinate system
- Subscripts x, y, and z denotes directions in global (non accelerating) coordinate system.
- Subscript 0 normally indicates the amplitude of an oscillating parameter. Subscript pp denotes the peak to peak amplitude.

Abbreviations

BVP	Boundary Value Problem
2D	Two dimensional
2D+t	Two dimensional plus time. Also known as $2\frac{1}{2}$D
3D	Three dimensional
DOF	Degrees of freedom
FEM	Finite Element Method
VIV	Vortex induced vibrations

Roman letters

a	sectional added mass per unit length
a_j	sectional added mass of node or element j
A, A_0	position amplitude
$\boldsymbol{A}$	added mass matrix
B	Bias error limit, usually with subscript identifying source
C_a	added mass coefficient
C_b	bi normal force coefficient
C_D	Drag coefficient of body
C_d	drag coefficient, sectional or 2D
C_f	local friction coefficient, based on area
C_F	averaged friction coefficient, based on area
C_n	normal force coefficient per unit length
C_t	tangent force coefficient per unit length
d	diameter
e	error
e_r	relative error
e_{diff}	The standard error of estimate which expresses the difference of measured and calculated values.
e_{mod}	modeling error.
e_{exp}	measurement error.
f	any scalar function
F_j	Force in direction j (scalar)
$\vec{F}$	Force vector in space
$\boldsymbol{F}$	Force vector in general
KC	Keulegan Carpenter number, $KC = \frac{V_0 T}{d}$
L	total length
m	sum of structural and added mass per unit length
m_j	sum of structural and added mass of node or element j
$\boldsymbol{A}$	mass matrix
q	structural mass per unit length
$\boldsymbol{Q}$	structural mass matrix
$\vec{r}$	position vector in global coordinate system
P	Precision limit, usually with subscript identifying source
R_e	Reynolds number
R_{ed}	Reynolds number based on diameter of the cable
R_{eL}	Reynolds number based on length of the cable
S	Standard deviation estimate, usually with subscript identifying source
s	curvilinear coordinate along the cable. Also used for non-dimensional time in 2D+t principle
t	time variable. Also used for weight specifying confidence interval
T	Tension, but also used for period
u, v, w	velocities in local coordinate system
U	tow or vessel speed (scalar)
V	relative velocity between cable section and surrounding fluid(scalar)
$\vec{V}$	relative velocity vector
w	weight per unit length

Greek Letters

α	’angle off attack’, the angle between the incoming fluid and the tangential direction of the cable or cylinder
κ	Influence coefficient
ϕ, θ, ψ	orientation angles of local coordinate system, usually euler angles
ρ	density of water
ν	dynamic viscosity of water
ω	circular frequency. Unit radians per second is denoted s^{-1}.

Chapter 1

Introduction

1.1 Background and Motivation

Marine seismic surveying is a method to map subsurface topology and geological structures. The method is mainly used in offshore oil production, both for exploration of possible areas containing oil and gas and more detailed studies in the field development and production phase. The basic configuration is given in figure 1.1. A more detailed description of such systems can be found in Pedersen (1996) and only a short summary will be given here. The survey system consists of a tow vessel, a lead-in system, an acoustic source and one or more streamers. The tow vessel is most often purpose built and range from designs based on trawlers to novel designs like the Ramform. Acoustic sources are most often based on air guns mounted on some kind of floats towed close behind the towing vessel. The hydrophones used to register the reflected acoustic signal are located in so called streamers towed in parallel, usually 3-8000 m long. In addition to hydrophones, the streamers contains signal cables, tension members, buoyancy devices and in some cases power and control lines for the depth control devices. From a modeling point of view the streamer is considered a fully flexible cylinder which do not carry any bending moment, in other words a cable. Configurations from a single streamer and up to 16 streamers towed in parallel are used. The depth and distance between the tow points of the streamers are kept by a system of tow lines, deflectors and floats, denoted lead-in in figure 1.1. In the downstream end of each streamer a tail buoy provides tension and navigation aids. Depth control devices in the form of small controllable wings are distributed along the streamer. Normally these only allow control of the tow depth of the streamer by a local PID controller, but new systems like the *Q-fin* system by Western Geco Inc allows global control also of the horizontal position.

For design and tuning of such control systems, simulation is a very useful tool. Mathematical models of the system can also be used in observers, improving the robustness and accuracy of the position measurement of the hydrophones. Simulation is also used for personnel training both for special operations like deployment and retrieval of the towed hardware and for normal operation. Since acquisition requires towing the streamers in a straight line, the time

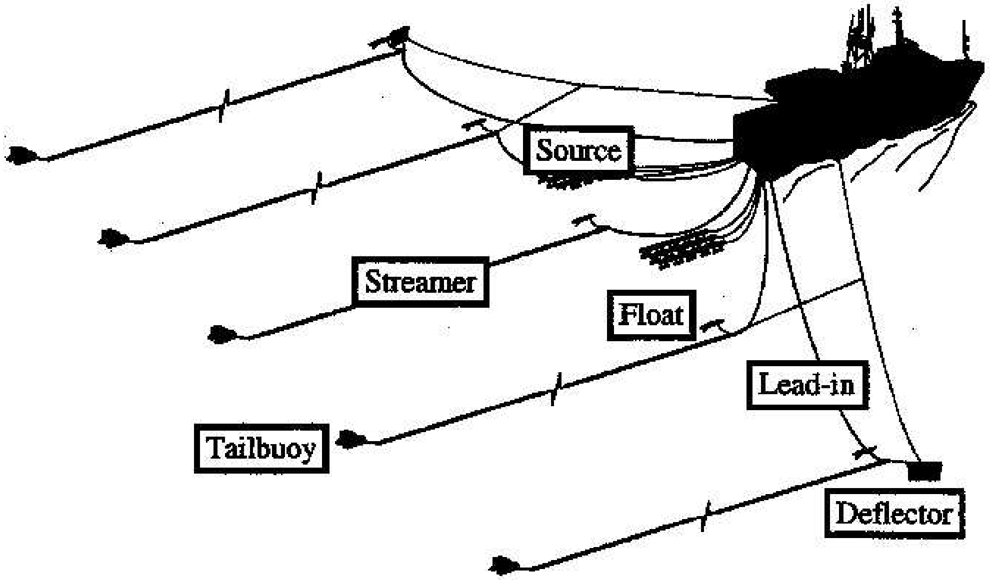

Figure 1.1: *Towing configuration for 3D marine seismic surveys using a single vessel towing two acoustic sources and five streamers.*

spent turning the survey system around between runs should be reduced as much as possible. Simulation of the system could be used to optimize the turn. Also, Pedersen (1996) reported large oscillations in the vertical direction for some cases during full scale measurements. A simulation model of the system could be used to find the cause of this as done by Pedersen and Sørensen (2001) with a very simple model of the streamer.

A major obstacle in developing reliable and effective models of a seismic survey system is to model the hydrodynamic forces on the streamers correctly. The flow around the streamer is dominated by flow in the axial direction, in contrast to other highly flexible marine structures like risers where the dominating flow is across the cylinder. A result of this is the importance of friction force on the tension in the streamer, which again is important for the transverse motion. On the other hand, the effect of the axial flow on the forces normal to the streamer axis is not fully known, since it is suspected that the cross flow principle normally used for slender marine structures is invalid when axial flow is dominating. This is here denoted the near-axial flow regime.

The objective of this work is then to evaluate and possibly improve models of the hydrodynamic force on a towed streamer. Since some applications like observers requires that simulation can be performed in real time or faster, the emphasis is on models that do not require modeling of the flow field around the streamer. Tools like Computational Fluid Dynamics (CFD) are therefore not applied, rather the emphasis is on applying experimental results in a general formulation.

1.2 Previous work

The literature on towed cable systems can be roughly divided in two: Stability of a towed array, or streamer, and modeling of a tow fish system. The former is the most applicable for the modeling of a streamer, but unfortunately the main focus have been on military applications (typically sonar arrays towed by submarines) and unclassified publications are rare. The linearized equation for the transverse motion of a towed flexible cylinder was published by Paidoussis (1966) and with corrections in Paidoussis (1973), and is known as the Paidoussis equation. This equation assumes small amplitude of motions, linear distribution of tension and that the cylinder is neutral in water. See also the series of articles by Paidoussis, Grinevich, Adamovic, and Semler (2002), Lopes, Paidoussis, and Semler (2002),and Semler, Lopes, Augu, and Paidousssis (2002) where the equation is extended to higher order and bending resistance is included. The main application is to study the stability of a towed flexible beam with a free end. Dowling (1988) discussed the solution and stability for a towed cable with a free end based on this equation. In both cases the hydrodynamic force is based on a linear model suggested by (Taylor 1952) for turbulent flow. The development of the Paidoussis equation is given in chapter 6.

An important finding in these analysis is that for a free, tapered end the cable may become unstable and oscillations of the free end are introduced. At some point toward the end of cable the tension, which is created by friction forces along the cylinder, becomes to small to balance the unstable part of the hydrodynamic forces. In this case a singularity is introduced in the Paidoussis equation and some moment resistance must be introduced at least locally to obtain a solution. In the case of a streamer it will be assumed that sufficient tension is applied at the downstream end to avoid this singularity. After all, this is the main reason for having an aft float attached to the streamer.

The formulation and problem setup here is mainly based on Kennedy (1987) and Triantafyllou and Chryssostomidis (1988). Both study the response of a long and thin flexible cylinder subjected to forced motion of the tow point and with an applied tension in the downstream end. No bending resistance is included. The former keeps the linear formulation of the hydrodynamic force coefficient, but the coefficient is much higher than suggested by Taylor. This is based on experimental result, but it has not been possible for this author to obtain details of these experiments. Triantafyllou and Chryssostomidis (1988) studies the same kind of problem, but adds a non-linear term to the hydrodynamic normal force. In both cases the response is a wave propagating along the cable in the downstream direction. For high frequencies the amplitude of the wave is reduced, so that the cable acts as a low pass filter for upstream disturbances. By including the nonlinear term the downstream response was found to approach zero.

A comprehensive study of seismic system from a more nautical point of view is is given by Pedersen (1996). The example of a streamer in chapter 7 is based on data from this work.

For more general cable systems a comprehensive review is given by Casarella and Parsons (1970) for work before 1970. A very quick summary of this is that the main problem is the hydrodynamic loading were experimental data are sparse. Two different principles for modeling hydrodynamic force is identified. The first uses the angle between the cylinder axis and the incoming flow, similar to Taylor (1952) while the alternative express the forces in terms of normal and tangential components of velocity. In the latter case Reynolds number are accounted for. More resent work seems to concentrate on the solution of the partial differential equations. Here the cable is discretized either in a physical or mathematical sense to create a system of equations solvable on a computer. Physical discretization usually divides the cable in straight, rigid segments connected at nodes. Examples are given by Winget and Huston (1976), Sanders (1982) and Vaz and Witz (1997). The alternative is to write the equation of motion for a continuous cable and then discretize the result. Possible schemes are the finite difference method, e.g. Ablow and Schechter (1983), Hover (1997) or the finite element method, (Bhattacharyya, Vendhan, and Sudarsan 2000; Aamo and Fossen 2000; Türkyilmaz 2003). In chapter 7 the finite element method is used to simulate Paidoussis equation with non-linear hydrodynamic forces. A different approach is suggested by Hover, Grosenbaugh, and Triantafyllou (1994) where the problem is divided in a static and a dynamic part, and the dynamic part is linearized.

1.3 Present work

The present work focuses on how to model the hydrodynamic force when the local angle of attack is small. The local angle of attack is the angle between the axis of the cylinder and the relative fluid velocity vector. The hydrodynamic forces includes all forces acting on the cylinder by the fluid, due to the relative motion between them. This force is in general divided in a part due to potential flow effects, like the added mass, and a viscous part due to skin friction and separation of flow.

After presenting some background on steady and unsteady flow on slender bodies and cylinders, chapter 2 also presents concepts and methodology for error analysis of experiments and numerical models in some detail, with emphasis on the use of both bias and precision errors in the analysis. To this author's knowledge the extensive application of this methodology in the following chapters is quite unique to this work.

The following two chapters discusses the normal forces on a rigid cylinder. First it is towed at a constant angle of attack so that the local angle is constant both in position and time. Chapter 3 describes the experiment and results for this case. The main findings is that there are at least two possible flow regimes for angle of attack between zero and twenty degrees. Due to the shape of the upstream end asymmetric vortex shedding occurred for very low angles in some cases. In addition to creating a bi-normal force this also increased the normal force on the cylinder. Possible models of the force are discussed. The forces are expressed in a *lift coefficient* form, similar to the expression for lift on a wing section:

$$F_n = C_n(\cdot)\ \frac{1}{2}\rho U^2\ dL$$

Where ρ is the density of the surrounding fluid, U the tow speed and d and L the diameter and the length of the tested cylinder. The force coefficient $C_n(\cdot)$ is in principle a function of several parameters, but most important are Reynolds number, position along the cylinder and angle of attack. Neglecting the Reynolds number and averaging along the length, it can be expressed

$$C_n(\cdot) = C_{n1}\sin(\alpha) + C_{n2}\sin^2(\alpha)$$

The values and physical meaning of these coefficients are discussed. In chapter 4 forced oscillation is applied on the cylinder, and possible force models are discussed. The KC dependence known from a cylinder oscillating in cross flow is discussed, and found to decrease with increased forward speed.

In chapter 5 the attention is shifted to a flexible cylinder. The response due to harmonic oscillation of the tow point was measured for a model setup in the tow tank. Setup, results and measurements errors are discussed. The following chapter presents the linearized model of the transverse motion, the Paidoussis equation. It is developed and extended to include a buoyancy term and non-linear hydrodynamic forces. This model assumes small perturbations of the cylinder in the normal direction, so that also gradients along the cylinder are small. By assuming a harmonic oscillating form of the solution, the problem is transformed to a boundary value problem for the response amplitude and phase along the cylinder. The use of force models found in literature overestimated the results by a factor of two, particularly around the first eigenfrequency of the experimental setup. Applying the results from the rigid cylinder improved this dramatically.

Chapter 7 presents a simulation model of a cable using the finite element method. Here the agreement between model and experiment is at the same level as the uncertainty of the measurements. Finally the model is applied to find the response of a streamer in waves and the effect of depth control devices.

As mentioned above, unclassified experimental data for normal forces on cylinders in near-axial flow are rare. Thus the results and the quality assurance of this data through an extensive error analysis may be the most important contribution of this work. The results and the estimated errors are for this reason given in tables in the appendix.

CHAPTER 2

Theoretical Background

The first part of this chapter introduces some commonly used concepts and approximations for hydrodynamic force models and to some extent discusses their relevance. This will be further discussed based on experimental results in following chapters. The problem to be considered is shown in figure 2.1.

In the following chapters the comparison of experiments and numerical models are discussed at length. An important aspect of this is the uncertainties associated with both experimental and computed results, in this context called measurement and modeling errors respectively. The second part of this chapter introduces methodology and concepts in error estimation, most noticeably for experimental results.

2.1 Hydrodynamic forces on a flexible cylinder in near axial flow

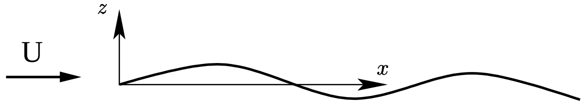

Figure 2.1: *Coordinate system for flexible cylinder in near axial flow.*

The cylinder is assumed to have constant cross sections and to be very long compared to its diameter, $L/d \geq 1000$ is expected for the real case. The coordinate system is moving with constant speed U toward the left, and will normally be the tow speed of the seismic streamer. An element of the cylinder is shown in figure 2.2 where velocity, forces, and angles are defined. Here U is again the tow speed of the cable, while V is the relative velocity between the cable and the surrounding fluid. The angle of attack α is the angle between the relative velocity vector and the cable axis, while the orientation angle θ is the angle between the cable axis and the x-axis. The forces F_n and F_t are written in a local coordinate system for the cable element, rotated the angle θ from the global coordinate system.

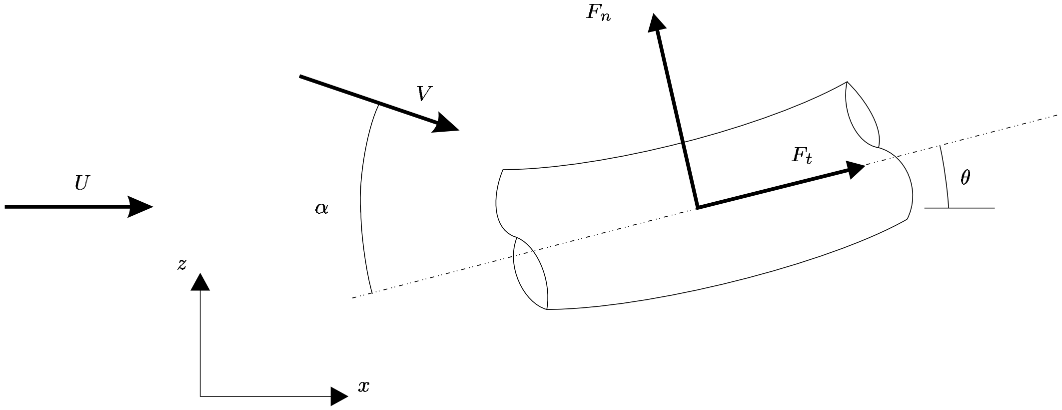

Figure 2.2: *Local element of a flexible cylinder. U and V describes free and relative velocities, F_n and F_t are normal and tangential forces, and α and θ are angle of attack and orientation angles, respectively.*

For a towed seismic streamer it is a reasonable assumption that the displacement in the normal direction is small compared to the length, and that this displacement is slowly varying with x. The last assumption will justify a small angle approximation for the orientation angle θ. This does not necessarily mean that the transverse velocity is small, thus the angle of attack α is not small.

Most of the existing models of hydrodynamic force on a long flexible cylinders utilize the *independence principle*. This principle assumes that the flow can be separated in a longitudinal and a transverse part, and that these can be analyzed separately. This is sometimes denoted the *cross flow principle* but here the latter term will be reserved for the special case when the transverse flow is considered pure 2-D, with no variation in the longitudinal direction.

The force and motion in the bi-normal direction, corresponding to an y axis into the plane in figure 2.1, are assumed identical to the normal direction in most of the following discussion.

2.1.1 Slender Body theory for flexible cylinder

The slender body theory is described in detail in Lighthill (1960) and Newman (1977). It is based on potential flow, thus viscous effects are neglected and strictly speaking only valid for the part of the body where there is no flow separation. By assuming small and slowly varying displacement the problem can be divided in a longitudinal and a lateral flow problem, an application of the independence principle. Due to the small angle θ the local coordinate system of F_n and F_t is assumed to coincide with the global system (x, y, z).

No tangential force component is predicted by the theory, but the normal force per unit length is given by:

$$\begin{aligned} F_n &= -\left(\frac{\partial}{\partial t} + U\frac{\partial}{\partial x}\right)(v\ a) \\ &= -a\left(\frac{\partial}{\partial t} + U\frac{\partial}{\partial x}\right)^2 z \\ &= -a\frac{\partial^2 z}{\partial t^2} - 2aU\frac{\partial z}{\partial x \partial t} - aU^2\frac{\partial^2 z}{\partial x^2} \end{aligned} \tag{2.1}$$

Here $v = \frac{\partial z}{\partial t} + U\frac{\partial z}{\partial x}$ is the relative velocity between the element and the fluid in the z direction. The added mass a is considered constant along the cylinder except at the ends. End effects are discussed by Paidoussis, Grinevich, Adamovic, and Semler (2002) and Dowling (1988) but will be neglected here.

When applied to slender, rigid bodies, the theory is applied to the forward part of the body, before any flow separation. For a flexible, oscillating cylinder there is no fixed separation points, and a correct application of the theory is therefore difficult. An extension of the theory to higher order accuracy is given by Lopes, Paidoussis, and Semler (2002).

2.1.2 General formulation of Viscous Forces

The viscous forces are highly dependent on semi-empirical formulas, particularly because the flow is usually turbulent in real cases. The formulations for force per unit length used here were suggested by Taylor (1952):

$$F_t = C_t\,\frac{1}{2}\rho V^2\ d \tag{2.2}$$

$$F_n = C_n\,\frac{1}{2}\rho V^2\ d \tag{2.3}$$

where ρ is the density of water and d is the diameter of the cylinder, and V is again the relative velocity between body and fluid. Note that V is not decomposed in normal and tangential directions. The decomposition is included in the coefficients which are functions of flow parameters like angle of attack, Reynolds number and in some cases the amplitude of motion. Expressions for these coefficients are the main goal of the experimental work in the following chapters, while some possible expressions are presented in the next sections.

2.2 Axi-symmetric boundary layer

For evaluation of the tangential force F_t it must be realized that the boundary layer on a cable is different from a flat plate. Equations for the axi-symmetric turbulent flow past a long cylinder are given by White (1972). His results for local skin friction and boundary layer thicknesses are given in figure 2.3. For streamers typical values are $R_a = \frac{Ua}{\nu} = 1\times10^5$, where $a = \frac{d}{2}$ is the radius of the streamer, and $R_x = \frac{Ux}{\nu} = 1\times10^8 - 1\times10^{10}$ (Heenan and Morrison 2002). From figure 2.3 a) expected values values of the local skin friction coefficient is $C_f \simeq 0.03$. Also, with tow speed $U = 2.5$ ms^{-1}, streamer diameter $d = 0.05$ m the boundary layer thickness is approximately $\delta = 0.2$ m, or five times the diameter of the cylinder.

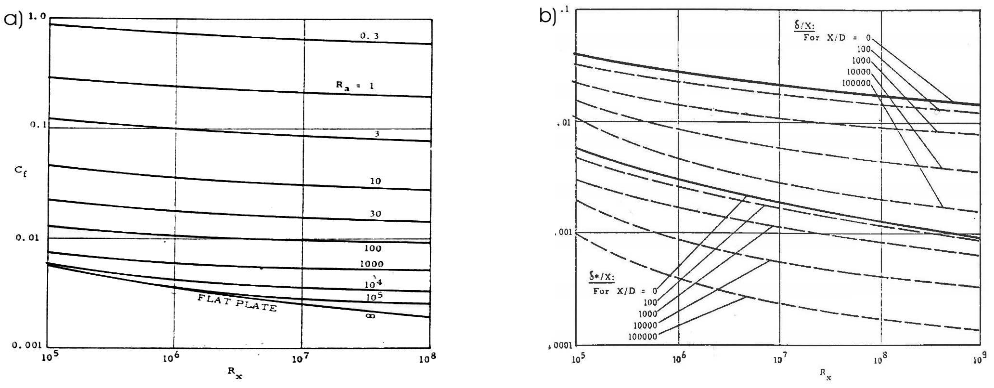

Figure 2.3: *Axi-symmetric boundary layer. a) Local skin friction coefficient. b) boundary layer (δ) and displacement ($\delta*$) thickness. From White (1972).*

White (1972) also gives an approximate formula for the averaged friction force coefficient on a cylinder of length L and radius a:

$$C_F = 0.0015 + \left(0.30 + 0.015\left(\frac{L}{a}\right)^{0.4}\right) Re_L^{-\frac{1}{3}} \tag{2.4}$$

valid for $1 \times 10^6 \leq Re_L \leq 1 \times 10^9$ and $\frac{L}{a} \leq 1 \times 10^6$. In this range, the formula is within 5% of the numerical result. Results are given in figure 2.4. By taking the derivative, a local friction coefficient may be found:

$$C_f(x) = 0.0015 + \left(0.20 + 0.016\left(\frac{x}{a}\right)^{0.4}\right) Re_x^{-\frac{1}{3}} \tag{2.5}$$

Here $x = 0$ is the upstream end of the cylinder.

For a streamer oscillating in the normal direction, the flow is of course not axi-symmetric. The case for small angle of attacks are discussed by Heenan and Morrison (2002) and references therein. The conclusion is that the friction force decreases on the upstream side and increases on the downstream side, but no quantitative results are given. Another effect mentioned by Heenan and Morrison (2002) is that the boundary layer is not continuous for the length of the streamer. When calculating the friction coefficient an effective length should be used. For a real streamer this length might not be more than 2-3 meters, giving effective length to diameter ratios of about 50.

The above formulas are valid for smooth cylinders, i.e, no effect of roughness is considered. For a flat plate the highest admissible roughness for this assumption to hold is:

$$k_{adm} \leq 100\frac{\nu}{U} \tag{2.6}$$

taken from Schlichting (1979). The admissible roughness then only depends on the dynamic viscosity ν of the fluid and the velocity outside the boundary layer U. The limit is valid for turbulent boundary layers and is slightly conservative for a flat plate. It should be safe to use it also for the axi symmetric layer since it depends on the thickness of the viscous sublayer which if anything is larger for the axi symmetric case than for the flat plate (White 1972).

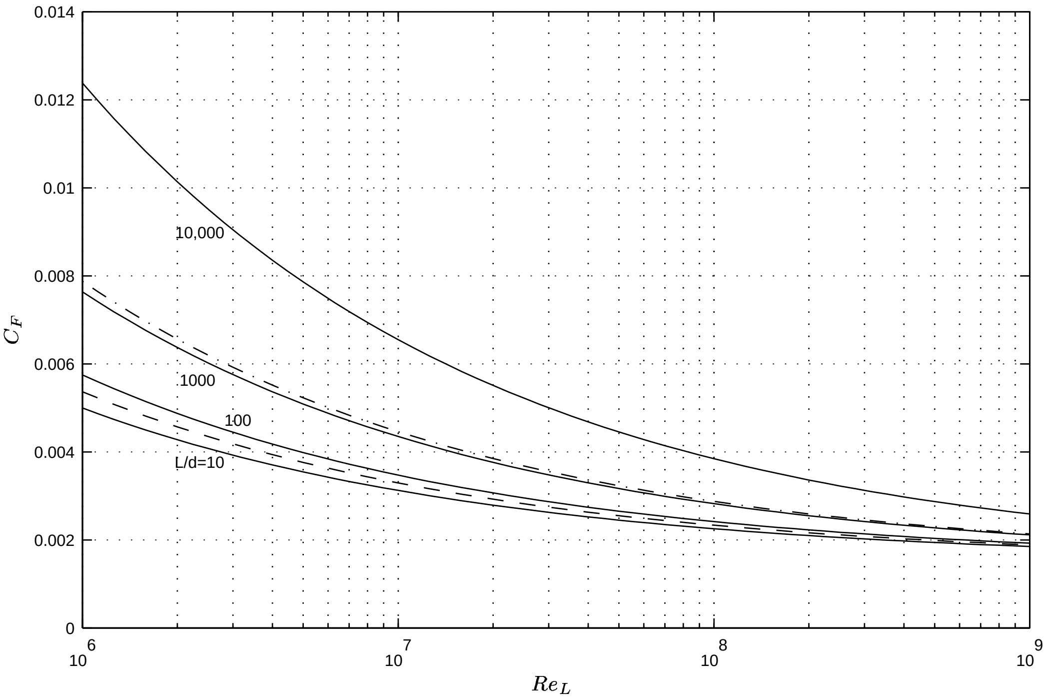

Figure 2.4: *Averaged skin friction coefficient C_F for various length to diameter ratios. Special values:* $--\ \frac{L}{d} = 40$*, the rigid cylinder experiment;* $-\cdot-\ \frac{L}{d} = 1200$*, the flexible cylinder experiment.*

2.3 Rigid cylinder at constant angle of attack

It seems that very few studies are available on the normal force of flexible cylinders at low angle of attack, particularly if separation is present. On the other hand, the related problem of forces on rigid cylinders of finite length are studied in much more detail, usually in connection with airplane fuselages and missiles. Figure 2.5 is taken from Zilliac, Degani, and Tobak (1991) and defines three leeward side flow regimes of a pointed infinitely long rigid cylinder. Three angle of attack regimes are defined: For low angles ($\alpha < 30°$) the flow is steady and symmetric relative to the angle of attack plane. In an intermediate range ($30° < \alpha < 50°$) the flow field is essentially composed of regime 3 in figure 2.5, steady and asymmetric tip vortices. For higher angles this becomes unstable, until for $\alpha > 65°$ the regimes 2 and 3 is located on the forward part of the body and regime 1 over the aft part. These limits were based on experiments with a relatively short body ($L/d = 16$) and it is expected that for longer bodies regime 1 will be more pronounced also for lower angles.

2.3.1 Cross flow principle

The regime 1 in figure 2.5 is the part where the cross flow principle is valid. The normal force coefficient is then written

$$C_n = C_d \sin^2(\alpha) \tag{2.7}$$

where C_d is the sectional drag coefficient of a circular cylinder in cross flow.

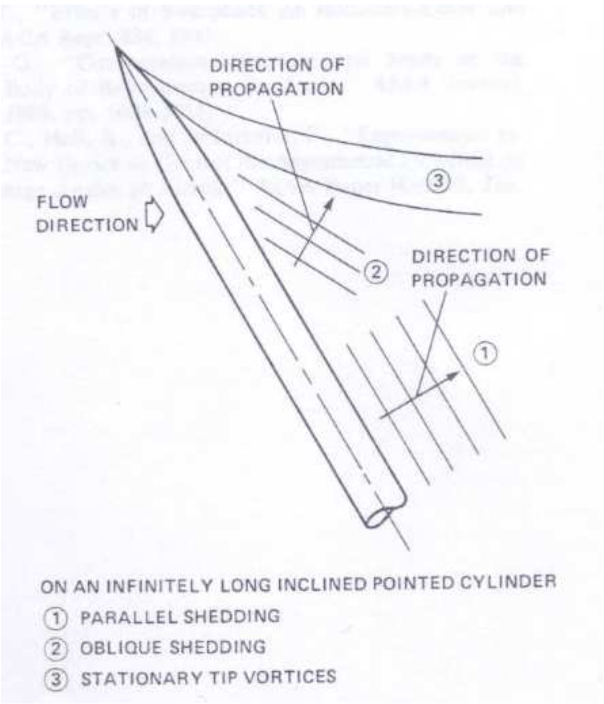

Figure 2.5: *Schematic of leeward-side flow regimes on a pointed cylinder. From Zilliac, Degani and Tobak (1991).*

A justification for this principle is given by Marshall (2003):. The Navier-Stokes equations for the longitudinal (x) and transverse directions (y and z) are, neglecting gravity:

$$\frac{\partial u}{\partial t} + u\frac{\partial u}{\partial x} + v\frac{\partial u}{\partial y} + w\frac{\partial u}{\partial z} = -\frac{1}{\rho}\frac{\partial p}{\partial x} + \nu\left(\frac{\partial^2 u}{\partial x^2} + \frac{\partial^2 u}{\partial y^2} + \frac{\partial^2 u}{\partial z^2}\right) \tag{2.8}$$

$$\frac{\partial v}{\partial t} + u\frac{\partial v}{\partial x} + v\frac{\partial v}{\partial y} + w\frac{\partial v}{\partial z} = -\frac{1}{\rho}\frac{\partial p}{\partial y} + \nu\left(\frac{\partial^2 v}{\partial x^2} + \frac{\partial^2 v}{\partial y^2} + \frac{\partial^2 v}{\partial z^2}\right) \tag{2.9}$$

$$\frac{\partial w}{\partial t} + u\frac{\partial w}{\partial x} + v\frac{\partial w}{\partial y} + w\frac{\partial w}{\partial z} = -\frac{1}{\rho}\frac{\partial p}{\partial z} + \nu\left(\frac{\partial^2 w}{\partial x^2} + \frac{\partial^2 w}{\partial y^2} + \frac{\partial^2 w}{\partial z^2}\right) \tag{2.10}$$

The local velocities in x, y and z directions are denoted u,v and w respectively, p is the pressure and ν the kinematic viscosity. The component of the free stream velocity are denoted U for the longitudinal direction and W for the normal direction, where the free stream is assumed to be in the $x - z$ plane. The variables can be non-dimensionalized by:

$$x^* = \frac{x}{L},\ y^* = \frac{y}{d},\ z^* = \frac{z}{d},\ u^* = \frac{u}{U},\ v^* = \frac{v}{W},\ w^* = \frac{w}{W},\ t^* = \frac{tW}{d},\ p^* = \frac{p}{\rho W^2} \tag{2.11}$$

Inserting in equations (2.8) - (2.10) and dropping the asterisks on the dimensionless variables:

$$\frac{\partial u}{\partial t}+\frac{\epsilon}{\alpha^*}u\frac{\partial u}{\partial x}+v\frac{\partial u}{\partial y}+w\frac{\partial u}{\partial z} = -\epsilon\alpha^*\frac{\partial p}{\partial x}+\frac{1}{Re_{2d}}\left(\epsilon^2\frac{\partial^2 u}{\partial x^2}+\frac{\partial^2 u}{\partial y^2}+\frac{\partial^2 u}{\partial z^2}\right) \tag{2.12}$$

$$\frac{\partial v}{\partial t}+\frac{\epsilon}{\alpha^*}u\frac{\partial v}{\partial x}+v\frac{\partial v}{\partial y}+w\frac{\partial v}{\partial z} = -\frac{\partial p}{\partial z}+\frac{1}{Re_{2d}}\left(\epsilon^2\frac{\partial^2 v}{\partial x^2}+\frac{\partial^2 v}{\partial y^2}+\frac{\partial^2 v}{\partial z^2}\right) \tag{2.13}$$

$$\frac{\partial w}{\partial t}+\frac{\epsilon}{\alpha^*}u\frac{\partial w}{\partial x}+v\frac{\partial w}{\partial y}+w\frac{\partial w}{\partial z} = -\frac{\partial p}{\partial z}+\frac{1}{Re_{2d}}\left(\epsilon^2\frac{\partial^2 w}{\partial x^2}+\frac{\partial^2 w}{\partial y^2}+\frac{\partial^2 w}{\partial z^2}\right) \tag{2.14}$$

The non-dimensional parameters are the diameter to length ratio $\epsilon = d/L$, inflow velocity ratio $\alpha^* = W/U = \tan(\alpha)$ and the Cross flow Reynolds number $Re_{2d} = \frac{Wd}{\nu}$. The same substitution in the continuity equation gives

$$\frac{\epsilon}{\alpha^*}\frac{\partial u}{\partial x}+\frac{\partial u}{\partial y}+\frac{\partial v}{\partial z} \tag{2.15}$$

By inspection of equations (2.12) - (2.15) it can be concluded that the terms including derivatives with respect to x can be neglected if:

1. $\epsilon \ll 1$
2. $\epsilon \ll \alpha$

The first requirement is the definition of slender bodies and should be fulfilled. The second requirement on the other hand will not be fulfilled as the angle of attack goes to zero. As an example, for angle of attack $\alpha = 10°$ the requirement cannot be said to be fulfilled for $x < 60 \times d$ where $\frac{\epsilon}{\alpha} > 0.1$.

The Reynolds number in equations (2.12) - (2.14) follows from the choice of non-dimensional variables in equation (2.11) and is based on the cross flow velocity. The question is if this is correct when choosing the drag coefficient if there also is a high longitudinal flow component present. For the 2-D case of a cylinder in cross flow the drag coefficient is very much dependent on the Reynolds number, see e.g Faltinsen (1990) where four regimes are defined for a smooth cylinder: Sub-critical ($Re_{2d} < 2 \times 10^5$), critical ($2 \times 10^5 < Re_{2d} < 5 \times 10^5$), supercritical ($5 \times 10^5 < Re_{2d} < 3 \times 10^6$) and trans-critical ($Re_{2d} > 3 \times 10^6$). Here the limiting Reynolds numbers are significantly reduced by roughness. The drag coefficient typical drops from $C_d = 1.2$ in the sub-critical regime to $C_d \simeq 0.4-0.6$ in the critical regime before increasing again to $C_d \simeq 0.8$ for trans-critical flow. Since this change is explained by transition from laminar to turbulent boundary layer upstream of the separation point, the boundary layer due to longitudinal flow should be of importance. If the boundary layer on the cylinder is turbulent due to longitudinal flow, the trans-critical value of $C_d = 0.8$ should probably be used even in cases where Re_{2d} is in the sub-critical regime.

2.3.2 The 2D+t principle

In 2D+t theory the three-dimensional steady flow is mapped to a two-dimensional flow with time dependence. This can be applied for the low angle of attack regime, where a vortex pair is formed close to the nose and develops downstream, in a steady pattern. This is illustrated in figure 2.6 and is referred to as the NACA vortex model (Sarpkaya 1966). Now consider a plane fixed with respect to the fluid and perpendicular to the axis of the body. As the body pierces this plane its trace moves laterally in the plane with velocity $U_n = U\sin(\alpha)$. This is illustrated in figure 2.6 where the plane is located at a distance x from the nose of the body. The flow in the plane is then assumed 2-D but time dependent, where the x component of the flow with respect to the body is mapped to a time $t = \frac{x-x_0}{U}$ in the transverse plane. x_0 is the distance from the nose to the location of initial separation. The time is non-dimensionalized by:

$$s = \frac{2Ut}{d} = 2\frac{x}{d}\frac{U_n}{U} = 2\frac{x}{d}\sin(\alpha) \tag{2.16}$$

From Schlichting (1979) the minimum time from separation start is $s = 0.351$, for the 2-D case and laminar flow. Both Jorgensen and Perkins (1958) and Bryson (1959) assumes that separation starts approximately at the transition from the nose cone to the cylinder part of the body, as observed in experiments (Jorgensen and Perkins 1958). For hemispherical noses the change in pressure gradient at the junction triggers two so-called *horn vortices* (Traub and Rediniotis 2003), an effect that may have similarities for the pointed nose. The problem of an 'expanding' cylinder in the 2-D analogy is neglected and the flow is assumed similar to the flow of an impulsively started cylinder in pure cross flow. As in the cross flow principle, the effect of a boundary layer due to the longitudinal flow is neglected.

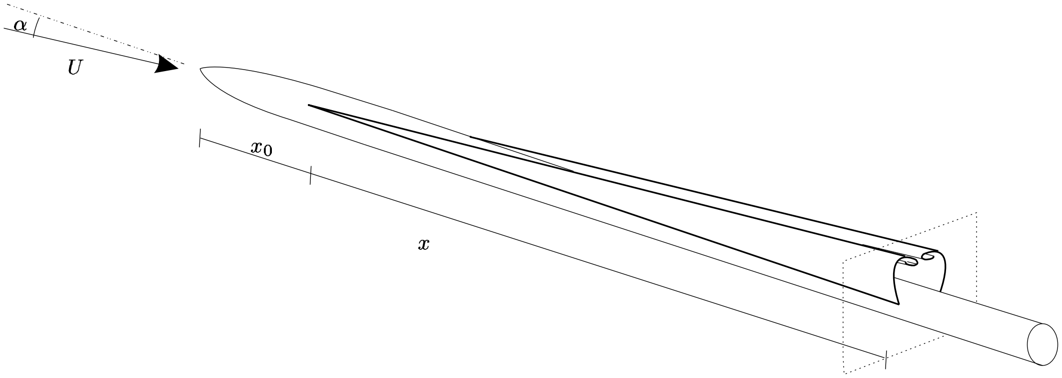

Figure 2.6: *Symmetric vortex separation on a slender body at low angles of attack.*

Calculated and measured force histories of an impulsively started cylinder are shown in figure 2.7. The numerical results are from high resolution vortex method (Koumoutsakos and Leonard 1995). They are characterized by a singularity at $s = 0$, a minimum value at $s \simeq 1$ and a maximum at $s \simeq 4$. The high Reynolds number case has minimum and maximum at the same non-dimensional times, but the range of values are larger and oscillations more pronounced. Experimental values in figure 2.7 are taken from Sarpkaya and Isaacson (1981). The rise and maximum of this curve seems to lag compare to the numerical result. This might be a result of experimental procedure, since some time of acceleration always will be present in an experiment. Note that the curves in figure 2.7 are the results of digitizing the printed curves in the references, so some error compared to the actual data is possible.

The experimental results in curve *c)* in figure 2.7 is plotted as a function of position and angle off attack in figure 2.8. The normal force at a given angle is given by integration of the

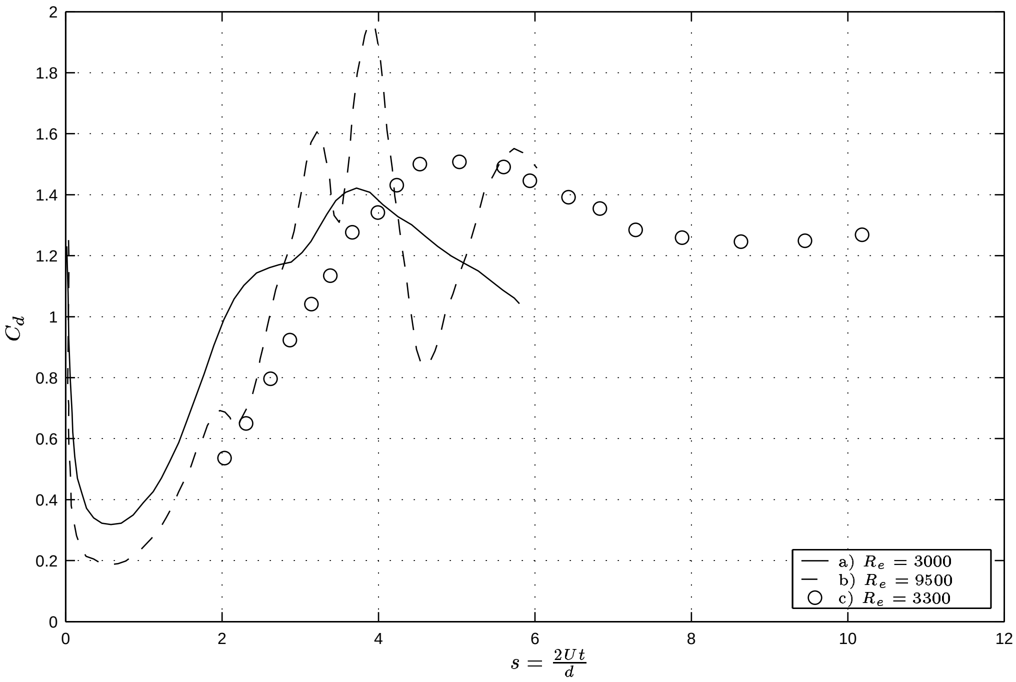

Figure 2.7: *Drag coefficient for impulsively started cylinder: a) and b) are numeric results (Koumouttsakos and Leonard, 1995) while c) is experimental results (Sarpkaya and Isaacson, 1981).*

curve formed by the surface in figure 2.8 and a plane normal to the α axis. By inspection, it is obvious that the effect is highest at low angles of attack, $\alpha \leq 5°$, both with respect to normal force and even more pronounced trough a moment on the cylinder. As should be expected the result from 2D+t method approaches the cross flow principle when angle of attack and length to diameter ratio increases. This is indicated by the level area of the surface in the upper right part in figure 2.8.

The total force on the cylinder is

$$F_n = \int_{x_0}^{L} C_d(x,\alpha)\mathrm{d}x \; \frac{1}{2}\rho U_n^2 d \; = \int_{s_0}^{s_L} C_d(s)\mathrm{d}s \; \frac{1}{4}\rho U_n U d^2 \tag{2.17}$$

Where the limits s_0 and s_L corresponds to x_0 and L respectively. With $x_0 = 0$ the ratio of force from cross flow principle (F_n^{CF}) and equation (2.17) is

$$\frac{F_n}{F_n^{CF}} = \frac{\int_0^{s_L} C_d(s)\mathrm{d}s}{C_d^{CF}\, s_L} \tag{2.18}$$

Where superscript CF denotes cross flow principle. Results are given in figure 2.9 a) where it is clear that the 2D+t principle gives less normal force than the cross flow principle.

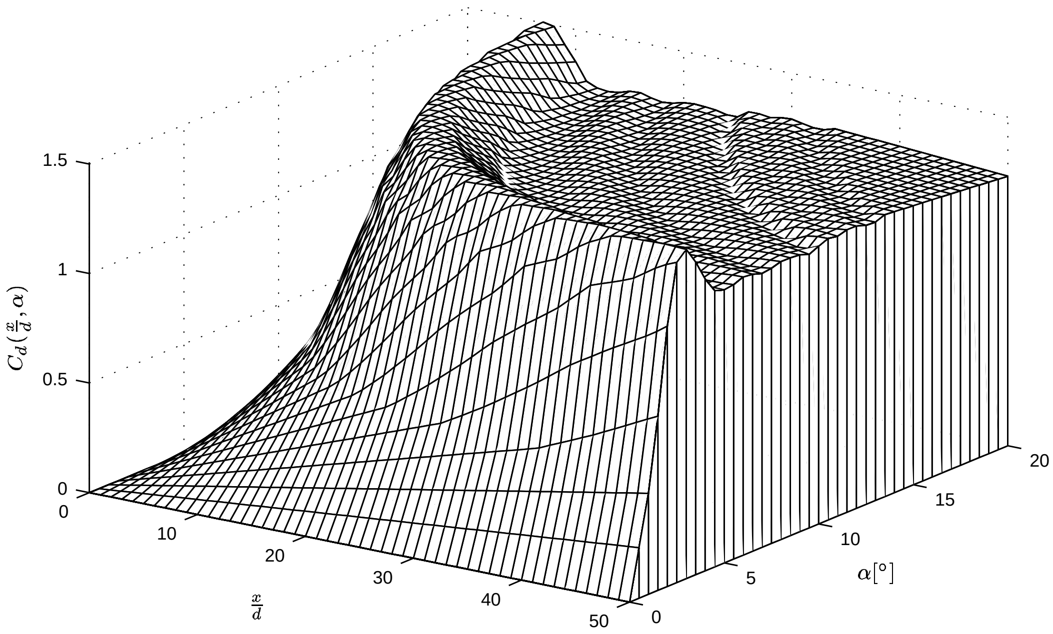

Figure 2.8: *Coefficients in 2D+t theory as function of position and angle of attack. The results are based on curve c) in figure 2.7, assuming $C_d(s) = 0$ for $s = 0$.*

The moment about $x = \frac{L}{2}$ is for 2D+t principle:

$$\begin{aligned} M_z &= \int_0^L C_d(x,\alpha)x\mathrm{d}x \; \frac{1}{2}\rho U_n^2 d - \frac{L}{2}F_n \\ &= \int_0^{s_L} C_d(s)s\mathrm{d}s \; \frac{1}{4}\rho U^2 d^3 - \frac{L}{2}F_n \end{aligned} \tag{2.19}$$

The ratio of this and $F_n^{CF}L$ is given in figure 2.9 *b*). The moment is positive for nose up. Then the negative values means that the moment from 2D+t tends to stabilize the cylinder.

The symmetric flow pattern in figure 2.6 will at some point break down and the alternating vortex shedding known from a cylinder in cross flow will appear. According to Sarpkaya and Isaacson (1981) this process start when the drag coefficient is at its maximum for the impulsively started cylinder. For the slender body, Jorgensen and Perkins (1958) comments that it seems that the symmetric pattern is more stable than expected from the analogy to 2D flow, so it is possible that the pattern is sustained for higher angles than indicated by impulsive start analogy. As referred to in the beginning of this section, for a body with $L/d = 16$ the symmetric flow pattern is observed for angle of attacks up to 30° (Zilliac, Degani, and Tobak 1991).

2.3.3 Intermediate regimes

The cross flow and 2D+t principle is applicable for high and low angles of attack respectively, corresponding to regimes 3 and 1 (with symmetric vortices) in figure 2.5. An approximate

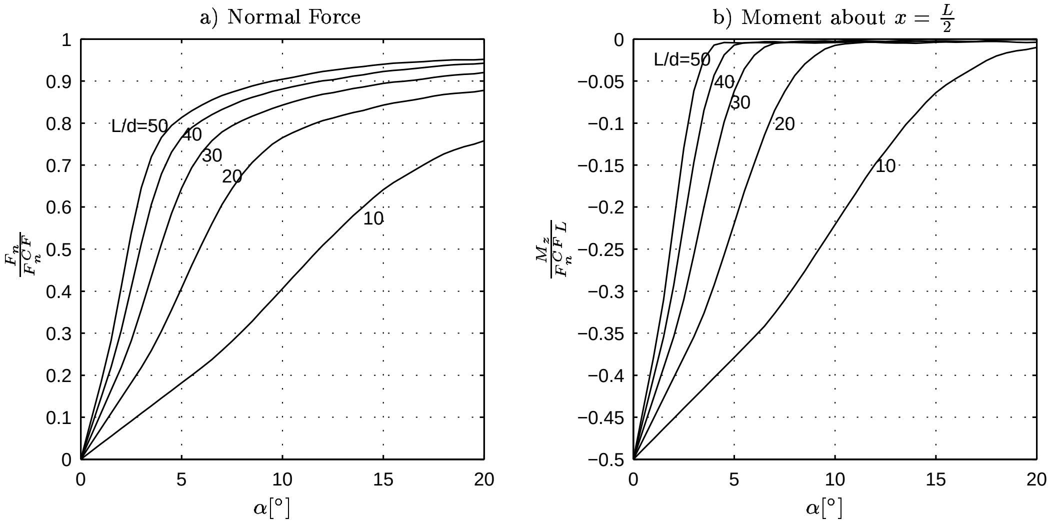

Figure 2.9: *Normal Force and Moment for 2D+t compared to cross flow principle*

theoretical description of the flow regimes between these does not seem to exist. Zilliac, Degani, and Tobak (1991) present measurements for the intermediate angles where the tip vortices are still steady, but becomes asymmetric. The direction of the asymmetry is unstable and depends on details of the nose and incoming flow. This region is characterized by high side, or bi-normal, forces on the body. Unfortunately Zilliac, Degani, and Tobak (1991), or later references on the same topic, does not discuss the lift, or normal force, for this region. The regime 2 in figure 2.5 is described by Ramberg (1983) and is characterized by a the fact that the vortices are not parallel to the cylinder. This also results in the shedding frequency being lower than expected from the cross flow principle. Again, no data is given for the forces on the cylinder for this flow regime.

2.4 Oscillating rigid cylinder

Due to waves, control devices mounted on the streamer or motion of the tow vessel a streamer towed in the ocean is more likely than not exposed to oscillating flow. The slender body theory above already allows for this, but the effect of viscosity are different in the oscillating case than in the steady case discussed above and may depend on the amplitude and frequency of the oscillation.

2.4.1 Separated flow

For cases where separation of flow takes place i.e the amplitude of motion is at least in the same order as the cylinder diameter, the only available theory seems to be based on the cross flow principle. Then the normal force is given by Morison's equation:

$$F_n = \rho\pi\frac{d^2}{4}\;\dot{w}_f - C_a\;\rho\pi\frac{d^2}{4}\;\dot{V}_n - C_d\;\frac{1}{2}\rho\;d\;V_n\,|V_n| \qquad (2.20)$$

Here a dot denotes time derivative, w_f is the velocity of the surrounding fluid, C_a is the added mass coefficient, C_d is a cross flow drag coefficient and $V_n = \dot{z} - w_f$ is the normal component of the relative velocity between cylinder and fluid. The first term is the Froude-Kriloff force. For a cylinder oscillating in fluid at rest, this term is zero, while for a cylinder at rest in oscillating fluid, the two inertia terms can be combined using the mass coefficient $C_m = 1 + C_a$. Compared to the expression above, the Morison's equation includes the first term in equation (2.1) and the viscous force from equation (2.3) with coefficients taken from the cross flow principle in equation (2.7).

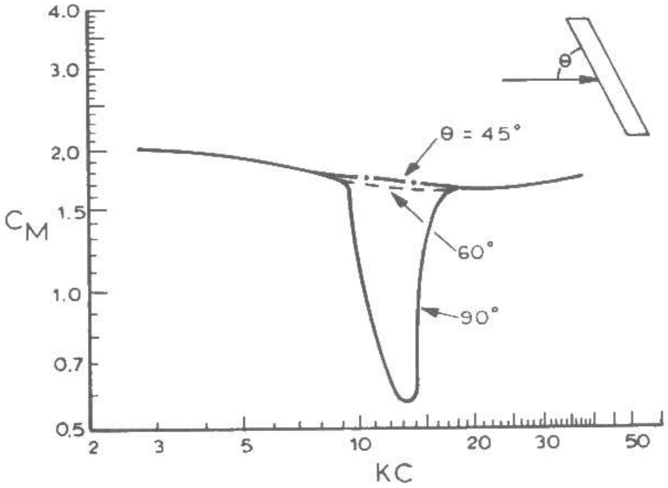

Figure 2.10: *Mass coefficient* $C_m = 1 + C_a$ *versus Keulegan-Carpenter number* $K = KC = \frac{U_{n0}T}{d}$ *for inclined cylinder in oscillating flow. From Chakrabarti(1987).*

For the 2D case of a cylinder fixed in a harmonically oscillating flow, it is well known that the coefficients C_a and C_d is not functions of the Reynolds number only, but also the history of the motion itself (Sarpkaya and Isaacson 1981; Faltinsen 1990) . This dependence is expressed through the *Keulegan-Carpenter number*:

$$KC = \frac{U_{n0}T}{d} = 2\pi\frac{A_0}{d} \tag{2.21}$$

Here U_{n0} and A_0 is the velocity and displacement amplitudes of the harmonic motion, T the period of the oscillation and d still the cylinder diameter. The variation of the coefficients for various inclinations of the cylinder are shown in figure 2.10 and figure 2.11. The figures are taken from Chakrabarti (1987), based on experimental data from Sarpkaya, Raines, and Trytten (1982). The measurements were performed in an U-tube where the cylinder is at rest in an oscillating water column. These data are not directly applicable to a towed streamer, since there is no constant flow in the axial directions and the angle of attack is high in the U-tube experiments. But the important result from these figures is that the large reduction in C_m and increase in C_d seen for a cylinder in normal flow ($\theta = 90°$ in figures 2.10 - 2.11) does not occur for the inclined cases, so this may be a very specialized phenomena that will not occur in the

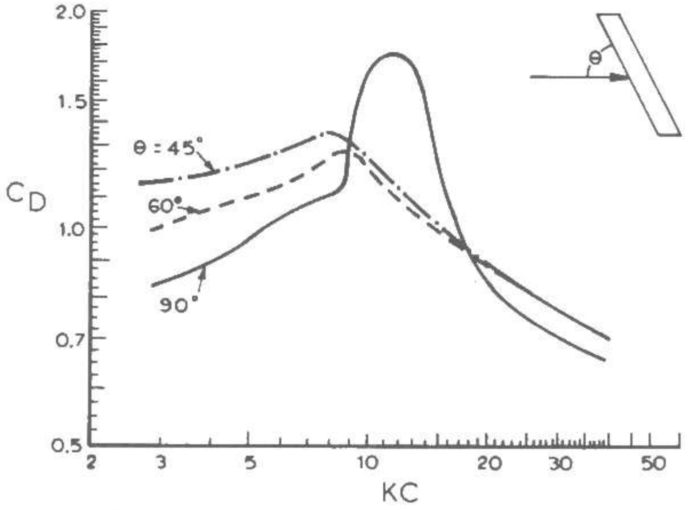

Figure 2.11: *Drag Coefficient C_d versus Keulegan-Carpenter number $K = KC = \frac{U_{n0}T}{d}$. for inclined cylinder in oscillating flow. From Chakrabarti(1987).*

current case either. This may explain the limited success in Ersdal and Faltinsen (2002), where a 2D+t approach was used to modify the KC number in order to use the data for a cylinder at $\theta = 90°$.

2.4.2 Attached flow

For small amplitudes or very low velocities, the flow may not separate from the cylinder, and the drag term from equation (2.20) becomes invalid. In this case the skin friction becomes just as important as pressure forces (Faltinsen 1990). The skin friction is discussed by Taylor (1952). For a stationary cylinder the absolute value of the normal force is

$$F_n = \left(C_d^p + C_d^f\right)\,\frac{1}{2}\rho V_n^2\ d \tag{2.22}$$

where V_n is the fluid velocity normal to the cylinder. The drag coefficient is split in two, where C_d^n is due to normal stresses and C_d^f is due to shear stress and given by

$$C_d^f = 4Re_n^{-\frac{1}{2}} \tag{2.23}$$

The cross flow Reynolds number is $Re_n = \frac{dV_n}{\nu}$ In the case of attached flow, the part due to normal force will be taken as equal to the shear part (Faltinsen 1990, p. 237). Inserting this and that the normal component of velocity is $V_n = U\sin(\alpha)$ the force is

$$F_n = 8Re_d^{-\frac{1}{2}}\sin^{\frac{3}{2}}(\alpha)\frac{1}{2}\rho U^2\ d \tag{2.24}$$

where $R_{ed} = \frac{Ud}{\nu}$ is Reynolds number based on cylinder diameter. This has the form of equation (2.3) with:

$$C_n = 8Re_d^{-\frac{1}{2}}\sin^{\frac{3}{2}}(\alpha) \tag{2.25}$$

For harmonically oscillating flow Faltinsen (1990) gives an expression for the shear part:

$$C_d^f = 2\pi \left(\frac{\pi}{Re_n \; KC} \right)^{\frac{1}{2}} \tag{2.26}$$

The cross flow Reynolds number is here based on the amplitude of the oscillating flow. In the form of equation (2.3) this becomes, again with a normal stress effect of equal amplitude:

$$C_n = 4\pi \left(\frac{\pi}{Re_d \; KC} \right)^{\frac{1}{2}} \sin^{\frac{3}{2}}(\alpha_0) \tag{2.27}$$

where α_0 is the amplitude of the angle of attack.

These expressions both utilizes the independence principle. An alternative is to assume that the friction force on the cylinder is parallel with the incoming flow, so that

$$C_n = \pi C_F \sin(\alpha) \tag{2.28}$$

The normal force coefficient C_n is based on the diameter of the cylinder, while the skin friction coefficient is normally based on the vetted surface $S = \pi d L$, hence the factor π in equation (2.28).This form is used by Paidoussis (1966) and Dowling (1988).

2.4.3 Bi-normal Force

A consequence of asymmetric vortex shedding is that a bi-normal force will be created on the cylinder. If the cross flow principle is applied, this force will be oscillatory even for steady inflow. For a flexible cylinder the result is a out of plane, or bi-normal, response. For an oscillating flow the bi-normal force is expected to be quite irregular (Chakrabarti 1987). One possibility is to express the force as a Fourier series with frequencies equal to and multiples of the forcing frequency. Analysis based on experimental data in a U-tube indicates that the coefficients and their relative importance is very sensitive to the KC-number, at least for the 2-D case (Faltinsen 2000). For large KC-numbers a quasi-steady model was developed by Bearman, Graham, and Obasaju (1984), revising a model by Verly (1982). This model assumes constant Strouhal number ($S_t = \frac{U}{f_v \; d}$, where f_v is the frequency of the oscillating force) and is based on instantaneous flow velocity (. See also Chakrabarti (1987, p 196) or Faltinsen (1990, pp 248-249). In this work the study of the bi-normal force is limited to discussions of asymmetric vortex shedding.

2.5 Error analysis: Basic statistics

The aim of an error analysis is to give a quantitative measure of how reliable a measured or calculated value is. Normally this is presented as a confidence interval, e.g 95%. This means that the probability that the true value is within the given interval is 0.95. In the following the word error will be used to describe the distance between a measured or calculated value and the true, but unknown, value. The word uncertainty may be used for the statistical estimate of the same thing.

Even if a careful and throughout error analysis is performed, parts of the analysis is open to discussion, and there is always the possibility that some major error source is overlooked.

On the other hand, to draw conclusions based on experimental results without at least trying to quantify the error level seems at best optimistic. An error analysis also includes a study of the sensitivity of the final results to input parameters, which ideally should be an important consideration when designing or refining the experiment.

All analysis here refers to so-called time-wise experiments, i.e. the measured quantity is measured at a single location at different times. The alternative in which the quantity varies in space but not in time are called sample-to-sample experiments. For marine applications this applies to thermodynamic properties of water and material properties of a material. For the towing tank experiments considered here such variations are not considered.

2.5.1 Bias, precision and total error

Two types of errors are considered in the analysis: *bias* and *precision* errors. The difference is illustrated in figure 2.12 taken from Coleman and Steele (1989). The figure also illustrates the *total* error as the sum of bias and precision errors. A main assumption in this analysis is that if an infinite number of measurements were taken the precision error would follow a Gaussian distribution. The bias error would then be the difference between the mean of this distribution and the true value. The trouble with these definitions is of course that the true value is unknown, so in practice an alternative definition is needed.

To do this the concept of replication levels are introduced. When repeating an experiment the replication level describes what exactly is repeated, here in three levels. At the zeroth order replication the measured quantity is assumed absolutely constant in time, so that only variations inherent in the measurement system contributes to the error. For example, calibration of load cells before mounting it in the experimental setup should give zeroth order replication. In this case the true value is known, so bias and precision can be estimated in the normal sense. At first-order replication level the instrumentation and setup is fixed, but the time is running. This corresponds to repeating the experiment keeping the instrumentation constant. Typically this corresponds to a time series of a measured variable. N'th level replication includes all other possible changes when repeating the experiment, from doing a second run at a later time to performing a similar experiment in another laboratory.

A more practical distinction between precision and bias error then is as follows. The precision error is given by the variation of the data at a given replication level, while the bias error are constant for the same level. The precision error can be estimated to a reasonable degree by repeating the experiment, but this is not the case for the bias error without increasing the replication level. In practice, particularly in a large and expensive laboratory like a towing tank, there will be a practical limit on this replication level. Estimates of the bias error must therefore be based on experience and more or less educated guesses. The resulting error level will always be uncertain and open to discussion, particularly if the bias errors are large.

2.5.2 Sample population and confidence interval

If the measurement is repeated an infinite number of times, the main assumption here is that the measured value will be normal, or Gaussian, distributed around a mean. This *parent distribution*

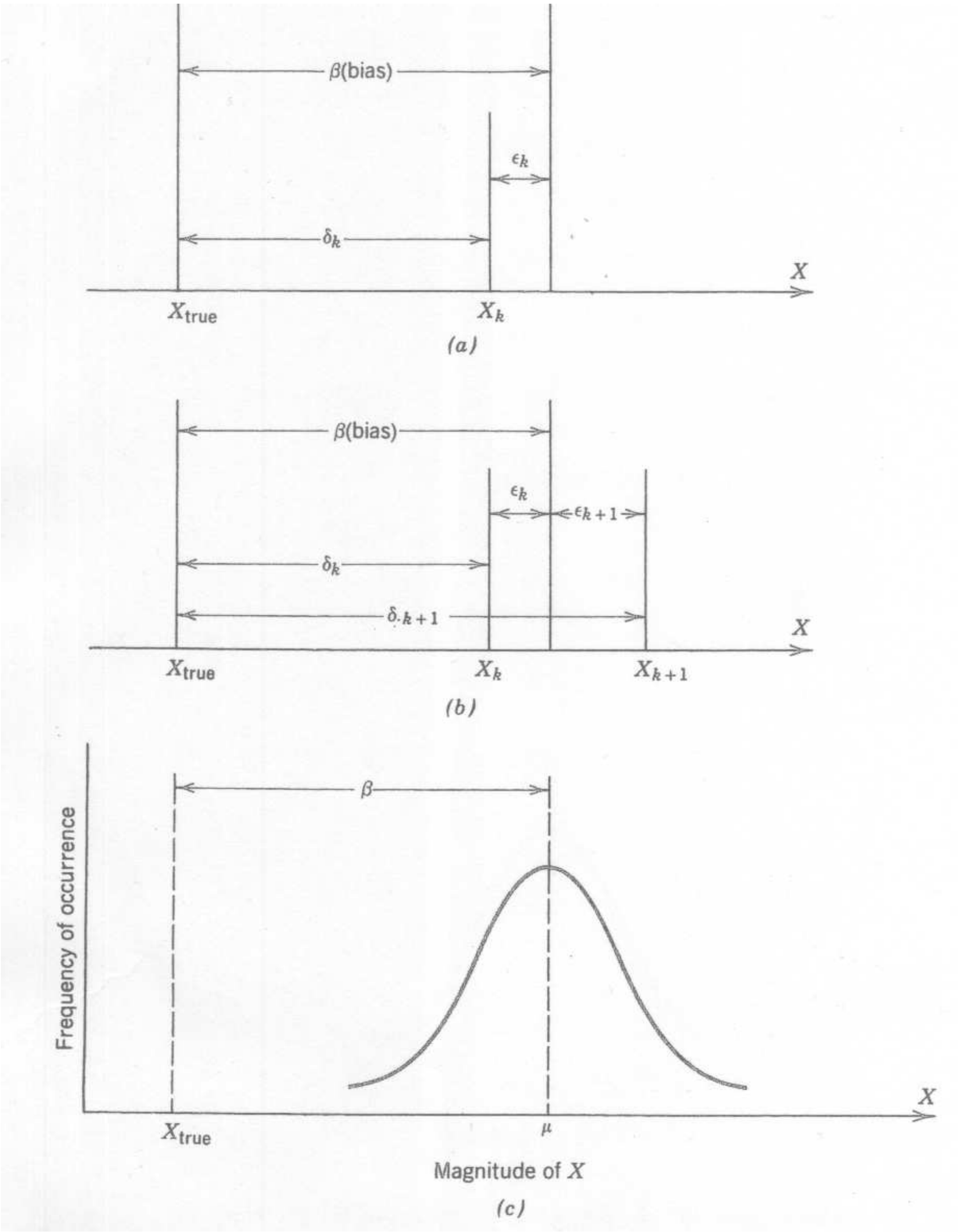

Figure 2.12: *Errors in the measurements of a variable X: a) single reading, b) two readings, c) infinite number of readings. From Coleman and Steele (1989).*

is characterized by the mean μ and the standard deviation σ, and expressed by

$$f(X) = \frac{1}{\sigma\sqrt{2\pi}} \mathrm{e}^{-\frac{(X-\mu)^2}{2\sigma^2}} \tag{2.29}$$

here $f(X)\mathrm{d}x$ is the probability that a single measurement X will lie between X and $X+\mathrm{d}X$. The measurement is of course never repeated an infinite number of times. The statistical properties of interest is therefore based on a *sample population* that consist of a finite number of samples drawn from the parent distribution. For the sample population the mean is given by

$$\overline{X} = \frac{1}{N}\sum_{j=1}^{N} X_j \tag{2.30}$$

where N is number of samples (measurements) X_j. The precision index, or standard deviation, of the sample population is estimated by

$$S_x = \sqrt{\frac{1}{N-1}\sum_{j=1}^{N}(X_j - \overline{X})^2} \tag{2.31}$$

Working with a sample population, the mean in equation (2.30) will depend on the set of samples taken from the parent population. Thus the mean itself is normally distributed with mean μ (mean of the parent distribution) and standard deviation (Kreyszig 1988)

$$S_{\overline{x}} = \frac{S_x}{\sqrt{N}} \tag{2.32}$$

For the parent distribution the confidence interval of a sample is given by

$$Prob(X_j - t\sigma \leq \mu \leq X_j + t\sigma) = \gamma \tag{2.33}$$

where $t \simeq 1.96$ for a normal distribution and confidence level $\gamma = 0.95$, i.e the 95% confidence interval. For the sample population, the standard deviation is only estimated thus the value of t is not given. This is especially true if the number of samples are low. Equation (2.33) can be rewritten

$$Prob\left(t \leq \frac{X_j - \mu}{S_x} \leq t\right) = \gamma \tag{2.34}$$

where the variable $\frac{X_j-\mu}{S_x}$ is random and follows a Student's t distribution, with $N-1$ degrees of freedom. The value of t may be found from (Kreyszig 1988)

$$t = F^{-1}\left(\frac{1}{2}(1+\gamma)\right) \tag{2.35}$$

where $F^{-1}(\cdot)$ is the inverse of the cumulative density function for the t-distribution, again with $N-1$ degrees of freedom. Figure 2.13 gives values of t for 95% and 99% confidence intervals. For $N > 30$ the value $t = 2$ is acceptable (International Towing Tank Conference 1990). The precision limit for a sample is then

$$P_x = tS_x \tag{2.36}$$

and for the mean of N repetitions

$$P_{\overline{x}} = t\frac{S_x}{\sqrt{N}} \tag{2.37}$$

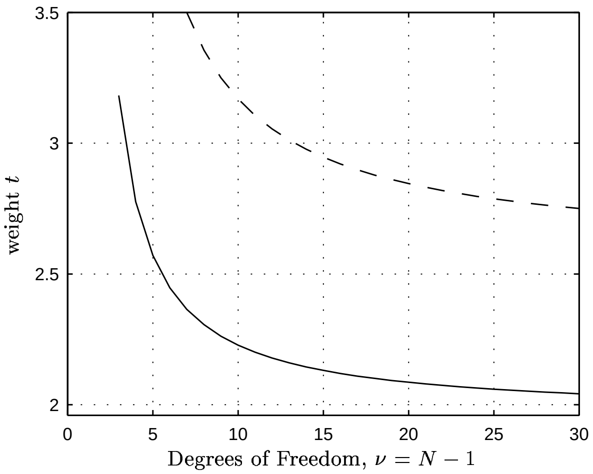

Figure 2.13: *The weight t for estimating confidence intervals: — 95% confidence; -- 99% confidence. Ordinate axis corresponds to 95% confidence for a normal distribution: t=1.96.*

2.5.3 Chauvenet's criterion for rejecting outliers

Data samples that appear significantly out of line with the majority of samples are called *wild* points, or *outliers*. If the reason for such discrepancy is obvious and verifiable, such points can be disregarded. In cases where the reason is harder to explain, an acceptable criterion for rejection of a sample is the Chauvenet's criterion. This states that samples within a band around the mean with probability of exceedance less than $1 - \frac{1}{2N}$ should be retained. This limit can be expressed as a weight on the standard deviation:

$$t_{chauvenet} = F^{-1}\left(\frac{1}{2}(1+p)\right) \tag{2.38}$$

where $p = 1 - \frac{1}{2N}$ is the limit probability based on N samples. Note that in this case $F(\cdot)$ is the cumulative density function of the normal distribution, also for small values of N. Values of $t_{chauvenet}$ are plotted in figure 2.14.

Samples with higher deviation from the mean than:

$$\left|X_j - \overline{X}\right| > t_{chauvenet}\; S_x \tag{2.39}$$

may then be disregarded, and a new mean and standard deviation can be found based on the remaining data. The procedure can only be performed once.

2.5.4 Bias error estimation

The precision limits in equation (2.36) and equation (2.37) is only valid for the precision part of the error, while the bias cannot be treated this way. This follows from definition, the bias error does not change when the measurement is repeated. Note that the higher the replication level of repeated measurements, the fewer unknown bias errors there are in the results. This means

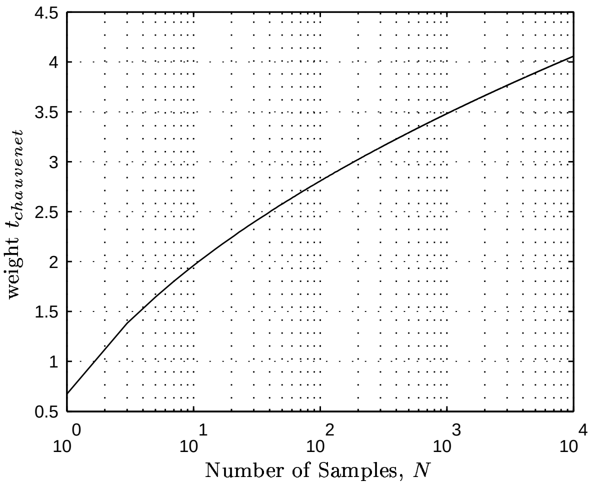

Figure 2.14: *The weight $t_{chauvenet}$ in Chauvenet's criterion for rejection of outliers.*

that errors that must be estimated if the experiment is performed only once, might be included in a statistical analysis if the experiment is repeated.

Known and well defined bias errors, like constant terms in a calibration model, are usually corrected for and not included in the error analysis. The rest, for example the uncertainty of the constant term in the calibration model, must be estimated in some way. The approach is to establish a bias error limit B that with a given confidence represents the unknown bias. In order to establish this limit simplified estimates, experience or more or less educated guesses must be applied.

2.6 General Uncertainty Analysis

The parameter actually measured is seldom the final result of the test. For example, when measuring force with a strain gauges the parameter actually measured is an electrical resistance. Based on the change in resistance, a force is calculated, and then usually non dimensionalized. The final result is therefore a function of several parameters, both inherit in the measurement method and in the preferred way to present the result.

2.6.1 Reduction equation

The functional relationship is called the *reduction equation* and is expressed:

$$X = f_r(Y_1, Y_2, ..., Y_N) \tag{2.40}$$

where X is the measurement (sample) and the reduction equation f_r is a function of N parameters $Y_1 \dots Y_N$. Examples for the experiments in later chapters of such parameters are calibration factors, tow speed and model dimensions but also less obvious factors like temperature and thermodynamic properties of water. The first step of the error analysis is to establish a list of parameters that must be considered. In the following these parameters are denoted *elemental error sources*.

Assuming that a small change in a parameter Y_i results in a small change in the measured value, Taylor expansion gives:

$$\begin{aligned} X &= \hat{X} + \frac{\partial \hat{X}}{\partial Y_i}\Delta Y_i + \frac{1}{2}\frac{\partial^2 \hat{X}}{\partial Y_i^2}\Delta Y_i^2 + \mathcal{O}\left(\Delta Y_i^3\right) && (2.41)\\ &\simeq \hat{X} + \frac{\partial \hat{X}}{\partial Y_i}\Delta Y_i && (2.42) \end{aligned}$$

From this, the *influence coefficient* is defined as

$$\kappa_i = \frac{\partial \hat{X}}{\partial Y_i} \tag{2.43}$$

and the elemental error is:

$$e_i = \frac{\partial \hat{X}}{\partial Y_i}\Delta Y_i = \kappa_i \Delta Y_i \tag{2.44}$$

In most cases the absolute value of ΔY_i is not known. Rather it is given as a precision limit based on a confidence interval as described in the previous section. The recommended practice is the 95% confidence interval, where the probability of the actual ΔY_i being less or equal to the estimated value is 95%:

$$\Delta Y_i = P_{Y_i} = P_i \tag{2.45}$$

or for bias error

$$\Delta Y_i = B_{Y_i} = B_i \tag{2.46}$$

Where P_i and B_i are the precision and bias limit of parameter Y_i respectively.

2.6.2 Error propagation

If all elemental error sources are independent, the combined effect on the measured value (error propagation) is:

$$e = \sqrt{\sum_{i=1}^{N}\left(\kappa_i\ \Delta Y_i\right)^2} \tag{2.47}$$

The precision and bias errors are calculated separately:

$$\begin{aligned} e_P &= \sqrt{\sum_{i=1}^{N}\left(\kappa_i\ P_i\right)^2} && (2.48)\\ e_B &= \sqrt{\sum_{i=1}^{N}\left(\kappa_i\ B_i\right)^2} && (2.49) \end{aligned}$$

where subscript P is denotes precision and B denotes bias error.

The total error may be found by

$$e = \sqrt{e_S^2 + e_B^2} \tag{2.50}$$

According to Coleman and Steele (1989) this gives approximately a 95% coverage of the true value. The alternative is to sum the errors

$$e = e_S + e_B \tag{2.51}$$

This gives 99% coverage if the bias and precision errors are of the same order and 95% coverage if one is negligible compared to the other. International Towing Tank Conference (1990) recommends both to be reported, but only the former will be discussed in later chapters.

If $\hat{X}$ is the erroneous measurement and e is the total error from equation (2.50), the true value X is found in the interval

$$X = \hat{X} \pm e \tag{2.52}$$

with a probability of 95%. This of course requires that the 95% confidence interval is used throughout the analysis. It is also assumed that the bias error is symmetric, which is not always the case. If not, a high and low limit must be established from equation (2.50).

Here the error has the same unit as the measured value itself. An alternative is to define a *relative error*:

$$e_r = \frac{e}{\hat{X}} \tag{2.53}$$

so that

$$X = \hat{X} \ \ (1 \pm e_r) \tag{2.54}$$

The relative error can be calculated by using a *relative influence coefficient*:

$$\kappa_{ri} = \frac{1}{\hat{X}} \frac{\partial \hat{X}}{\partial Y_i} \tag{2.55}$$

in equations (2.48) - (2.49) .

2.7 Measurement Errors

The following steps are listed in International Towing Tank Conference (1990) in order to create an uncertainty interval for a measurement:

1. identify all error sources
2. determine the individual precision and bias errors for each error source
3. determine the sensitivity of the end result to error sources
4. create the total precision interval
5. create the total bias uncertainty

6. combine total bias and precision either by addition or *root sum square* method (equation (2.50)
7. declare results from 4)-6) separately.

The first two steps are the tough ones. A possible approach is to start with the reduction equation and then consider its parameters and what might influence them. Then the replication level must be considered in order to distinguish between precision and bias errors. The question is typically if the experiment is repeated, and which uncertainties are covered by repetition.

The influence coefficients is found by partial derivation of the reduction equation, either analytically if possible or numerically by changing input parameters to a numerical procedure.

The ITTC report use a slightly different way to calculate the precision error than the one outlined above. Rather than establishing a precision limit P for each parameter Y, a total precision limit is calculated

$$S_{result} = \sqrt{\sum_{i=1}^{N} (\kappa_i S_i)^2} \tag{2.56}$$

The precision error is then given by

$$e_P = t_{95} \frac{S_{result}}{\sqrt{M}} \tag{2.57}$$

where t_{95} is the weight based on a 95% confidence interval and M is the number of times the test is repeated. To find t_{95} from a student's t distribution an average degree of freedom is required, weighted by the magnitude and degree of freedoms of the individual precision indexes S_i. This is done by the Welch-Satterthwaite approximation:

$$\nu_{result} = \frac{(\sum S_i^2)^2}{\sum \frac{S_i^4}{\nu_i}} \tag{2.58}$$

This do not seem to give a simplification compared to calculating a precision limit for each elemental error source, so this method is not applied here.

2.8 Modeling errors

The word model is used in at least three different contexts in this thesis. First there is the physical models used in the experiments, i.e the hardware actually put in the water in order to measure force or response. Next there is the mathematical model used to describe some physics, possibly on several levels. Thus the hydrodynamic force model is a mathematical model used in the simulation of the motion of a cable, a higher level mathematical model. Finally there is a numerical model, here used to describe the implementation of a mathematical model, thus including the numerical methods and other approximations made to actually solve the equations given by the mathematical models. Hopefully it will be clear from the context what is actually meant in each case.

The flow diagram in figure 2.15 is adapted from International Towing Tank Conference (1990) and describes the modeling and validation process. Note the distinction between verification and validation, the former being the process of checking that the implemented code actually gives a true representation of the mathematical model(s), while the latter is to verify that the numerical model is an adequate representation of the physical reality. Roughly speaking the verification will in the following be done by comparison to analytical results for special test cases, while validity of the numerical model is based on comparison to experiments.

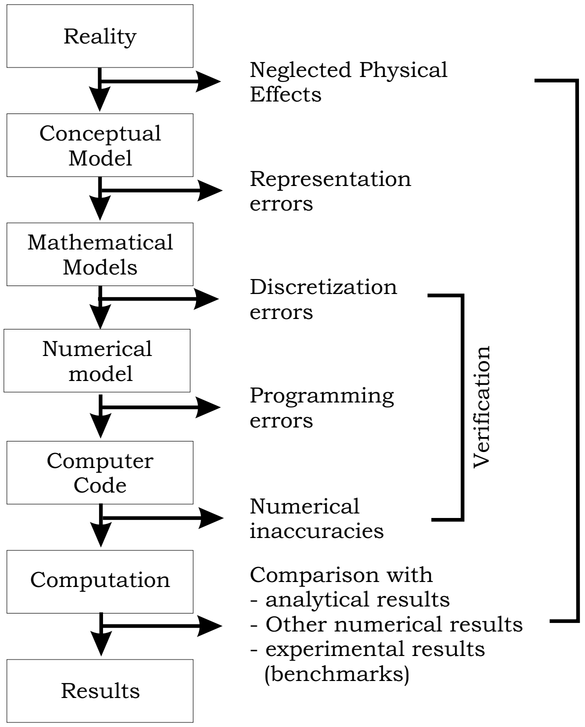

Figure 2.15: *Modeling and validation process. From recommendations in International Towing Tank Conference (1990).*

A confidence interval of the numerical model is established in the same way as for the experimental results, considering the numerical model a reduction equation and estimating limits for each parameter. Error sources to be considered are indicated in figure 2.15.

2.8.1 Comparing model and experiment

In comparing measured and calculated results the distinction between measurement errors and modeling errors are not always obvious. This is the case for parameters not explicitly stated in the reduction equation, so that a numerical model is necessary to estimate sensitivity. An example of this is found in chapter 5 for the transverse response of a cable. Here parameters like aft tension, length, and tow speed are not included in the reduction equation, although these parameters certainly effects the resulting response. In the following parameters of this type will be treated as modeling errors while the term measurement errors will be reserved for uncertainties in the actual measurement.

When comparing experiment to a mathematical model there are then at least three quantities to consider. The first of these is the difference between the calculated and measured results:

$$e_{diff} = X^{mod} - X^{exp} \tag{2.59}$$

where X^{mod} is the result from the mathematical model and X^{exp} is the result from the measurement. To measure the performance of the model for a range of parameters a precision index can be formed as before:

$$e_{diff} = t\sqrt{\frac{1}{N-1}\sum_{j=1}^{N}\left(X_j^{mod} - X_j^{exp}\right)^2} \tag{2.60}$$

where t is the weight corresponding to a given confidence interval as discussed above and N is the number of samples.

By including the errors inherent in the numerical analysis and from uncertainty in input parameters (e_{num}), a total modeling error can be defined:

$$e_{mod} = \sqrt{e_{diff}^2 + e_{num}^2} \tag{2.61}$$

But this error only makes sense if compared to the measurement errors. If the model error is less or equal to the measurement error, that is

$$e_{mod} \leq e_{exp} \tag{2.62}$$

then the model is as good as the measurements, and further improvements makes no sense. In this case the validation is complete, and the numerical model is acceptable based on the available data. If a range of parameters are considered, some representative values must be used for e_{mod} and e_{exp}.

Chapter 3

Rigid cylinder at stationary angles

The rigid cylinder setup were ran in the the Marine Cybernetics Laboratory (MCLab) and in towing tanks I+III, see appendix A. The experiments in the towing tank was performed in September 2002 where the cylinder was rotated in yaw. The follow up experiment in the in MCLab were performed in December 2003, this time rotating the cylinder in pitch. The results were found to be quite different in the two cases, a fact that will be discussed toward the end of the chapter.

3.1 Experimental setup

Figure 3.1 and figure 3.2 show the model mounted in the MCLab.

The main components of the model were:

A The test section was made of a aluminum pipe 2 m long and 51 mm in diameter. The wall thickness was 2 mm and total mass was 1.877 kg (with end plugs). Using a roughness reference pad the roughness height of the spray painted surface was estimated to be less than 1.5μm.

B The force sensors were standard 2 DOF sensors from MARINTEK. The test section was simply supported at the ends to avoid cross talk from moment. The assembly of sensors and couplings were 130 mm long and covered by an aluminum pipe. The gap between this cover and the test section was 1 mm, assuring free movement of the test section. See figure 3.3.

C The end supports are a total of 270 mm long, where the forward 150 mm was approximately a parabola. The struts are 1 m long solid aluminum bars of elliptic cross section (30×10 mm).

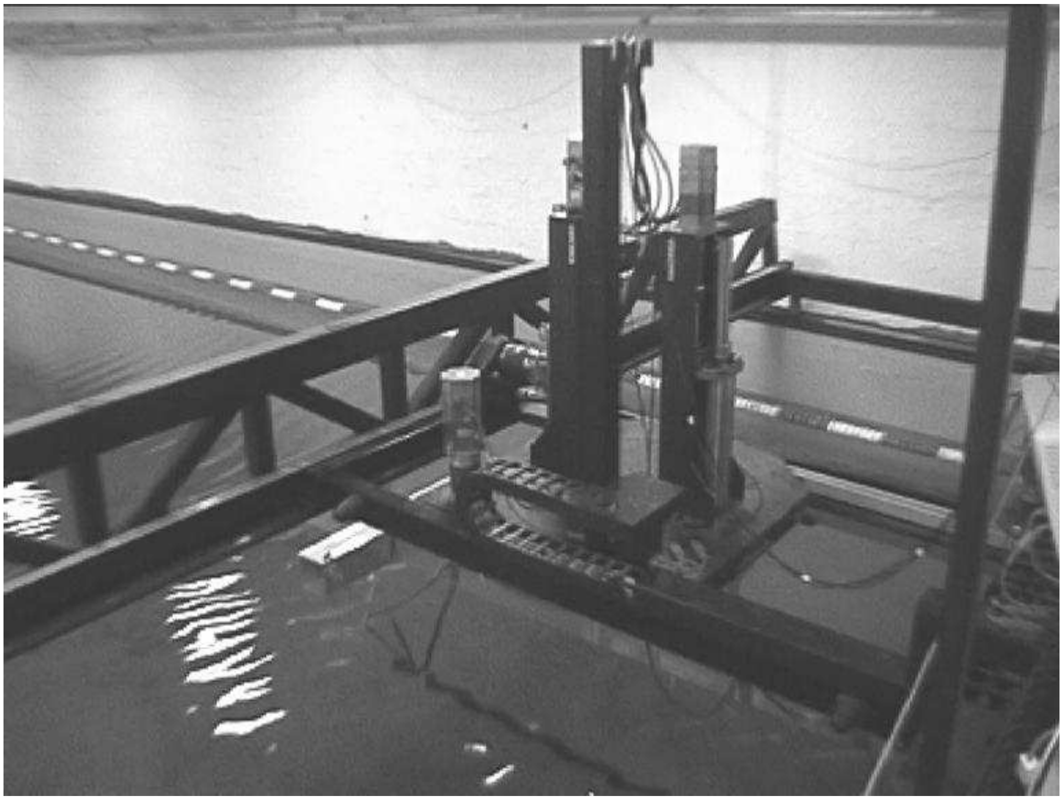

Figure 3.1: *Towing the rigid cylinder in MCLab. Tow speed is U=0.6 ms*$^{-1}$

Table 3.1: *Parameters of the test section*

Length	L	2.03 m
Diameter	d	0.051 m
Dry Weight	m	1.875 Kg
Water density	ρ	998.5 Kg/m^3
Dyn. viscosity	ν	1.05×10^{-6} m^2/s
Length to diameter ratio	$\frac{l}{d}$	39.2
Structural mass to Added mass ratio	$\frac{m_s}{\rho\pi\frac{d^2}{4}}$	0.46
Roughness	$\frac{k}{d}$	29.5×10^{-6}

D The yoke structure was made of aluminum RHS 200 × 200 beams. It was connected to the vertical actuators of the carriage by hinges. At the left connection in figure 3.2, rails and linear ball bearings are used between the hinge and the support beam in order to allow pitch motion of the model.

Important parameters are given in table 3.1.

The main idea of this design was that only forces on a constant cross section should be measured. Drag and lift forces from the end supports and struts should not have to be corrected

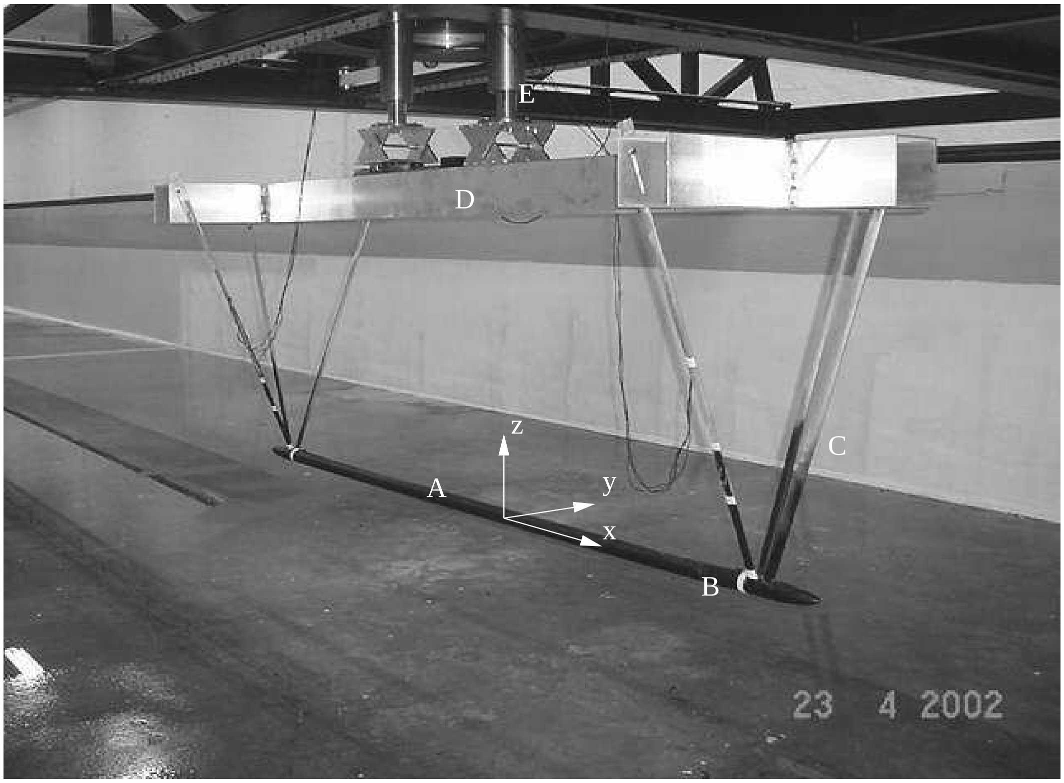

Figure 3.2: *The Model mounted under the carriage in MCLab: A -test section, B -Force sensor housing, C -end supports and struts, D -yoke*

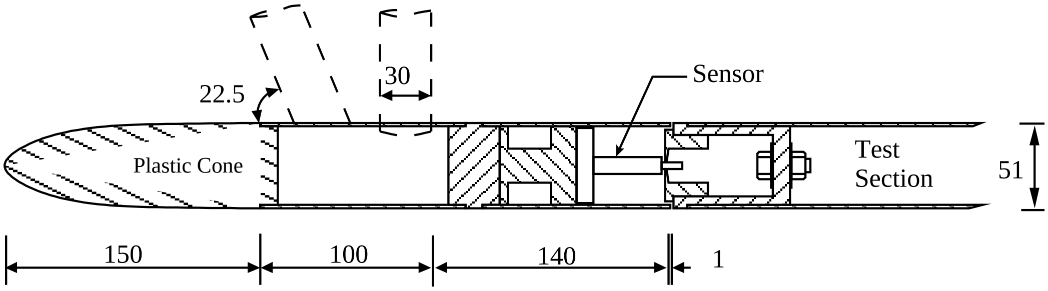

Figure 3.3: *Model detail: End support and sensor housing. Measurements in mm and deg.*

for. The length of the test section was a compromise between high Reynolds numbers (based on length) and the length of the basin. Typical towing length in MCLab was 25 m, or 12.5 times the length of the section. The diameter was selected mainly to ensure that the cylinder was truly rigid. For a load of 40 N/m the max displacement was less than 0.1% of the section length.

The sensor arrangements is shown in figure 3.3. A pin in a finely fitted hole was used to decouple moment from shear loads. This also eliminated axial loads induced by bending of the test section. Shim plates were used to limit the axial movement of the test section. This setup allowed the test cylinder to rotate around it's axis, but from observation during the experiment it seemed that the friction in the support was enough to prevent this. In the towing tank the model was mounted on a rig allowing manual setting of draft and yaw angle, while in the MCLab all settings were done by the control system of the carriage.

The force sensors are standard strain gauges based designs used extensively by MARINTEK, while all velocities are encoder outputs from the carriages. In both laboratories a Hottinger MGC+ were used for amplification, filtering and analog to digital conversion of all measurements. Although same make and model, two different units were used. In the towing tank a sample frequency of 200 Hz and a filter cutoff frequency of 60 Hz were used. For the followup experiments in the MCLab the sampling frequency was reduced to 120 Hz, filtering at 40 Hz. In both cases the cutoff frequency was set to well below the Nyquist frequency to avoid aliasing of the signal. All force signals were recorded in volts, while calibration and all data analysis were performed on a PC using MATLAB®.

3.2 Error analysis

In this section the methodology described in the last part of chapter 2 is used to establish a 95% confidence inteval for the measurement results

In the towing tank, each run were performed in both directions for each combination of velocity and angle. The experiment were first performed 13'th September 2002, and repeated the 25'th, and again the 27'th September 2002. Each result is then an average of six runs. The exception is the angles above 12° which were only ran the last day, thus only two repetitions exist for these angles. In MCLab all experiments were repeated three times and for selected angles six times. Here all runs are in the same direction.

It is then possible to use the variation in the result directly to estimate a confidence interval, but to better understand the nature of the errors, a detailed analysis of the elemental errors was performed. This must in any case be done for the bias errors.

3.2.1 Reduction Equations

In conformation with later chapters the angle of attack is denoted by the symbol α. The force normal to the cylinder axis, but in the plane formed by the incoming velocity and this axis, is denoted the normal force. The bi-normal force is then the force normal to this plane. In the MCLab the model was rotated about the y-axis in figure 3.2 for most of the runs, so that the z axis is the normal direction while the y axis is the bi-normal direction. This is denoted rotation in pitch in the following. In the towing tank and the remaining runs in the MCLab the model were rotated about the z axis, in which case y axis becomes the normal and z axes the bi-normal directions, respectively. This is then denoted yaw rotation.

The presented results of the experiments are force and moment coefficients. Denoting the measured forces from the two force sensors with superscripts f and a for forward and aft sensor respectively, the reduction equations described in chapter 2 are

$$C_{n2}(\alpha) = \frac{F_y^a + F_y^f}{\frac{1}{2}\rho U^2 \; dL} \tag{3.1}$$

$$C_{n3}(\alpha) = \frac{F_z^a + F_z^f}{\frac{1}{2}\rho U^2 \; dL} \tag{3.2}$$

$$C_{n5}(\alpha) = \frac{\left(-F_z^a + F_z^f\right) l}{\frac{1}{2}\rho U^2 \; dL^2} \tag{3.3}$$

$$= \frac{-F_z^a + F_z^f}{\frac{1}{2}\rho U^2 \; dL} \tag{3.4}$$

$$C_{n6}(\alpha) = \frac{\left(-F_y^a + F_y^f\right) L}{\frac{1}{2}\rho U^2 \; dL^2} \tag{3.5}$$

$$= \frac{-F_y^a + F_y^f}{\frac{1}{2}\rho U^2 \; dL} \tag{3.6}$$

The subscripts 2 and 3 denotes forces in the y and z directions, while 5 and 6 indicates moment about the same axes.

To generalize, the reduction equations contain measured forces, a dynamic pressure $q = \frac{1}{2}\rho U^2$ and representative dimensions. The error sources are grouped according to this.

3.2.2 Precision and bias limits for force measurements

For the force measurements, there are three replications levels available:

- The sensors were calibrated after assembly. By rotating the sensor and the spacer it was mounted on, known weights of 10-500 grams were applied in directions 0,90,120,180,240, and 270 degrees with respect to the positive n axis. This gave more than 120 points on which to build a 2-D calibration model incorporating cross-talk and alignment errors:

  $$F_n = k_1 V_1 + k_2 V_2 \tag{3.7}$$

  Here F_n is the known force in direction n, V_{1-2} are the measured voltages in the two directions of the sensor and k_1 and k_2 are coefficients found by the least square fit method. The result is 4 sets of coefficients. This is the zeroth replication level.

- The measurements are recorded in in time series with steady state conditions for at least 15 seconds. The forces used in the analysis is the mean these time series and represents a 1'st replication level.

- At least some of the time series were repeated six times, representing a second order replication level with 3 degrees of freedom. Here variations in alignment and velocity are included in the data set, so the precision level should be higher for this case.

Precision limits are given in table 3.2. For zeroth order replication the value is the 95% confidence interval of the calibration model. The 1'st order level uses the forward runs on the

Table 3.2: *Precision and bias limit ranges and medians (in N) on force measurements. All velocities and angles included. (na -not applicable).*

Replication Level	Samples N	Weight t	y-direction min	y-direction max	y-direction median	z-direction min	z-direction max	z-direction median
0'th	120	2	0.015			0.028		
1'st	4000	2	0.021	0.616	0.048	0.029	0.248	0.066
2'nd	6	2.57	0	3.615	0.096	0.04	9.35	0.35
Bias errors								
	Vibration	B_{01}	0.0	0.15	0.0025	1.5×10^{-6}	0.008	0.0015
	Cylinder End	B_{02}	0	0.0022	4.4×10^{-5}	*na*		
	Strut Wake	B_{03}	*na*			0.0015		
Measured Force		$\lvert F_n\rvert$	0	37.387	0.615	4.00×10^{-4}	1.991	0.368

third day, while the 2'nd order includes all measured data. Six data points are assumed for all angles in this case. For the higher order levels the precision is given by (see chapter 2):

$$P_{\bar{x}} = t\frac{S_x}{\sqrt{N}} \tag{3.8}$$

In table 3.2 the median is given rather than the mean. The median is the value for which the probability of exceedance is 50%. In other words, half the calculated precision limits are lower than this value, and half the precision limits are higher. Since relatively few cases (mostly $\alpha > 20°$) gave quite high precision limits compared to the majority of the runs, the median is more representative than the mean. From inspection of the raw data it was found that for 1'st order replication the value does not vary with angle of attack, thus the variation in results are mainly due to variation in velocity.

For $\alpha > 20°$ the model was observed to oscillate and the standard deviation of the time series increases by a factor five or more. This is reflected in the max value of the precision level. For second order replication the z direction results are much higher than expected, particularly since these value should be less sensitive to small variations in angle of attack than the y-direction. This may imply unsteady flow pattern for the high angles.

The highest limits were found for the highest measured values, so the relative error is more constant than the precision levels indicates. Typically, the precision limit is about 5% of the measured values, at least in the y-direction.

The 2'nd order level is here included for comparison only. Since there was a small difference in speed in forward and back wards runs, the resulting precision limits is too high. When estimating the final error from repeated runs, the coefficients are calculated for all data series, then the mean and the precision level is established.

Identified sources of bias errors in the force measurements are

Roughness The surface roughness of the cylinder influence the magnitude of the skin friction on the cylinder. More importantly, increased roughness decreases the Reynolds number where the flow in the boundary layer changes from laminar to turbulent. The effect of roughness for a cylinder in steady cross flow is given in Faltinsen (1990, p. 177). The roughness from table 3.1 is an order of magnitude lower than the lowest values presented here. A flat plate can be assumed smooth for $k/x = k/d$ for local Reynolds numbers less than about 5×10^6 (Blevins 1992), which is the upper limit for the Reynolds number based on cylinder length in the experiments. It will from this be assumed that the cylinder is smooth, an any effect of roughness is neglected.

Vibrations (B_{01}) Since the total force on cylinder was measured, all inertia forces due to vibration induced by the carriage and its drive system were included in the measurements. But these are assumed to have zero mean, so they only effects effect the precision errors in table 3.2. The effect of vibration on the averaged hydrodynamic damping forces depends on the work done by the cylinder on the fluid, which again depends on the actual motion of the cylinder. From decay tests of the model mounted on the carriage the lowest eigenfrequency was found to be 9 Hz. The highest shedding frequency was found for 2.5 ms^{-1} tow speed and 30 degrees yaw angle. The estimated value is $f_v = 4.9 - 6.86$ Hz where the low value corresponds to subcritical flow (Strouhal number $S_t = 0.2$) and the high limit corresponds to transcritical flow, $S_t = 0.28$ (Faltinsen 1990). Since the in line oscillating force has twice the frequency of the vortex shedding, there is a possibility of matching load and eigenfrequency for the extreme cases. Oscillation of the model was observed, both visually and in the force measurements, for velocities above 1.5 ms^{-1} and angles above 20 degrees. For the remaining tests no oscillation of the model was observed and the motion of the cylinder is assumed limited to the clearance of the pin of the sensor to the fitting in the test cylinder, see figure 3.3. The clearance is 0.1 mm. For the case of VIV, Faltinsen (1990) give a simple relation between drag coefficient and amplitude of oscillation:

$$\frac{C_d}{C_{d0}} = 1 + 2\left(\frac{A}{d}\right)_{max} \tag{3.9}$$

Here C_{d0} is the drag coefficient without vibration, A is the amplitude and d is the cylinder diameter. Although the current case is not VIV, this represent an upper limit. The bias due to vibration can then be expressed

$$B_{01} = 2\left(\frac{A}{d}\right)_{max} F_0 = 0.004F_0 \tag{3.10}$$

Here F_0 is the measured force.

Cylinder end effects (B_{02}) To ensure that all forces actually went trough the force sensor a gap between the test cylinder and the support was necessary. This gap is shown in figure 3.4 and was about 1 mm. The boundary layer and displacement thickness at the forward gap can be found from figure 2.3. The displacement thickness is found to $\delta^* \simeq 1.2$ mm, about the same as the gap opening. It is then assumed that the tangential flow velocity at the gap is small and that potential forces from sudden change in diameter can be neglected. The analysis is then limited to include frictional forces due to low speed flow between the outer plate of the support and the protrusion at the cylinder end. This is assumed similar to a 2D channel flow, see right part of figure 3.4. The height of the channel was $h = 1$ mm, the breath $b = 4$ mm (the length of the protrusion on the cylinder end), and the length $l = \frac{1}{2}\pi\frac{d}{2}$, i.e half the circumference of the cylinder. From Blevins (1992, Table 13-4) the shear force on the walls are:

$$\tau = \frac{h}{2l}(p_1 - p_2) \tag{3.11}$$

Here $(p_1 - p_2)$ is the pressure drop through the channel. The pressure difference on the upstream and leeward side of the cylinder can be estimated by the dynamic pressure of the cross flow so that $(p_1 - p_2) \simeq \frac{1}{2}\rho\,(U\sin(\alpha))^2$. With equal flow on both side of the protrusion, the total force on the cylinder end is

$$B_{02} = \tau 2bl \ = hb\frac{1}{2}\rho\,(U\sin(\alpha))^2 \tag{3.12}$$

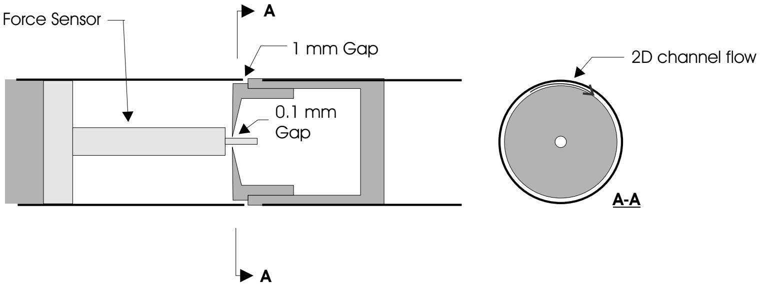

Figure 3.4: *Model detail: Test section end*

Analysis Errors The use of a well documented and tested tool like MATLAB® should reduce the number of bugs in the computer analysis scripts, an error source that is impossible to quantify. Another question is which part of the measured time series to use in analysis. All recordings were started before the actual run, so that all transient effects are present in the time series. The part of the time series used in averaging are identified based on the tow velocity, with a time delay from constant velocity was achieved to assumed steady state forces of at least 5 seconds. From visual inspection of selected force traces no transients were observed beyond this time, but no further analysis were done.

Wake of the struts (B_{03}) In planning the experiments it was estimated that the pressure recovery in the wake of a single strut should be quick enough so that it did not create a force on the test section. From runs with zero angle it is seen that there is a small vertical force on the forward sensor. This is most likely due to the combined effect of all three struts. Since the effect of angle of attack is uncertain, it cannot simply be subtracted from the results, but is included as a bias uncertainty limit. It only influences force in the z-direction.

When rotating in yaw it was found that the presence of the struts had a major influence on the initial vortex formation on the cylinder nose. This effect is studied by comparing rotation in yaw to results from rotating in pitch in the discussion of the results, and are not included in the error analysis.

The range and median of the bias limits are given in table 3.2. For the most part, the bias error is an order of magnitude lower than the precision limits.

Table 3.3: *Precision and bias limit for (in ms^{-1}) on reference velocity. All velocities and angles included. (na -not applicable).*

Replication Level	Samples N	Weight t	Tow speed [ms^{-1}] 1.0	1.5	2.0	2.5
1'st	4000	2	8.28×10^{-5}	1.2×10^{-4}	1.52×10^{-4}	1.85×10^{-4}
Bias errors						
Residual flow		B_{04}	0.004			
Generated waves		B_{05}	6.8×10^{-4}	0.0027	0.011	0.024

3.2.3 Precision and bias limits for dynamic pressure

The dynamic pressure is given by

$$q = \frac{1}{2}\rho(U - u_f)^2 \tag{3.13}$$

Here U is the tow speed as usual, while u_f is the velocity of the surrounding fluid in the tow direction, and must be included due to possibility of residual flow and generated waves. Only the tow speed was measured, while u_f represents the largest uncertainty with respect to bias.

The tow speed was measured by a counter mounted on the carriage rails. The precision error is given by equation (3.8) and listed for 1'st order replication in table 3.3. The speed was slightly different on forward and backward runs due to the speed control on the carriage, so there is to few data points to include 2'nd order replication here.

Bias errors are:

Residual flow (B_{04}) When the cylinder is towed, part of the water in the tank is set in motion, both in the form of wake and generation of waves. It will take some time after the run before this motion dies out, in fact this is the part of the actual experiment that requires the longest time. The waiting time between runs was minimum 4 minutes in the towing tank and twice that in the MCLab, based on experience and visual observation of the waves in the tank. An estimate of the level of residual flow can based on far wake theory. The mean velocity deficit at the center of a plane (or 2D) wake is given by (Blevins 1992, p.267)

$$\frac{u_1}{U} = 1.2\left(\frac{x}{C_d\, D}\right)^{-\frac{1}{2}} \tag{3.14}$$

For an axi-symmetric body the relation is

$$\frac{u_1}{U} = 0.35\left(\frac{x}{(C_D\, A)^{\frac{1}{2}}}\right)^{-\frac{2}{3}} \tag{3.15}$$

Here u_1 is the maximum velocity in the wake A the characteristic area on which C_d is based, and U the free stream velocity. Equations 3.14 and 3.15 refers to a coordinate system fixed to the moving body. Switching now to a plane fixed with respect to the fluid and normal to the direction of motion, as in 2D+t theory, the diffusion of the wake becomes a function of time by the substitution $x = \frac{U}{t}$:

$$
\begin{aligned}
u_1 &= U\,1.2\left(\frac{U\,t}{C_D\,D}\right)^{-\frac{1}{2}} && (3.16)\\
u_1 &= U\,0.35\left(\frac{U\,t}{(C_D\,A)^{\frac{1}{2}}}\right)^{-\frac{2}{3}} && (3.17)
\end{aligned}
$$

for plane and axi-symmetric wakes respectively. In this fixed plane the velocity u_1 is the actual velocity at the center line, not the velocity deficit, since the body fixed coordinate moves with a velocity U with respect to the fixed system. Table 3.4 lists the resulting velocity for the cylinder (axi-symmetric) and a strut (plane) at t=240 s. The tow speed is set to $U = 2.5$ ms^{-1} and it is assumed that the diffusion in the fixed plane is not affected by the fact the the motion of the cylinder actually has stopped at some time $t < 240$.

Table 3.4: *Estimated residual velocity u_1 after 4 minutes.*

	C_D	d/A	u_1
Test Cylinder	0.01	$\pi dL = 0.32\ m^2$	0.002
Strut	0.1	0.01 m	0.004

The result for the strut is then used in table 3.3. There is also the possibility of residual flow due to remaining waves, but since these could not be observed this is neglected.

Generated Waves (B_{05}) The depth at which the cylinder is towed is a trade off between rigidity of the model and the influence of the free surface. In this case the cylinder was towed at a depth of 0.4 m, or 8 d. The velocity amplitude under a linear free surface wave at a given depth is

$$u_A = \sqrt{kg}\zeta_A e^{-kh} \tag{3.18}$$

where $h = 0.4$ m is the tow depth, $\omega = \sqrt{gk}$ is the circular frequency of the wave, and ζ_A is the amplitude of the wave elevation at the surface. The expression assumes infinite water depth and that the wave elevation is small. The wave number is given by $k = \frac{2\pi}{\lambda}$ where the max wave length is $\lambda = 2\pi\frac{U^2}{g}$ for transverse waves and $\lambda = \frac{4\pi}{3}\frac{U^2}{g}$ for divergent waves (Faltinsen 2004). Low wave numbers means slower decay with depth, so the transverse waves should be critical. On the other hand, the only waves that could be observed during the experiment were divergent waves from the struts. The Froude number for the struts is 1.84 for $U = 1.0$ ms^{-1} which is in a range where the divergent waves are dominant (Faltinsen 2004). By observing the wash on the tank walls, it was concluded that the wave amplitude never exceeded 5 cm. The bias limit is then estimated by:

$$\zeta_A = 0.05 \text{ m} \quad (3.19)$$

$$k = \frac{3}{2}\frac{g}{U^2} \quad (3.20)$$

$$B_{05} = \sqrt{\frac{3}{2}} U \zeta_A e^{-kh} \quad (3.21)$$

The second parameter in the dynamic pressure is the water density. The density and viscosity of the water in the tank used for calculating dynamic pressure and Reynolds number are given in table 3.1. These values are based on a measured water temperature of 18.2 °C and taken from tables used at MARINTEK. The variation of the temperature in the tank is very low, so the same temperature is used for all days. The biases are:

Density	$B_{06} = 0.1 \ \frac{Kg}{m^2}$
Dynamic Viscosity	$5.0 \times 10^{-9} \ \frac{m^2}{s}$

The dynamic viscosity is only used when calculated Reynolds number, and is not included in the error estimate. .

3.2.4 Precision and bias limits for alignment and dimensions

Alignment The yaw angle was set manually using a fixed protractor. The angle was set by the same person all day, ensuring that the same reference was used each time. The bias limit was then estimated to

$$B_{06} = \pm 0.25^\circ \quad (3.22)$$

Running both directions with zero angle of attack revealed no difference in z-direction force thus no error in pitch alignment could be observed. Since such forces may be very small, a precision error equal to the yaw precision are applied anyway.

Model dimensions (B_{07}) All dimensions are kept constant during analysis, thus there should be no precision errors. The length and diameter of the test section were measured to an accuracy of ±0.5 mm. Then

$$B_{07} = 0.5\text{mm} \quad (3.23)$$

3.2.5 Influence Coefficients

From chapter 2 the influence coefficient becomes

$$\kappa_i = \frac{\partial \hat{C}_j}{\partial Y_i} \quad (3.24)$$

where j refers to index and Y_i is the parameters in equations (3.2) - (3.6) . Below, the parameters are index by the alphabet rather than numbers, to separate from error source indexes. For normal forces ($j = 2, 3$) the sensitivity to variation in a single sensor is

$$\kappa_a = \frac{\partial}{\partial F_y^f}\left(\frac{F_y^a + F_y^f}{\frac{1}{2}\rho U^2 \ dL}\right) = \frac{1}{\frac{1}{2}\rho U^2 \ dL} \quad (3.25)$$

and similar for F_y^a, F_z^z and F_z^a. For the moments ($j = 5, 6$), the equations are

$$\kappa_a = \frac{\partial}{\partial F_y^f}\left(\frac{-F_y^a + F_y^f}{\frac{1}{2}\rho U^2\ dL}\right) = \frac{1}{\frac{1}{2}\rho U^2\ dL} \tag{3.26}$$

and so on.

For error in the velocity the sensitivity is

$$\kappa_b = \frac{\partial}{\partial U}\left(\frac{F_y^a + F_y^f}{\frac{1}{2}\rho U^2\ dL}\right) = -2\frac{F_y^a + F_y^f}{\frac{1}{2}\rho U^3\ dL} \tag{3.27}$$

for both normal forces and moments.

The sensitivity to variation in density is

$$\kappa_c = \frac{\partial}{\partial \rho}\left(\frac{F_y^a + F_y^f}{\frac{1}{2}\rho U^2\ dL}\right) = -\frac{F_y^a + F_y^f}{\frac{1}{2}\rho^2 U^2\ dL} \tag{3.28}$$

and finally for variation in diameter

$$\kappa_d = \frac{\partial}{\partial d}\left(\frac{F_y^a + F_y^f}{\frac{1}{2}\rho U^2\ dL}\right) = -\frac{F_y^a + F_y^f}{\frac{1}{2}\rho U^2\ d^2 L} \tag{3.29}$$

and similar for variation in length.

The angle of attack α is not included in the reduction equations, so the sensitivity cannot be expressed this way. But since the angle of attack is varied, the relationship between the force and the angle of attack is known from the experiment. This of course is the reason for doing the experiments in the first place. The sensitivity κ_e can therefore be estimated by a numerical derivation of the measured results, with respect to the given angle of attack.

3.2.6 Total error estimates

To avoid division by zero when calculating a relative error, only $\alpha \geq 1°$ are included in the following results. Figure 3.5 shows the relative errors for C_{n2}, i.e. the in-line normal force coefficient, calculated based on the forward runs the third day. This represents a first order replication approach. The bars gives the contributions from the source described above. The part of the bars representing force and dynamic pressure (*Dyn. Pres.*) includes both precision and bias errors for these sources. The solid line gives the total error from equation (2.50), the quadratic sum of the error contributions.

Figure 3.6 gives the relative errors from the second order replication. In this case a coefficient is calculated for each run, and the precision error is based on the variation of these values. Six repetitions are assumed for all angles. By repeating the test series errors due to variation of the set angle and the residual velocity will be included in the precision part, so B_{04} and B_{07} are not included in the bias error estimates. This is the main reason for repeating the experiments. Note the difference in legend between the two plots. For second order replication there is only one precision error and it is given separately. The remaining sources are all bias errors.

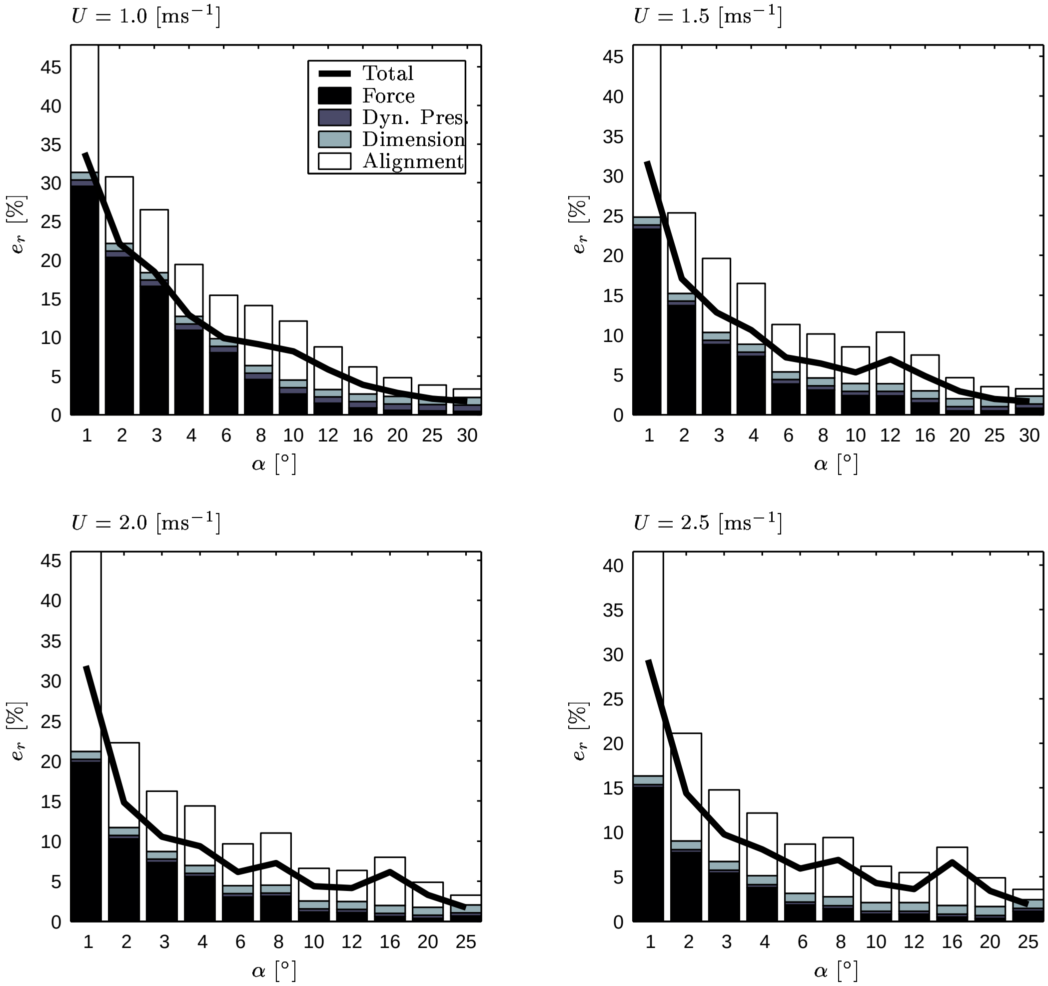

Figure 3.5: *Relative errors based on first order replication analysis. Calculation is for* C_{n2}.

Comparing the two methods, the first order replication gives high errors for low angles while the errors are in the same range for medium and high angles. Particularly at the lowest angles it seems that the error due to variation in angle of attack is lower than the estimate in B_{07}. For higher angles the comparison is reasonable, which hopefully indicates that no large error sources are omitted in the analysis. Note that even when the experiments are repeated, the bias error is estimated to contribute 10-15% of the total measurment error.

The errors included with the results below are from second order approach, if not noted otherwise.

3.3 Results

The measured results are presented in plots as function of the angle of attack, with bars representing the 95% confidence interval. Also see appendix B for the results in tabular form. Major findings in the results are discussed in the following sections.

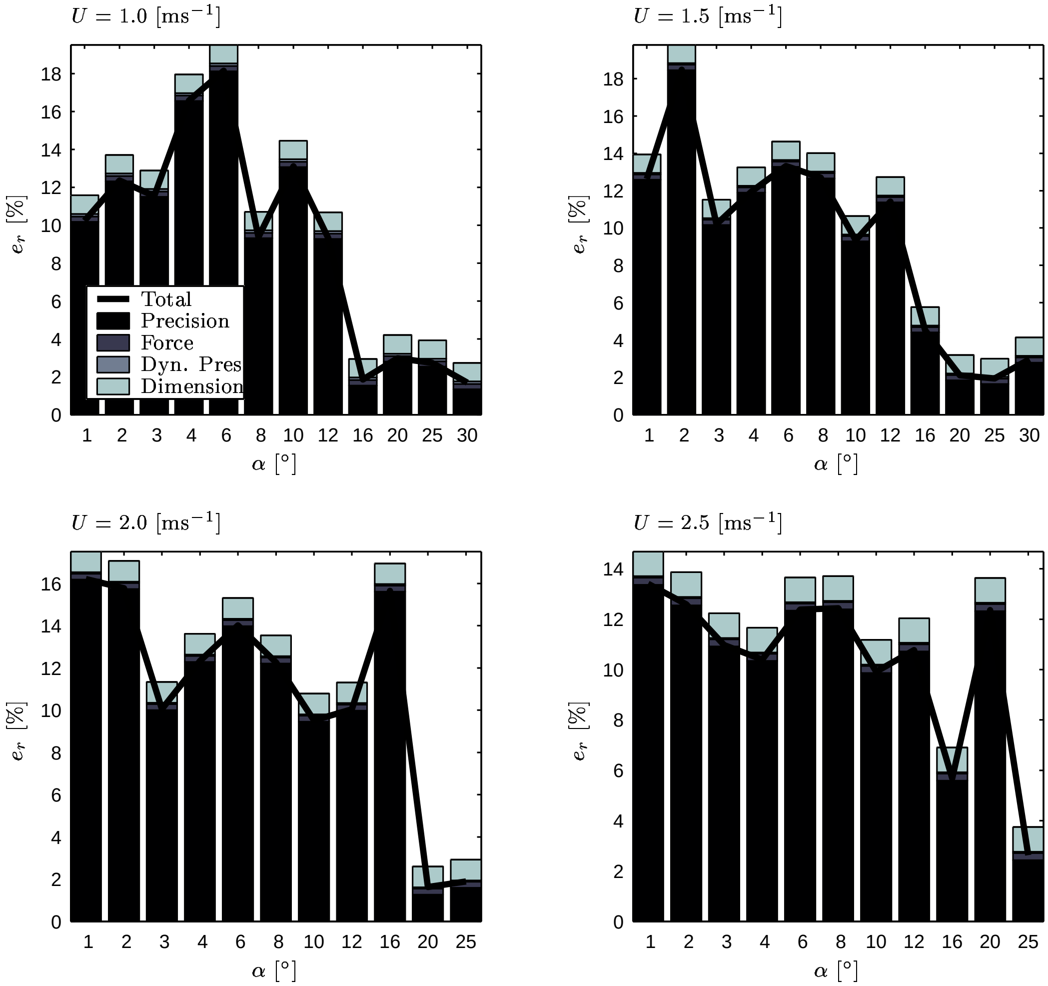

Figure 3.6: *Relative errors based on second order replication analysis. Calculation is for* C_{n2}.

3.3.1 Results from experiments in the Towing Tank

The results from towing the cylinder in the large towing tank are plotted in figures 3.7 - 3.10. In this case the cylinder was rotated in yaw only. From these results there seems to be a change in flow pattern somewhere around 6°, and again between 10 and 20 °, depending on tow speed. In the low region the normal force is almost linear with the angle, while the bi-normal force is of the same order as the normal force. This region is further discussed in following sections on flow patterns in pitch and yaw and modeling of the normal forces for low angles. In the intermediate region the normal force looks more like a parabola. The bi-normal force is almost constant, but is now small compared to the in-line direction. At the highest angles it almost looks linear again. Here the bi-normal force changes sign, and becomes irregular. The shift is assumed to be related to the Reynolds number of the longitudinal flow, as will be discussed in the section of normal forces for higher angles of attack. For all regions the moments are well within the error limits of the measurements, and any conclusions based on this must be stated with care.

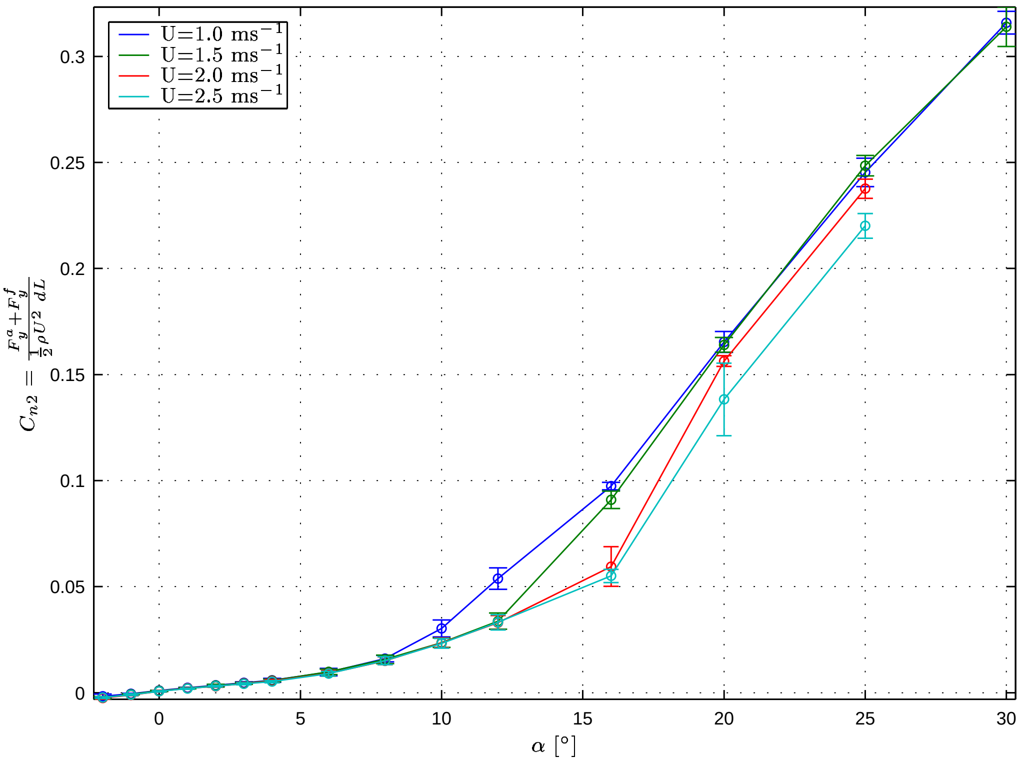

Figure 3.7: *Normal Force coefficient when rotating in Yaw: C_{n2}. Results from towing tank. Bars represents the 95% confidence interval*

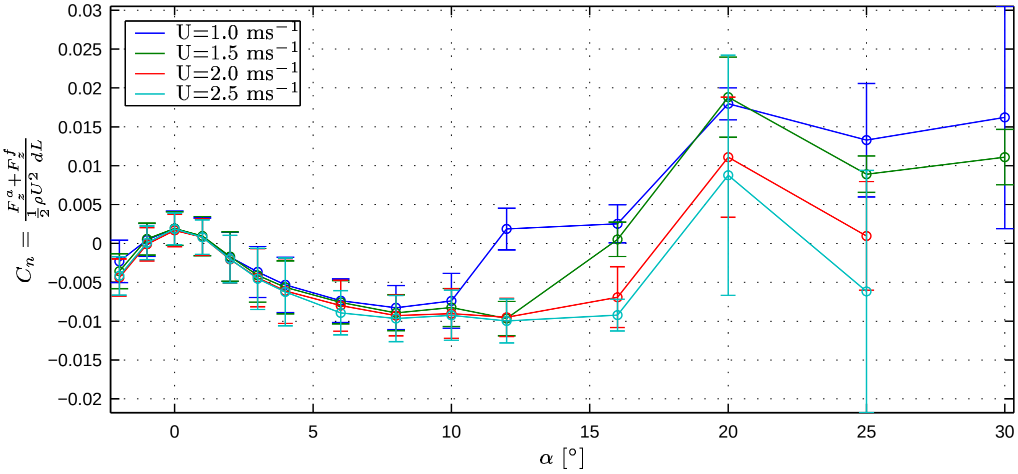

Figure 3.8: *Bi-normal Force coefficient when rotating in Yaw: C_{n3}. Results from towing tank. Bars represents the 95% confidence interval*

3.3.2 Results from MCLab

Figure 3.11 and figure 3.12 gives the results from the runs in the MCLab, rotating the cylinder in pitch. In this case the maximum angle was limited to 12 °in order to avoid interference

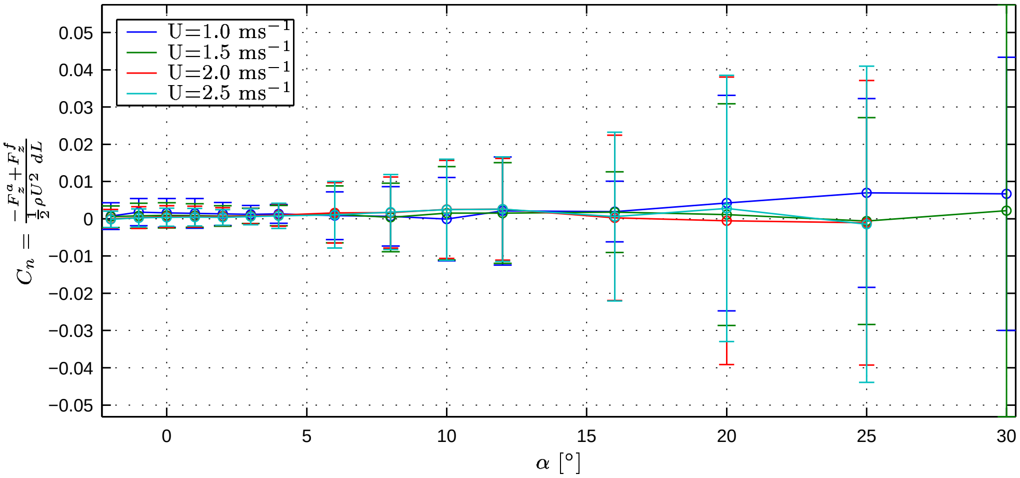

Figure 3.9: *Bi-normal moment coefficient when rotating in Yaw: C_{n5}. The moment is taken about $\frac{L}{2}$. Bars represents the 95% confidence interval*

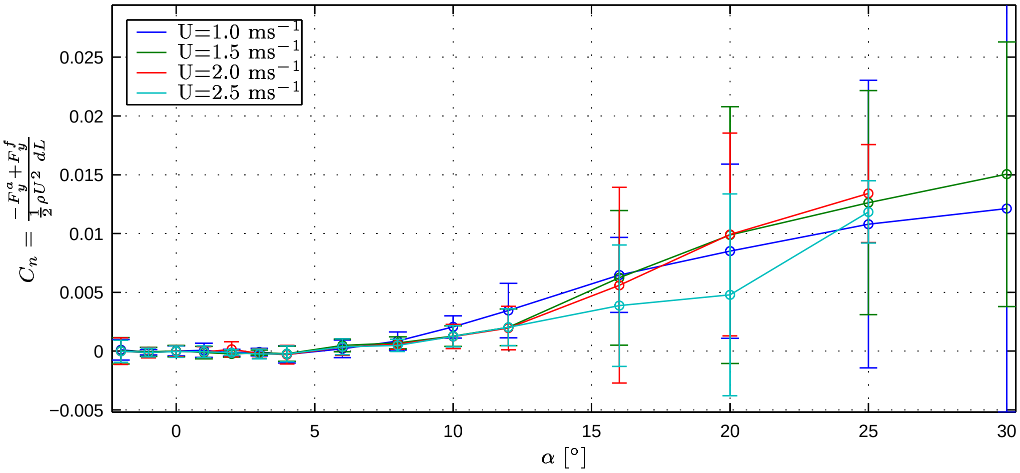

Figure 3.10: *Normal moment coefficient when rotating in Yaw: C_{n6}. The moment is taken about $\frac{L}{2}$. Bars represents the 95% confidence interval*

with the surface. All runs were repeated three times, and selected runs ($\alpha = 2°, 6°$,and $12°$) six times. Again a zero offset corresponding to a C_{n3} value of 0.001 was found. Since this is the important result this time, the offset is removed for all data, but included in the bias error estimate ($B_{03} = 0.0015$, as before). Otherwise the errors are calculated as for 2'nd order replication above, with six repetitions. Using the MCLab carriage, th uncertainty of orientation of the cylinder almost zero, thus the error level is slightly less for these experiments than those from the towing tank. Results from s single series rotating in yaw is also included in the figures, assuming the same error level as when rotating in pitch.

The results from rotating in yaw is a least qualitatively the same as found from the towing tank experiments, while the normal force when rotating in pitch is significantly lower.

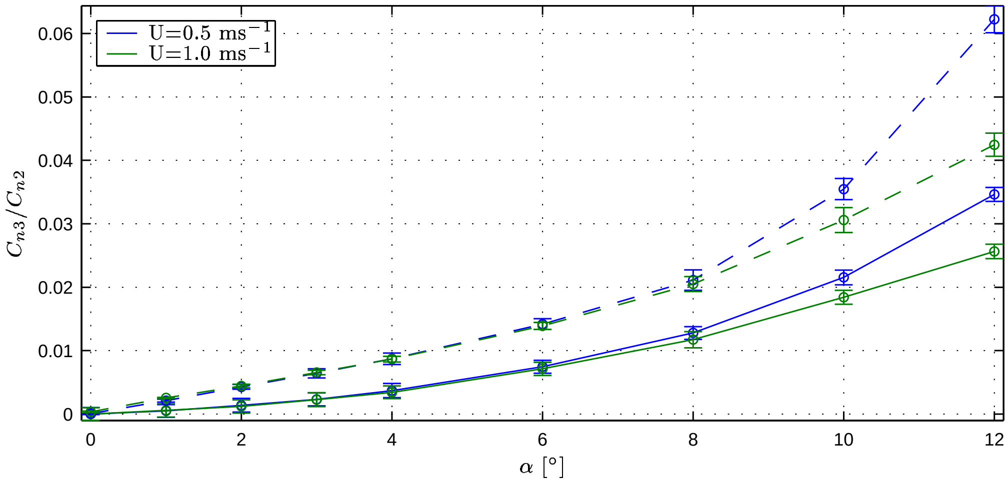

Figure 3.11: *Normal force coefficient from experiments in MCLab: — Rotation in Pitch (C_{n3}); -- Rotation in Yaw (C_{n2}). Bars represents the 95% confidence interval*

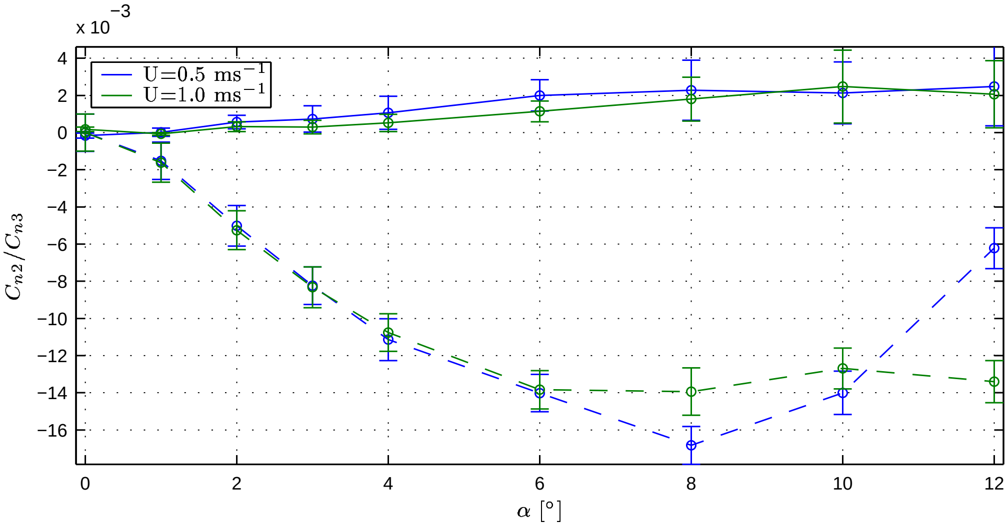

Figure 3.12: *Bi-normal force coefficient from experiments in MCLab: — Rotation in Pitch (C_{n2}); -- Rotation in Yaw (C_{n3}). Bars represents the 95% confidence interval*

This discrepancy is true also for the bi-normal force. The dependence of tow speed for $\alpha > 6$ also seems to be less pronounced when rotating in pitch, see for example the bi-normal forces in figure 3.12.

As was the case for the tow tank experiments, the measured moment coefficient where small an with large errors, so the results are not plotted here. They are on the other hand included in the tables in appendix B.

3.4 Flow pattern in pitch and yaw

In the results from the MCLab, it becomes clear that the measured forces are not equal when rotating in pitch rather than yaw. Both normal and bi-normal forces are larger for the yaw rotation case in the range measured. The difference does not seem to be a measurement error, particularly since the yaw rotation results in the tow tank are reproduced in the MCLab.

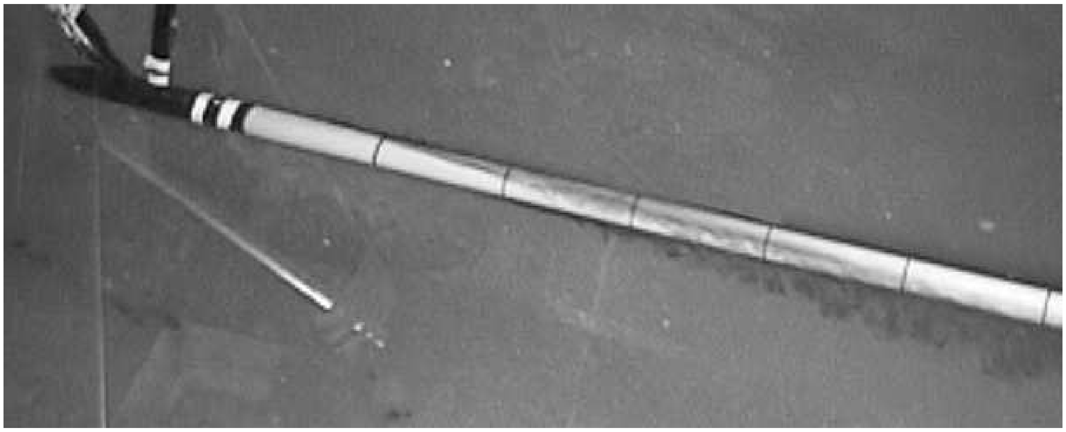

Figure 3.13: *Vortex shedding when rotating in yaw. Tow speed is* $U = 0.2\ ms^{-1}$ *and angle of attack is* $\alpha = 10°$. *A dominating vortex is developed underneath the cylinder while a small vortex that stays close to the cylinder on the lee side is developed on the top*

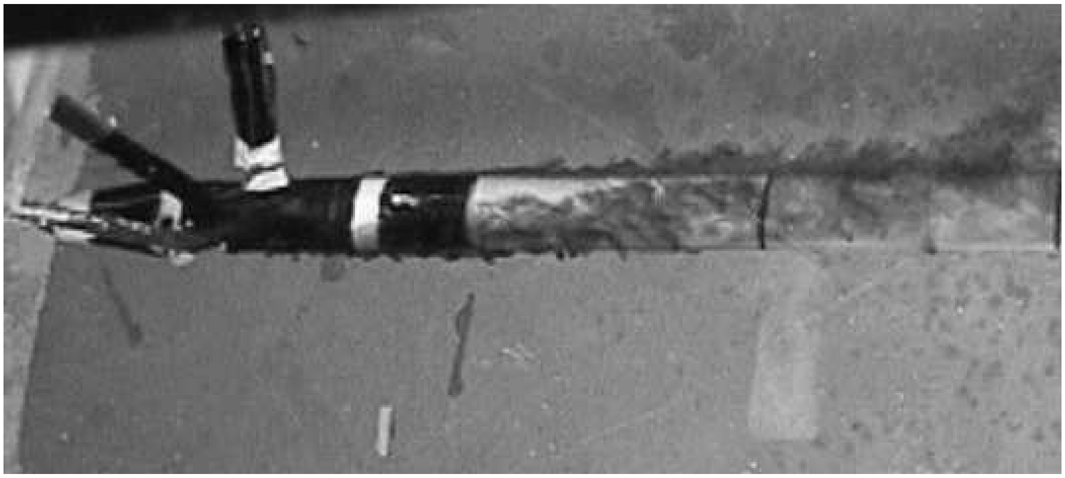

Figure 3.14: *Vortex shedding when rotating in pitch. Tow speed is* $U = 0.2\ ms^{-1}$ *and angle of attack is* $\alpha = 10°$. *A symmetric pair of vortices are formed on each side of the cylinder*

To investigate this, the flow field on the cylinder were visualized by releasing dye (potassium permanganate) on the lee side of the cylinder. At low tow speeds it was possible to observe a distinctive difference in the flow pattern when rotating in pitch rather than yaw. For higher, turbulent flow, good visualization were not achieved. In figure 3.13 and figure 3.14 it should be possible to see that in the case of yaw rotation the initial vortex pair is not symmetric, but dominated by the vortex formed underneath the cylinder. In this case the dye was released at the same axial (x) location as the struts, where a vortex sheet already exists. When rotating in pitch, the initial vortices are close to symmetric. Here the dye is released at the nose, so the figure shows the vortex formation from the start. Assuming the vortex patterns are the same for higher tow speeds, this explains why there is a much larger bi-normal force in the yaw rotation case, but it does not necessarily explain the difference in normal force, see e.g the discussion in Hoerner and Borst (1985, ch. XIX).

The difference in flow pattern is most likely due to the struts. When rotating in yaw, the upstream end is not symmetric about the plane of the normal direction (the horizontal plane in this case) since the supporting struts are placed on the upper side of the cylinder. It seems that this influence the formation of the first set of vortices and thus the flow over the full length of the cylinder. In the pitch rotation case, the upstream end is close to symmetric in the plane of the normal force (now the vertical plane), and so is the initial vortex formation. The last case then looks more like the $2D + t$ approximation in chapter 2.

3.5 Normal Forces: $\alpha \geq 6°$

In chapter 2 a general formulation of the viscous normal force was written:

$$
\begin{aligned}
F_n &= C_n \, \frac{1}{2} \rho V^2 \, d && (3.30) \\
C_n &= C_{n1} \sin(\alpha) + C_{n2} \sin^2(\alpha) && (3.31)
\end{aligned}
$$

where F_n is the force per unit length. In the stationary case the relative velocity equals the tow speed, so that $V = U$ in the following expressions.

The two models of normal force described in chapter 2 both utilized the independence principle, i.e the flow over the cylinder is decomposed in a longitudinal and a transverse direction and studied separately. The normal force is then a function of the cross flow drag coefficient, calculated from the normal component of the velocity:

$$C_d = \frac{F_n}{\frac{1}{2}\rho \left(U \sin(\alpha)\right)^2 \, d} \tag{3.32}$$

In the frame work of equations (3.30) - (3.31) this corresponds to $C_{n1} = 0$ and $C_{n2} = C_d$. Figure 3.15 presents the experimental results for this coefficient. The figure clearly illustrates a problem with the independence principle: The drag of a smooth cylinder in 2-D has a shift from a value of approximately $C_d \simeq 1.2$ for $R_{ed} < 1 \times 10^5$ called the subcritical region to $C_d \simeq 0.7 - 0.8$ for $R_{ed} > 1 \times 10^6$, the supercritical region (These values depends highly on the roughness of the cylinder, but again the tested cylinder will be assumed smooth). For Reynolds number between these limits, the transcritical region, the drag coefficient is even lower Blevins (1992). The cross flow Reynolds number for the test cylinder is given in the left part of figure 3.16, and is in the subcritical region for all cases. But the change in value of the coefficient is usually explained by change from laminar to turbulent boundary layer prior to separation. If the flow in the axial direction has high enough Reynolds number the boundary layer is turbulent anyway.

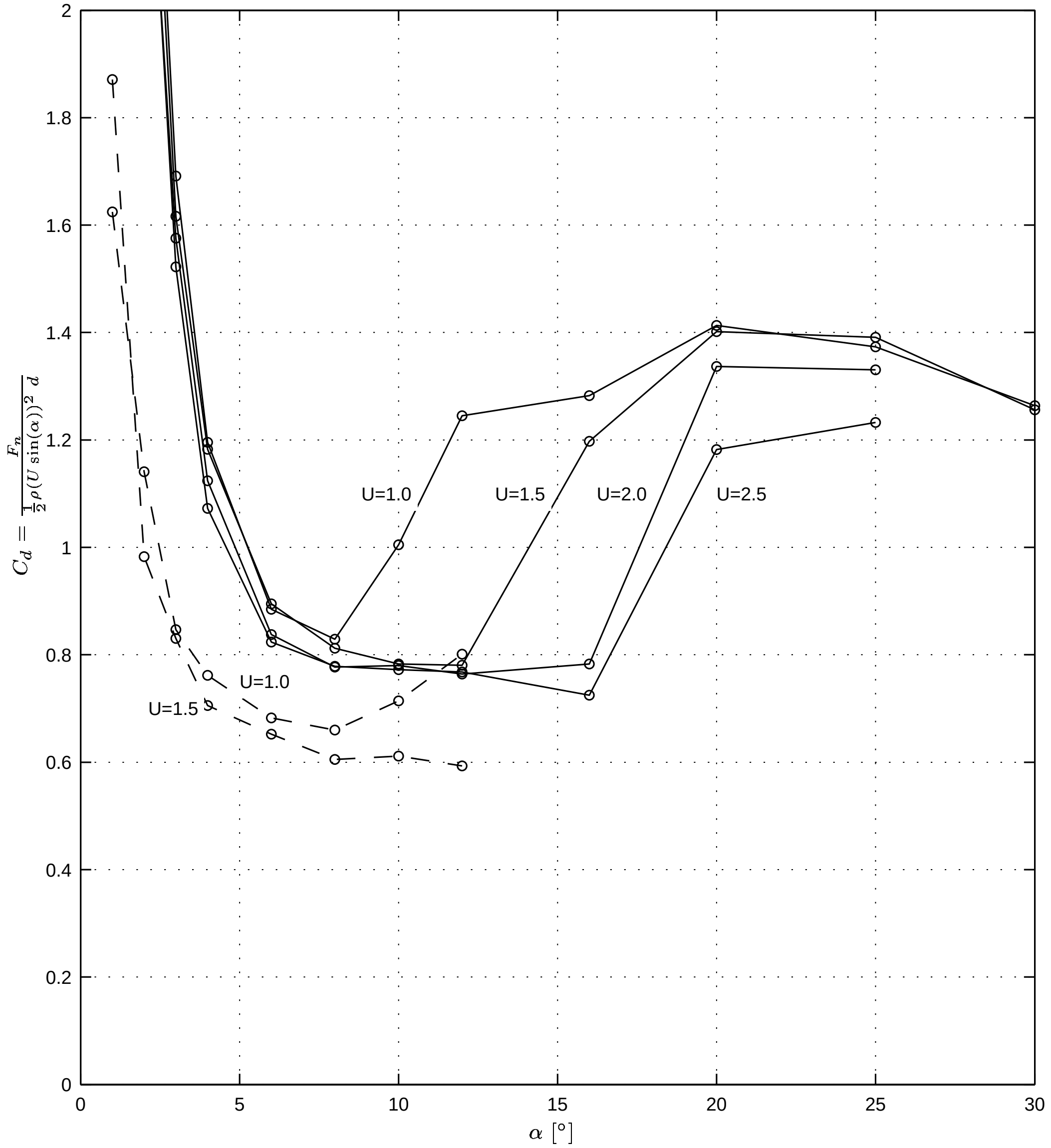

Figure 3.15: *Cross flow drag coefficient:* — *Rotation in yaw;* -- *Rotation in Pitch*

The question is then if the change in coefficient value would happen at all. From figure 3.15 it is obvious that some shift do occur, for angles between 5 and 15 degrees the C_d values tends toward the trans- and supercritical values while for higher angles it tends toward the subcritical value. The longitudinal flow is described by the Reynolds number based on length, given in the right part of figure 3.16. Unfortunately it is not given whatever these Reynolds numbers results in a turbulent boundary layer or not. Considering figure 2.3, dependence of diameter for the axially symmetric boundary layer is given by the parameter R_a. This is the Reynolds number based on cylinder radius, thus $R_a = 0.5\ R_{ed}$. For the experiment, this value is in the order 10^4. For $R_x = R_{eL}$ and $x/d < 100$ in figure 2.3 it can be concluded that the boundary layer for the test cylinder is close to that of a flat plate, and not much influenced by the transverse curvature.

The transition from laminar to turbulent boundary layer on a flat plate takes place somewhere in the region $0.5 \times 10^6 < R_{ex} < 5 \times 10^6$ (Blevins 1992, Fig 10-10). This is the exact region of the Reynolds number based on length in figure 3.16. This very strongly suggest that the boundary layer due to longitudinal flow do influence the flow field and force in the normal direction.

When designing the experiment it was assumed that the forward support structure would create enough disturbance to ensure a turbulent boundary layer, but from the above discussion this probably was a little optimistic. Note that the shift in C_d value does not take place for the same longitudinal Reynolds number for different tow speeds, so Reynolds number is not the only parameter involved in the shift. From figure 3.7 the measurement error increase slightly for the higher angles, but not enough to conclude that the shift is highly unstable for a given tow speed.

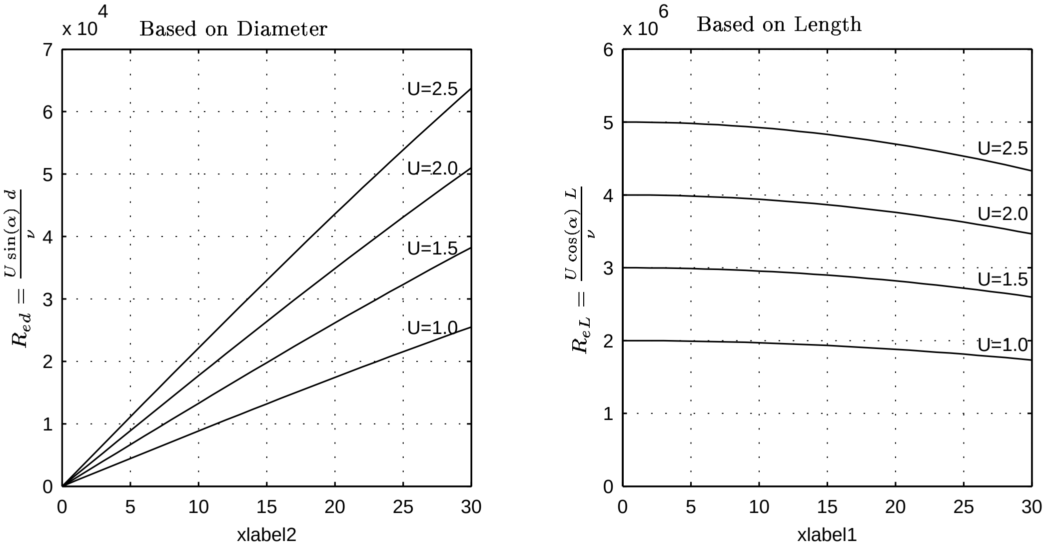

Figure 3.16: *Reynolds numbers for the rigid cylinder at constant angles.* R_{eL} *is based on test section length.*

The above discussion is mainly based on the results from rotation in yaw. Although the data for rotation in pitch is limited to angles $\alpha \leq 12^\circ$, it seems that the C_d values remains on the trans- and supercritical range for higher angles in this case. The difference in results from yaw and pitch rotation mentioned above is clearly seen in figure 3.15. Allowing for some variation in the C_d values, the difference seems to roughly correspond to the ratio between the cross flow principle and the $2D + t$ method given in figure 2.9. It then seems like the onset of an asymmetric flow (rotation in yaw) leads to a situation where the flow pattern associated with the cross flow principle becomes dominating at a lower angle than if the initial vortex pair is symmetric (rotation in pitch). This has a parallel in CFD modeling of flow over a cylinder, where a slight asymmetry is used to speed up the convergence to a steady state flow pattern (Comsol AB 2000).

3.6 Normal forces: $\alpha < 6°$

The results for angles larger than about $5° - 6°$ seems to be in reasonable agreement with the independence principle, when proper Reynolds number are used. Unfortunately this is not the case for low angles, where the cross flow drag coefficient goes to infinity as the angle approaches zero. This is expected to happen, since the denominator of equation (3.32) goes to zero as α goes to zero. When the transverse component of the velocity becomes so low that the flow does not separate, the skin friction dominates the force. The skin friction is proportional with $\sin(\alpha)$ rather than $\sin^2(\alpha)$, so the coefficient in figure 3.15 should have a singularity at $\alpha = 0$.

But this should happen for lower angles than indicated by in figure 3.15. In Schlichting (1979) it is given that for an impulsively started cylinder in 2D cross flow the separation starts at $s = \frac{2Ut}{d} = 0.351$, while in figure 2.6 the turn around is at $s \simeq 1°$ Following the coordinate mapping in the $2D + t$ method from chapter 2 this corresponds to $\alpha \simeq 0.6°$ at the downstream end of the test section. The distance from the nose to the start of the test section is 0.39 m, so $s = 1$ corresponds to $\alpha \simeq 3.6°$ at the start of the test section. In figure 3.15 the curves turn upward at about 6°, where separation should be fully developed along the cylinder.

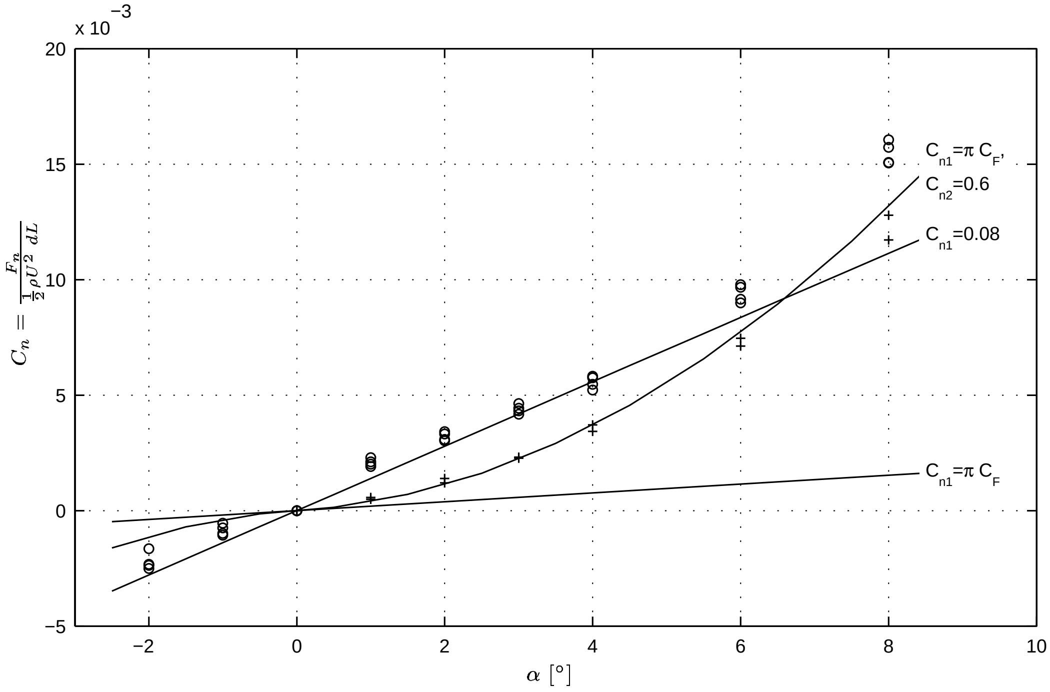

Figure 3.17: *Normal Force coefficient at low angles: ○ Rotation in yaw; + Rotation in pitch*

The measured normal force coefficients for small angles are plotted in figure 3.17. The solid lines corresponds to $C_{n2} = 0$ and given C_{n1} in equation (3.31). The value $C_{n1} = \pi C_F$ is the result from skin friction, suggested by Taylor (1952). For the rotation in pitch the linear the sum of a skin friction and a $2D + t$ term, that is $C_{n1} = \pi C_F$ and $C_{n2} = 0.6$ in equation (3.31) seems to fit the data well within the error limits.

For the rotation in yaw on the other hand, there is a linear trend with $C_{n2} \simeq 0.08$ from curve fitting. No good explanation for this have been found, except that it seems related to the asymmetric separation of vortices. In the case of oscillating cylinders discussed in the following chapters, both the asymmetry and the linear force coefficient is present, indicating that this is an often encountered phenomena at low angle of attack.

Chapter 4

Oscillating rigid cylinder

The next logical step in investigating the hydrodynamic force on a streamer is to study the forces on an oscillating rigid cylinder, rather than the stationary angle of attack case discussed in the previous chapter. Again the focus will be on experimental results. These tests were performed in May 2002, which is before the stationary tests in the towing tank. This was also the first attempt to utilize the multi degree of freedom forced motion capability of the MCLab carriage, revealing an unwanted limitation in the original carriage control system. The available data is therefore limited to one rather low frequency. Still, it seems that some rather important conclusions can be drawn from the results.

4.1 Measured forces

The results given in this section is the peak to peak amplitudes of all tested combinations of amplitude and forward speed. In addition mean force traces of selected cases are included for comparison with force models of an oscillating cylinder presented in sections below.

4.1.1 Set up and errors

The model cylinder was the same as in chapter 3, without some of the stiffeners on the strut structure. The oscillation then had to be performed in the vertical direction (z-direction in figure 3.2), since horizontal motion (y-direction) would results in large deflections in the cylinder supports.

In principle, the carriage in the Marin Cybernetics Laboratory allows forced motion of a model in 5 degrees of freedom. At the time of these tests the control system of the carriage did not allow accurate control of the velocities of each axis independently. The control system was taken from a milling machine, in witch case accuracy in velocity and acceleration was sacrificed for accuracy in position. The ability to create a combination of a fixed forward speed and a harmonic vertical motion were therefore limited, and some oscillations in the forward speed did occur. Measurements were made for five velocities ranging from zero to one meter per second and 8-9 different amplitudes of oscillation, while the frequency were kept constant at $f = 0.2$ Hz for all experiments. Then both KC number and cross flow Reynolds numbers changes when the amplitude changes.

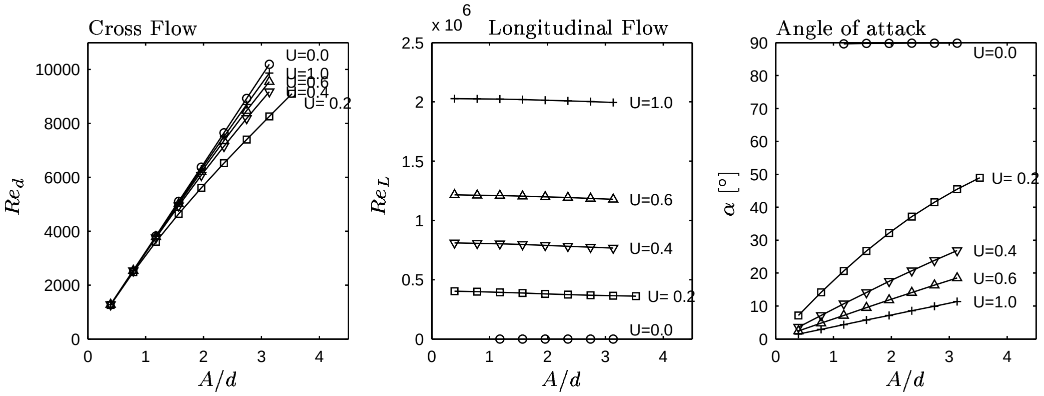

Figure 4.1: *Reynolds numbers and angle of attack as function of oscillation amplitude (A) to cylinder diameter (d) ratio. U is the tow speed in ms*$^{-1}$*. All numbers are based on measured amplitudes.*

Figure 4.1 plots the Reynolds number and amplitude of the angle of attack versus the position amplitude to diameter ratio A/d. The cross flow Reynolds number is calculated from the measured velocity amplitudes. The results is fairly constant, with the exception of tow speed $U = 0.2$ ms^{-1}, where the deviation in velocities were largest. All cross flow Reynolds numbers are in the subcritical regime. The longitudinal Reynolds number are calculated from the mean of the measured tow speed. Again the variation is small, and the effect of some variation of the forward speed is not addressed explicitly in the error analysis. Any effects should be included in the precision error. The longitudinal Reynolds numbers are mostly below the transition region, so the boundary layer should be laminar. The exception is $U = 1.0$ ms^{-1} where the boundary layer may be turbulent over large parts of the cylinder. The angle of attack is the inverse tangent of the cross flow velocity amplitude divided by the mean tow speed. It ranges from about 2° for high tow speed and low KC numbers to 90° for zero tow speed.

The peak to peak values are found by finding the difference between maximum and minimum measurements from each forced period, and taking the mean. The precision errors are taken as the variation of this mean. In most time series a total of 8-9 periods were measured, for high speed in two or more runs. The precision error is then calculated from equation (2.36).

Since the setup is the same, bias errors from the z-direction in chapter 3 are used for both the z-direction and y-direction. The motion here is in the z-direction, so the cylinder end effect is included in this direction. The values are given in table 4.1. Due to the very high accuracy of the carriage position control alignment errors are neglected. The tow speeds are lower, so the maximum forces are expected to be lower in this case than for stationary tow at high speeds and angles. Therefore the median values in table 4.1 are used for force measurements biases.

According to Sarpkaya and Isaacson (1981) the effect of roughness is not necessarily the same for an oscillating cylinders as it is for a cylinder in steady flow. Based on their discussion,

Table 4.1: *Bias errors for oscillating rigid cylinder.*

Source	index	Bias Limit	Unit
Vibration	B_{01}	0.008	N
Cylinder end	B_{02}	0.0022	N
Strut Wake	B_{03}	0.0015	N
Residual Flow	B_{04}	0.004	ms^{-1}
Generated Waves	B_{05}	0.2×10^{-3}	ms^{-1}
Density	B_{06}	0.1	Kg/m
Diameter	B_{07}	0.5×10^{-3}	m
Length	B_{08}	0.5×10^{-3}	m

the assumption of a smooth cylinder will still stand. This because the roughness in the current case is two orders of magnitude below the values discussed by Sarpkaya and Isaacson (1981). The mean tow depth was in this case 0.6 m, a little deeper than for the stationary case. The smallest gap between bottom or surface to occur in the experiments then was 0.4 m, giving a gap to diameter ratio of about 8. From experiments by Sarpkaya and Isaacson (1981) a ratio of two should be sufficient to avoid interference effects from a fixed surface, so the surrounding fluid is assumed infinite in extension.

This time the forces are presented directly, so a reduction equation is only involved to calculate the sensitivity of errors in dynamic pressure and dimensions:

$$\kappa_i = \frac{\partial}{\partial X_i}\left(1.2\frac{1}{2}\rho W_0^2\ dL\right) \tag{4.1}$$

where X_i is one of the parameters in the equation, corresponding to $i = 4-8$ in table 4.1. W_0 is the velocity amplitude and the drag coefficient of 1.2 is assumed conservative. For $i = 1-3$ and for the precision error, the influence coefficient is $\kappa_i = 1$. The total error can then be calculated as in described in chapter 2.

4.1.2 Force Amplitudes

The peak to peak amplitudes of the measured transverse forces are given in figure 4.2 and figure 4.3 and tabulated in appendix B. Inertia forces due to the dry mass of the test cylinder are calculated from the time derivative of the measured vertical velocity and the given mass. The result is subtracted from the measured force in the vertical direction before analysis so the forces discussed here should be the hydrodynamic forces only.

The general trend is that transverse forces decreases with increased tow speed, but not gradually.

The normal force (z-direction in this case), the peaks are notably reduced from $U = 0.0$ ms^{-1} to $U = 0.2$ ms^{-1}, then they actually increase again and is more or less constant for $U = 0.4$ ms^{-1} and $U = 0.6$ ms^{-1}, before there again is a noticeable reduction from $U = 0.6$ ms^{-1} to $U = 1.0$ ms^{-1}. The large change from no speed to some speed should be expected, based on the discussion in chapter 2 and realizing hat the KC numbers of these experiments are in the

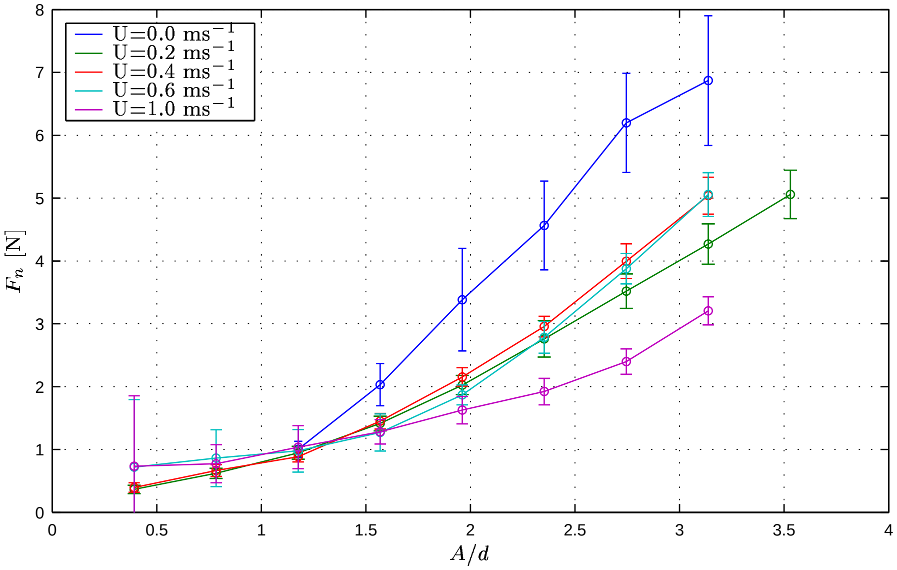

Figure 4.2: *Peak to peak amplitude of measured normal forces on a oscillating cylinder as function of oscillation amplitude. Frequency is constant:* $f = 0.2$ *Hz. Each curve corresponds to a tow speed in the axial direction and bars represent 95% confidence interval.*

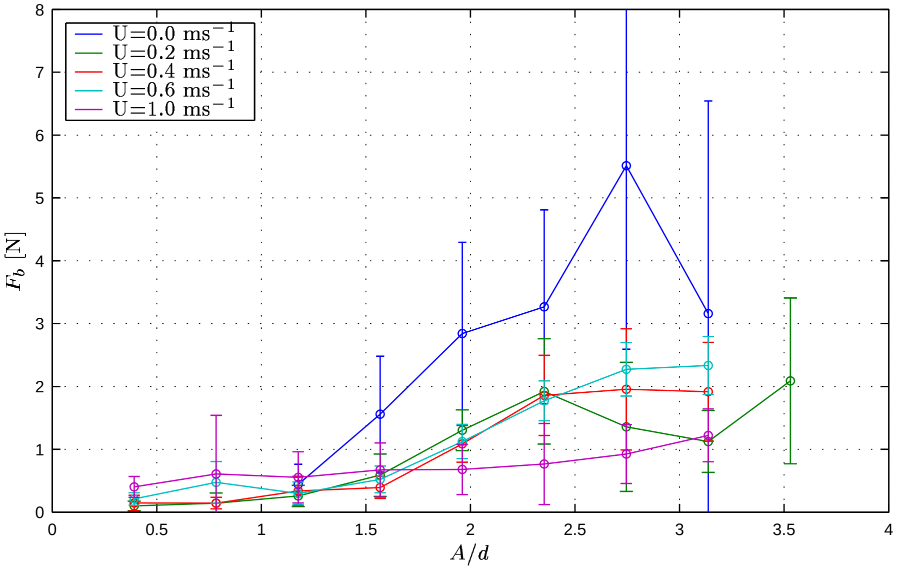

Figure 4.3: *Peak to peak amplitude of measured bi-normal forces on a oscillating cylinder as function of oscillation amplitude. Frequency is constant:* $f = 0.2$ *Hz. Each curve corresponds to a tow speed in the axial direction and bars represent 95% confidence interval.*

region with large KC dependence. It is more difficult to explain why the force increases again for higher tow speeds, except that the velocities increases and the angles of attack are in a region where cross flow principles becomes dubious. For $U = 0.6$ ms^{-1} the test section of the cylinder travels three quarter of its length during on half period of oscillation, so formerly shed vortices are returning to the cylinder downstream. For $U = 1.0$ ms^{-1} the cylinder travels longer than its own length during a half period, thus the inflow conditions should be close to free-stream for the full length of the cylinder and a difference from lower tow speeds should be expected. Also, for $U = 1.0$ ms^{-1}, the longitudinal Reynolds number is in the transition region, which may lead to a reduction in the normal drag force as shown in chapter 3.

In the y-direction, which is the bi-normal direction in this case, the force peaks are almost as large as for the normal force at low amplitudes, although the precision error is large so this is uncertain. When amplitude and/or forward speeds increases there is a shift where the bi-normal forces are reduced compared to the normal force.

These results will be further discussed in the following sections on force modeling.

4.1.3 Traces of normal forces

Traces of the normal forces over one period are given in figures 4.4 - 4.6 for three amplitudes and velocities. These results are the mean of all measured periods. The bars represents the 95% confidence interval. The large scatter early in the time series are mainly due to small differences in phase, while scatter of the peak values are lower. The forced normal velocity is also included in the plots.

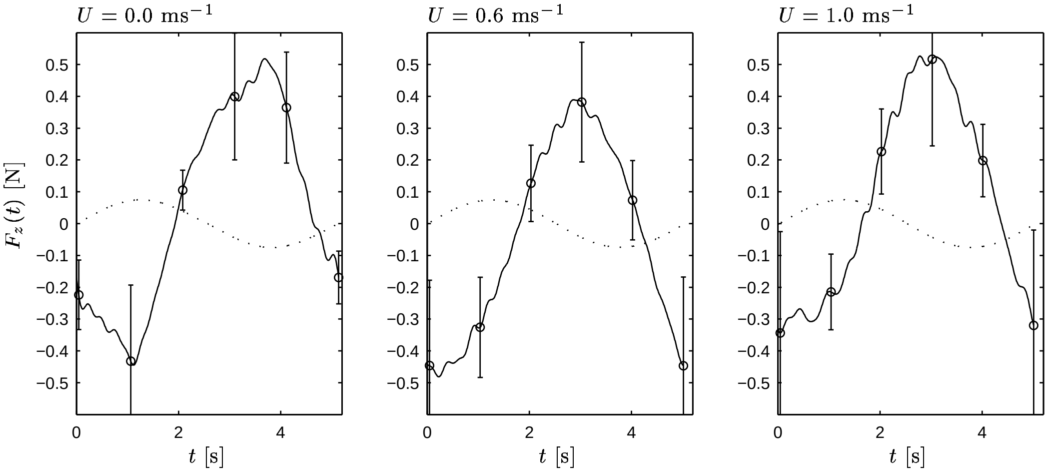

Figure 4.4: *Time series at $A/d = 1.17$: — Measured force, bars represent 95% confidence interval; -- Forced normal velocity (w).*

According to Morison's equation described in chapter 2, the hydrodynamic force is the sum of a term in phase with the acceleration and a term in phase with the velocity, the added mass and drag term, respectively. For harmonic oscillation these are 90°out of phase, so that the added mass force is maximum when the velocity is zero, while the drag force is maximum when the velocity is maximum. Relating the amplitude of the two terms gives for harmonic oscillation:

$$\frac{\omega^2 A C_a \pi \frac{d^2}{4}}{\frac{1}{2}(\omega A)^2 C_d\, d} = \frac{\pi}{2}\frac{C_a}{C_d}\frac{1}{\frac{A}{d}} \tag{4.2}$$

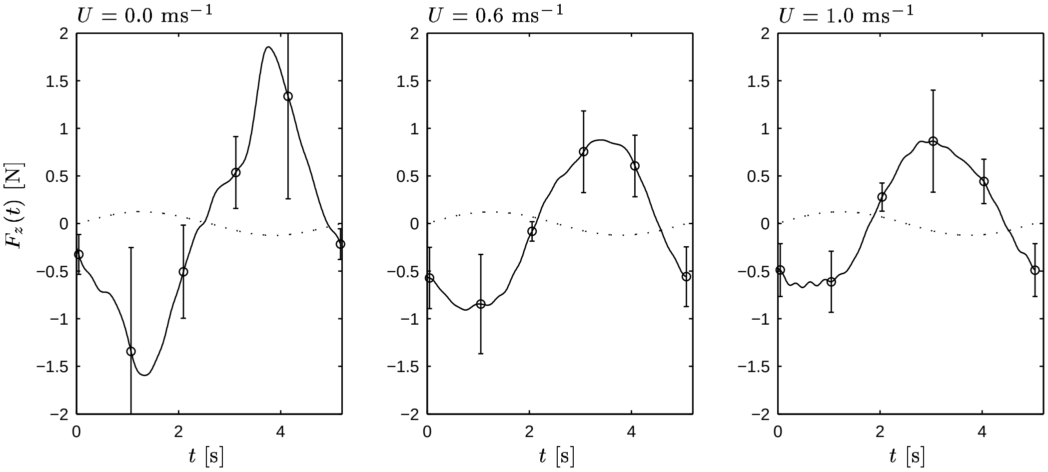

Figure 4.5: *Time series at A/d = 1.96: — Measured force, bars represent 95% confidence interval; -- Forced normal velocity (w).*

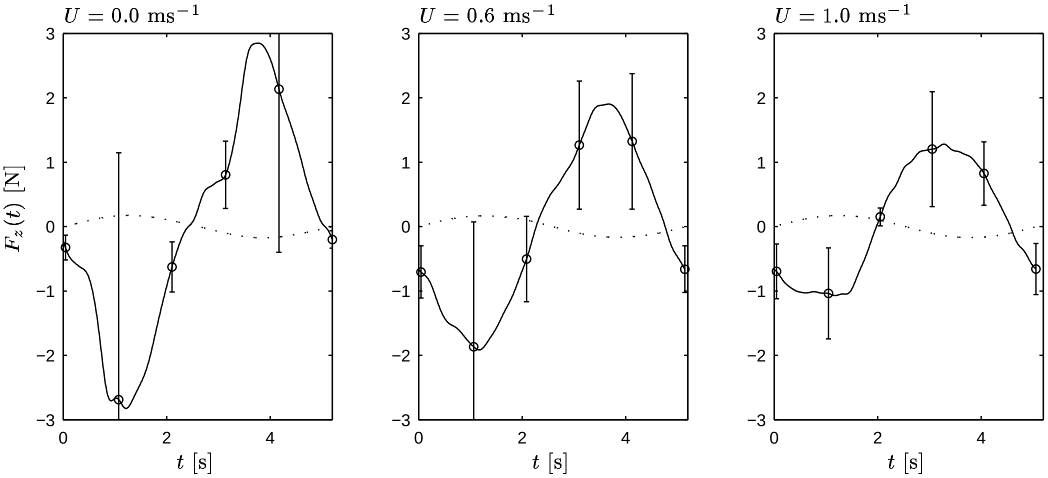

Figure 4.6: *Time series at A/d = 2.75: — Measured force, bars represent 95% confidence interval; -- Forced normal velocity (w).*

For low A/d ratios the force is the expected to be dominated by the added mass term, while for high amplitudes the drag term dominates. This can be seen in figures 4.4 - 4.6 for $U = 0$ ms^{-1}, where a peak develops as the amplitude increases. There is a large error for the value of these peaks, indicating the unstable nature of oscillating flow with shed vortices. But when the tow speed increases these peaks disappears and the time of the maximum force shifts to somewhere between the maximum acceleration and maximum velocity.

4.1.4 Traces of Bi-normal forces

From the discussion in chapter 3 it was expected that the bi-normal force should be about zero for high tow velocities and low amplitudes. Comparing angle of attack for stationary rotation in pitch with the angle of attack amplitude in figure 4.1 this should be the case for $U = 1.0$ ms^{-1}, except maybe for the largest amplitude. That this is not the case is shown already in figure 4.3 where the peak to peak values in bi-normal direction is about 1/3 of the normal force.

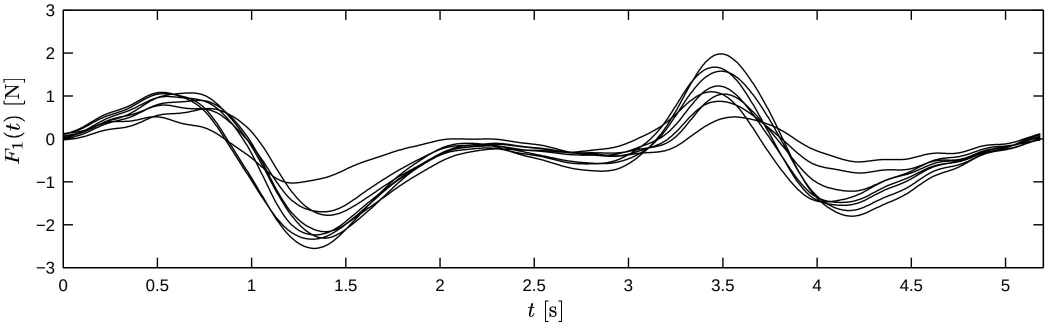

Figure 4.7: *Bi-normal force traces at* $A/d = 2.75$ *and* $U = 0.0$ *ms*$^{-1}$.

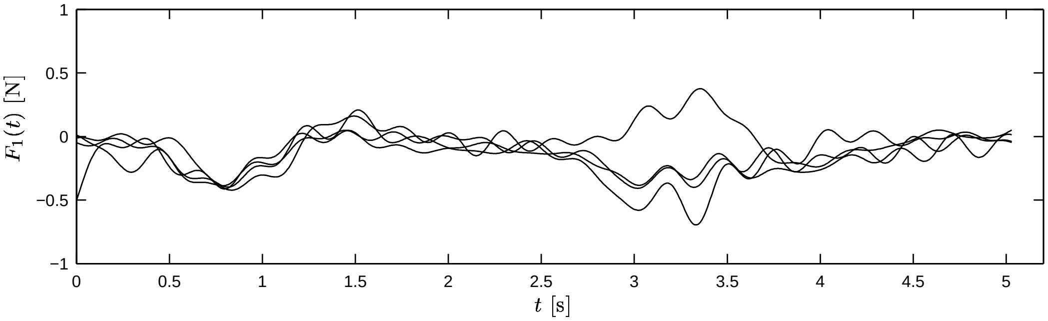

Figure 4.8: *Bi-normal force traces at* $A/d = 2.75$ *and* $U = 1.0$ *ms*$^{-1}$.

The measured bi-normal force traces are shown in figure 4.7 for zero tow speed and in figure 4.8 for $U = 1.0$ ms^{-1}. Here all measured periods of the time series are shown, to directly indicate the scatter. For $U = 0.0$ ms^{-1} the peaks has the same order of magnitude as the in-line forces. Using the root mean square (RMS) value of velocity and assuming Strouhal number $S_t = 0.2$ the vortex shedding period may be estimated by: $T_v = \frac{d}{S_t v_{rms}} = 2.04$ s. Allowing for a time interval around zero transverse speed where no transverse force is generated, this seems to fit with the measured trace.

For $U = 1.0$ ms^{-1} there seems to be only two peaks for every forced oscillation period, and the value is lower. Also, the direction of the side force is not entirely stable, for one of the measured periods the direction is opposite of the others. This again illustrates that the vortex formation is highly dependent on the surrounding flow. The high frequency oscillation evident in figure 4.8 is most likely some resonance frequency of the model setup as indicated by decay tests.

4.2 Normal force models

For a rigid cylinder of constant cross section the remaining term from the slender body force in chapter 2 is

$$F_{np} = -a\frac{\partial w}{\partial t} \tag{4.3}$$

where w is the normal component of the relative velocity. The viscous part of the force is given by equation (2.3):

$$\begin{aligned} F_{nv} &= -C_n \frac{1}{2}\rho V^2\, d && (4.4)\\ C_n &= C_{n1}\sin(\alpha) + C_{n2}\sin(\alpha)\left|\sin(\alpha)\right|| && (4.5)\\ \alpha &= \arctan\left(\frac{w}{u}\right) && (4.6)\\ V^2 &= u^2 + v^2 && (4.7) \end{aligned}$$

The normal force coefficient C_n is here given by a second order expansion in α, as suggested by Taylor (1952). The total force per unit length is the then the sum of these forces. The question is again the value of the coefficients.

4.2.1 Constant coefficients

From chapter 3 the coefficients should be:

$$\begin{aligned} C_a &= 1 && (4.8)\\ C_{n1} &= \pi C_f \ = 0.011 && (4.9)\\ C_{n2} &= 1.2 && (4.10) \end{aligned}$$

The C_{n2} values assumes high angles and laminar boundary layer. In order to compare this with measurements, the ratio of the model error and the measurement error for each case is plotted in Figure 4.9. See chapter 2 for a discussion of these quantities. If this ratio is less than unity the requirement in equation (2.62) is fulfilled and the force model is as good as the current data. It is here assumed that the force model is the only error in the numerical model. For e_{exp} the mean value over a period is used. Estimated values are calculated from measured velocities and numerical time derivatives.

The ratios in figure 4.9 are in general larger than unity. This means that the discrepancy between model and experiment cannot be explained by measurement errors, so refinement of the model is justified.

4.2.2 KC dependent coefficients

The force on a cylinder oscillating in 2-D cross flow is known to be highly dependent of the KC number for the range of amplitudes discussed here. The main reason is that vortices shed in one half cycle influences the inflow of the cylinder in the next half cycle (Faltinsen 1990). But as shown in chapter 2 this dependence almost disappeared for an inclined cylinder, so the modification of the inflow seems to be less influential when axial flow is present. The current

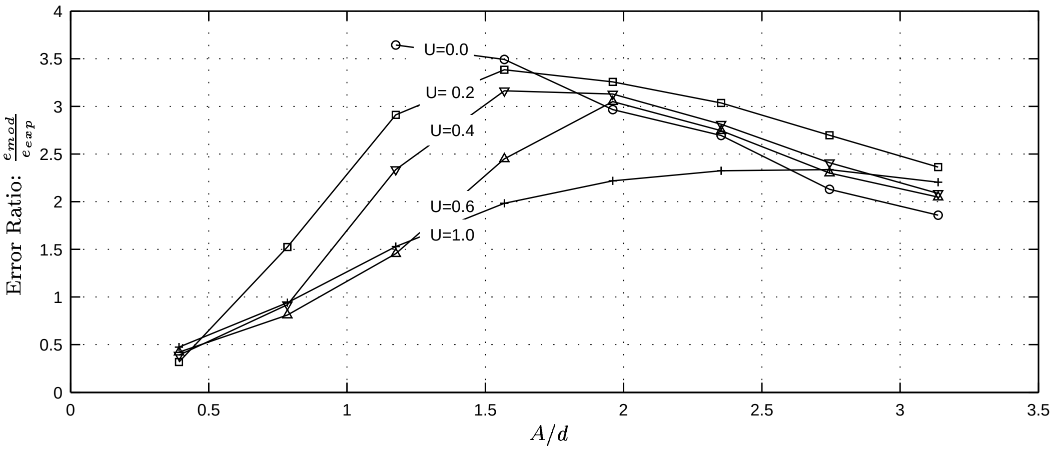

Figure 4.9: *Force model error* e_{mod} *over measurement error* e_{exp}*: Constant coefficient. A ratio of unity means that the numerical model is as good as the uncertainty in the experiments. Indicated tow speeds* U *in* ms^{-1}*.*

case has steady flow in the axial direction and oscillating flow in the transverse direction. Then vortices shed at one section is convected downstream during a half cycle and influence the inflow for some downstream section. The distance between where the vortex is shed and where it returns to the cylinder depends on both oscillation period and tow speed. As mentioned above, for the highest tow speed they do not return at all, which of course is a significant difference from the 2-D assumption.

The values of the coefficient in figures 4.10 - 4.11 are found by a least square curve fit of the measured data to the equation

$$F_z = a_1 \frac{\mathrm{d}w}{\mathrm{d}t} + a_2 w \left| w \right| \tag{4.11}$$

where w is the measured vertical velocity. The coefficients are then:

$$C_a = \frac{a_1}{\rho \pi \frac{d^2}{4}} \tag{4.12}$$

$$C_d = \frac{a_2}{\frac{1}{2} \rho d} \tag{4.13}$$

where F_z is the measured force per unit length of the cylinder. The calculation was done on each measured period, and the values in figures 4.10 - 4.11 represent the mean of at least six estimates. The standard deviation of the estimates are given in figure 4.12. This way of estimating the coefficient is assumed to be the most accurate of the methods listed by e.g Chakrabarti (1987). The alternative of estimating the coefficients at zero and max velocity gave the same general trend, but with larger errors.

The KC numbers are calculated from the measured velocity and period:

$$KC = \frac{V_{n0}\, T}{d} \tag{4.14}$$

Since the motion is not exactly harmonic in all cases, this is not exactly the same as $KC = 2\pi\frac{A}{d}$. For this reason there is some variation of the tested KC numbers between the tow speeds, even if the tested position amplitudes were the same.

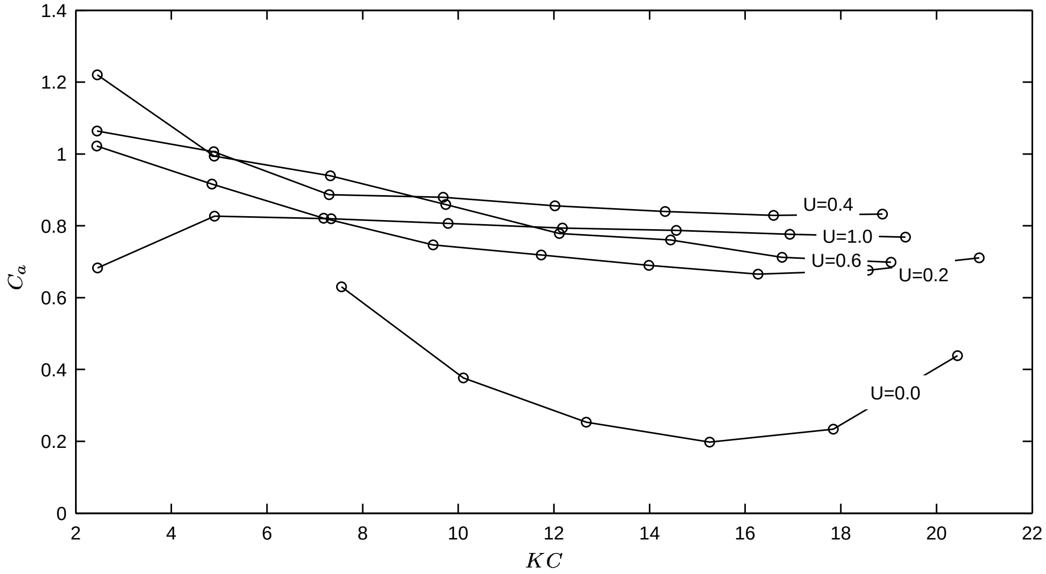

Figure 4.10: *Cross flow added mass coefficient with axial velocity estimated from experiments Tow speed U in ms^{-1}.*

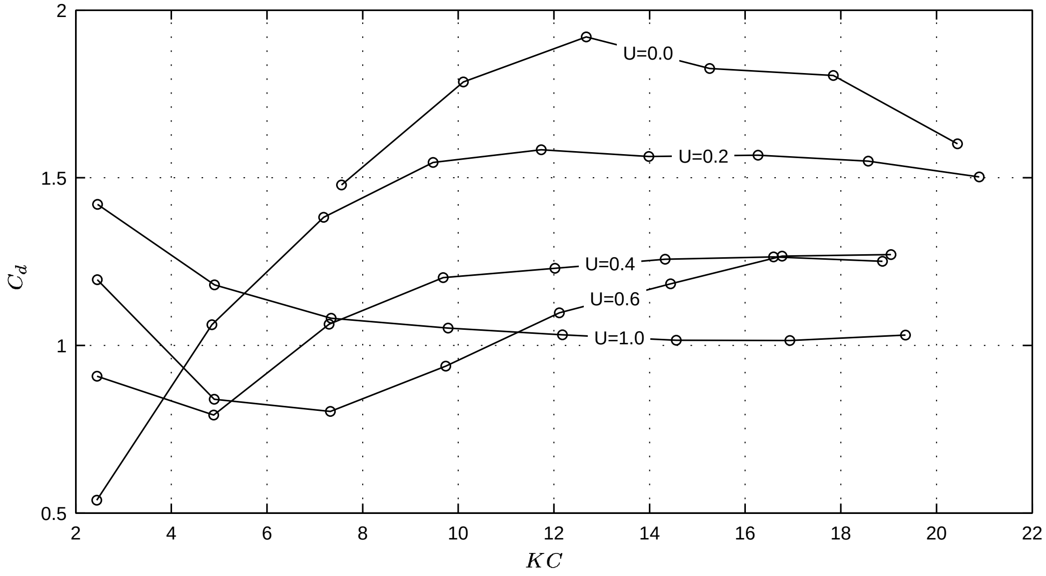

Figure 4.11: *Cross flow drag coefficient with axial velocity estimated from experiments Tow speed U in ms^{-1}.*

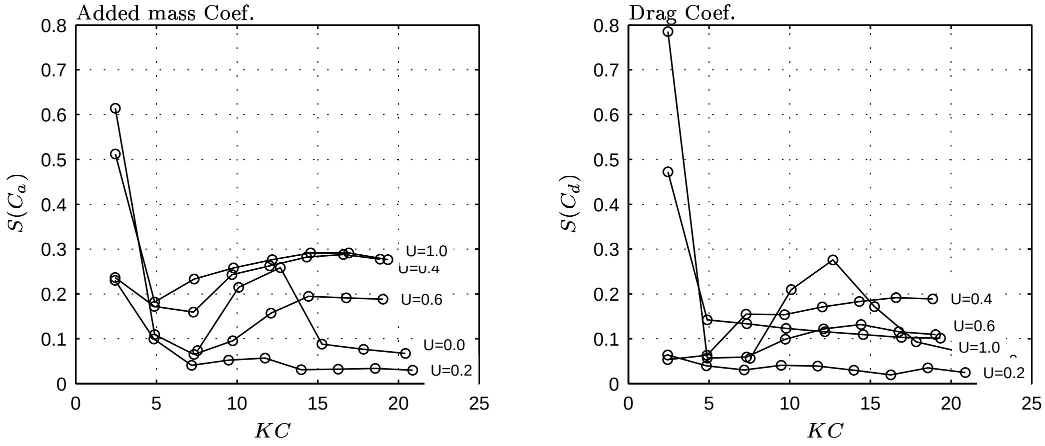

Figure 4.12: *Period to period variation of coefficient estimates. The vertical axis is the the standard deviation of the calculated values. Tow speed* U *in* ms^{-1}.

The results for the added mass coefficient show the same tendency as for the inclined cylinder results in chapter 2. In the presence of an axial flow component the added mass coefficient is only a weak function of the KC number. The variation due to non zero speed in figure 4.10 is within the period to period variation of the estimates (figure 4.12, and may therefore be somewhat arbitrary. The value does seem to converge to $C_a = 0.8$ as KC increases. From the result for the inclined cylinder, this may rise to unity for $KC \geq 50$.

As for the inclined cylinder, the distinctive maximum for the drag coefficient found for $10 < KC < 15$ disappears in the presence of axial flow, but this seems to be the only similarity between the two cases. For the current case, the drag coefficient converges to different values based on the tow speed. For $U = 0.2$ ms^{-1} there probably still is some KC number dependence, for $U = 0.4$ ms^{-1} and $U = 0.6$ ms^{-1} the drag coefficient converges toward $C_d \simeq 1.2$, the expected value for subcritical flow. For $U = 1.0$ ms^{-1} the KC dependence is weak, and the C_d value less than for true subcritical flow. As discussed above, this most likely is a result of the length the cylinder travels during a half period of oscillation and a possible transition to turbulent boundary layer and thus transcritical flow.

The result of using coefficients from figure 4.10 and figure 4.11 to model the measured force is investigated in figure 4.13, by the same ratio as in figure 4.9. The uncertainty in the coefficients indicated by figure 4.12 is not included here, only the difference between measured and calculated force is included in the model error. From the figure it seems that the results are acceptable for all cases. It is clearly an improvement over the result with constant coefficients in figure 4.9.

4.2.3 Linear model

In literature on towed arrays, the normal hydrodynamic force is assumed proportional to the normal component of the velocity (Paidoussis, Grinevich, Adamovic, and Semler 2002; Dowling

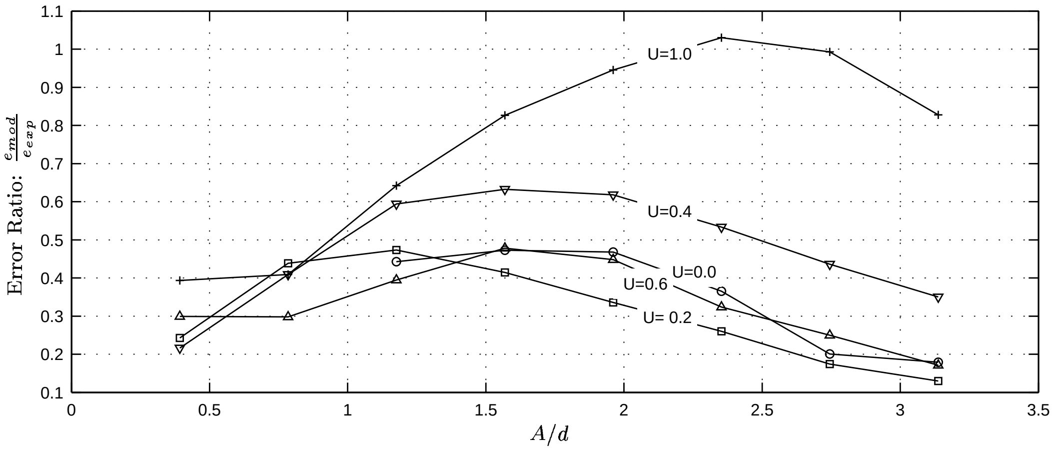

Figure 4.13: *Force model error e_{mod} over measurement error e_{exp}: KC dependent coefficients. A ratio of unity means that the numerical model is as good as the uncertainty in the experiments. Indicated tow speeds U in ms^{-1}.*

1988; Kennedy 1987). If the angle of attack α is small, it can be assumed that

$$w^2 \simeq 0 \tag{4.15}$$

$$\sin(\alpha) \simeq \alpha = \frac{w}{u} \tag{4.16}$$

Then keeping first order terms only, equation (4.4) can be written

$$F_{nv} = -C_{n1}\frac{1}{2}\rho wu\ d \tag{4.17}$$

Setting $C_a = 1$ and $C_{n1} = 0.08$ gives the error ratios in figure 4.14. This is found to be the best value for $U = 1.0$ ms^{-1} while for lower speed the model does not make much sense. Zero tow velocity is not included, since this would give zero viscous force. Comparing to the amplitude of α in figure 4.1, $U = 1.0$ ms^{-1} is the case where the low angle assumption could be expected to hold. For this tow speed the linear model seems to perform better than the Morison's equation.

The value of $C_{n1} = 0.08$ is quite high. The expected value taken from e.g Dowling (1988) is $C_{n1} \leq \pi C_f$, a result based on unseperated flow. In Kennedy (1987) it is given as $C_{n1} = 0.06$, unfortunately without much explanation. It is also the same result as found for small stationary angles when rotating in yaw, still without any explanation.

4.2.4 Time series comparison

From figures 4.9 - 4.14 is seems that for low amplitudes all models are acceptable. This is because the relative error for these cases are high, from figure 4.2 and figure 4.3 they are of the order 50-100%. It must therefore be concluded that the quality of the data for these cases is not good enough to properly compare the models.

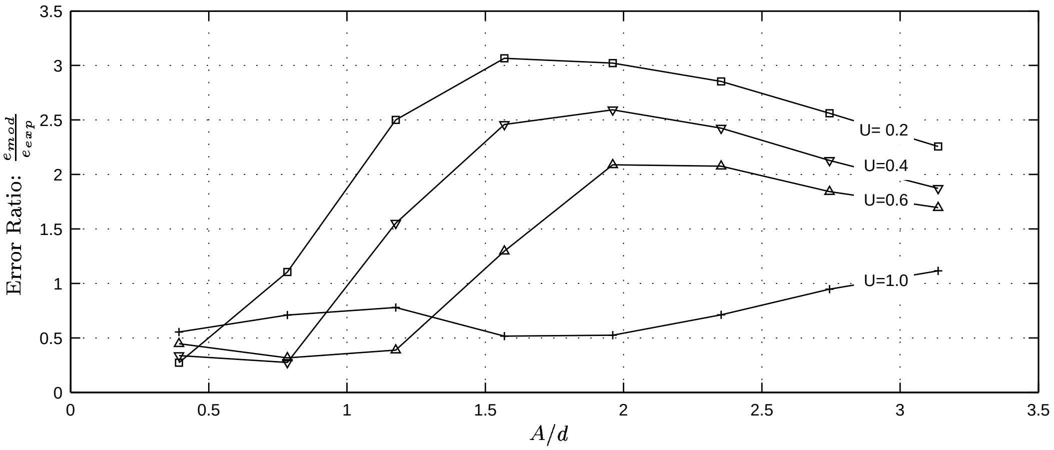

Figure 4.14: *Peak Force estimate error e_{mod} over measurement error e_{exp}: Linear Model. A ratio of unity means that the numerical model is as good as the uncertainty in the experiments. Indicated tow speeds U in ms^{-1} .*

The time series of selected cases are shown in figure 4.15 and figure 4.16. As before, the time series shown are the average of all steady state periods between identified zero up crossing points. The bars indicate the 95% confidence interval of the peak values.

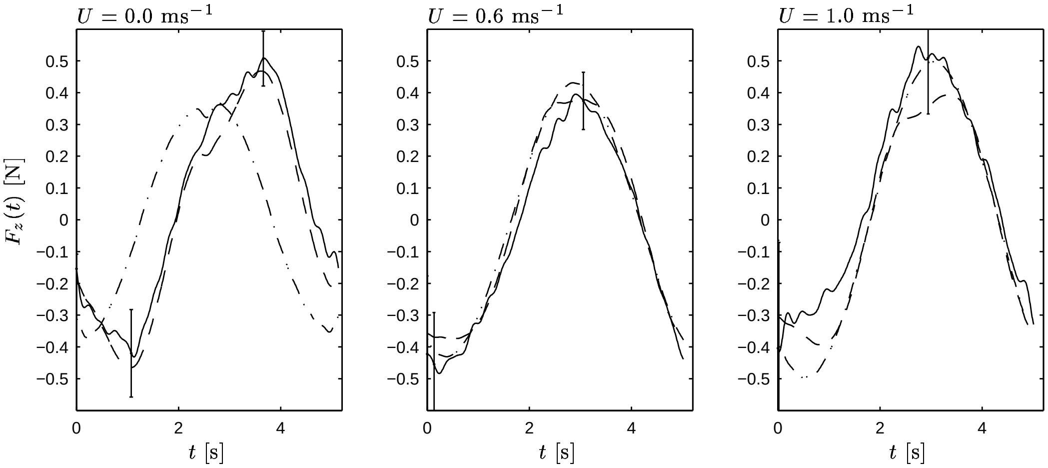

Figure 4.15: *Time series at $A/d = 1.17$: — Measured; -- Non linear model; -·- Linear model. Bars indicates 95% confidence interval of averaged values.*

Forces calculated by the nonlinear expression in equation (4.4) with KC dependent coefficients and forces calculated by the linear model in equation (4.17) are included in the plots. For $U = 0.0$ ms^{-1} the viscous part of the force becomes zero for the linear model, so the plotted force is here the estimated inertia force. There is a dip in the curves at $t \simeq 2.5$ s, the point where the motion changes direction. This is due to the particulars of the motion control system. The force estimated by the non linear model follows the measured force quite well for the low

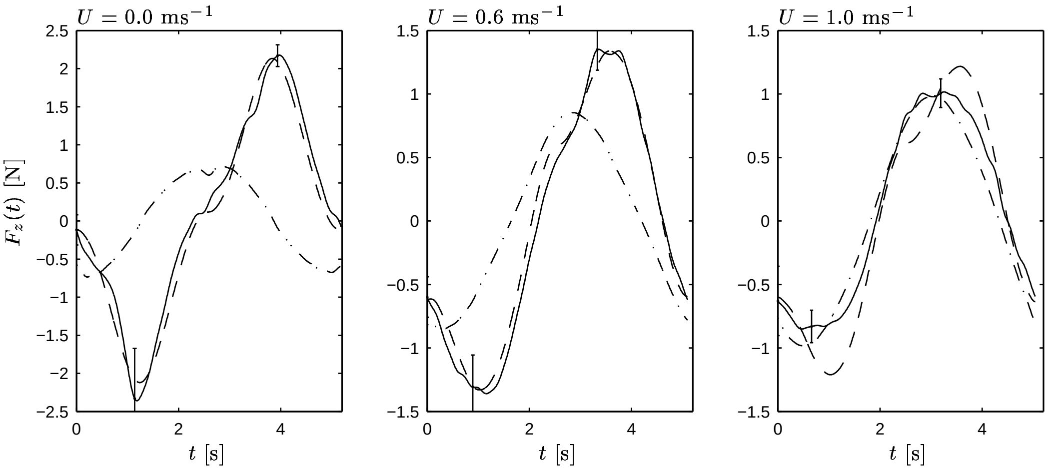

Figure 4.16: *Time series at $A/d = 2.34$: — Measured; -- Non linear model; -·- Linear model. Bars indicates 95% confidence interval of averaged values.*

velocities, with a small deviation in the phasing of inertia and drag forces known from 2-D tests (Sarpkaya and Isaacson 1981). For $U = 1.0$ ms^{-1} the linear model works quite well, and better than the non linear version. This is particularly true for the upper part of the curve, while the lower part of the measured signal is more flat than expected. This could be the result of the wake of the struts and is included in the error estimate for the peaks.

4.3 Conclusions: Rigid Cylinder

Before continuing with a flexible cylinder, the following observations is done from the rigid cylinder results.

- For low angles of attack the normal forces depends very much on the initial vortex formation. If this is symmetric, the 2D+t principle seems to give a reasonable description of the force. If asymmetric, there seems to be a large term which is linear with the angle of attack.
- Even when the cross flow principle holds, the appropriate drag coefficient depends on the Reynolds number of the longitudinal flow
- In the case of the oscillating flow, the initial vortices are normally asymmetric and with increasing speed, the linear drag term becomes important.
- The importance of the KC number decreases when the axial flow component increases. This is particularly true for the added mass coefficient.

Chapter 5

Oscillating Flexible Cylinder

This chapter describes the experiment with forced oscillation of a towed flexible cylinder. The experiment was carried out in towing tank I+III (see appendix A) in November 2001. This means that they are performed before the rigid body experiments. The results presented here deviated so much from the expected theoretical results that further investigation with the rigid cylinder were initiated.

5.1 Set up and Procedure

For practical reasons similarity in geometry and Reynolds numbers to a full scale streamer are hard to obtain. In this case it was assumed that a length to diameter ratio above 1×10^3 and a Reynolds number based on length above 1×10^6 would be sufficient to capture the physics of the full scale case. The limiting Reynolds number was taken from White (1972), and represents the lower limit for his approximate formula for drag coefficient for steady axi-symmetric boundary layers, see chapter 2. For the lowest tow speed this Reynolds number was achieved after about 2 m, or about 15% of the total length. The forward connection assembly of the streamer model was not entirely smooth, and also considering that oscillation creates pressure gradients in the transverse direction, it is possible that transition took place even earlier. The limit on length to diameter ratio is of the same order order as a typical section of a streamer between two birds. The Reynolds number based on radius ranged from $R_a = 2.75 \times 10^3$ to $R_a = 13.75 \times 10^3$, which is about 10% of typical values for the full scale streamers. According to the curves for axi-symmetric boundary layers in chapter 2, the friction coefficient is then higher in the experiment than in full scale.

Figure 5.1 illustrates the experimental set up. The upstream support provided a forced, harmonic oscillation, while the downstream end was supported by springs in transverse directions. The spring condition may be looked upon as a simplification of either a proportional controller or the towing line of a tail buoy. The forward and aft end of the cable were placed 0.43 m below the surface, giving a depth to diameter ratio of 39. This was assumed to be

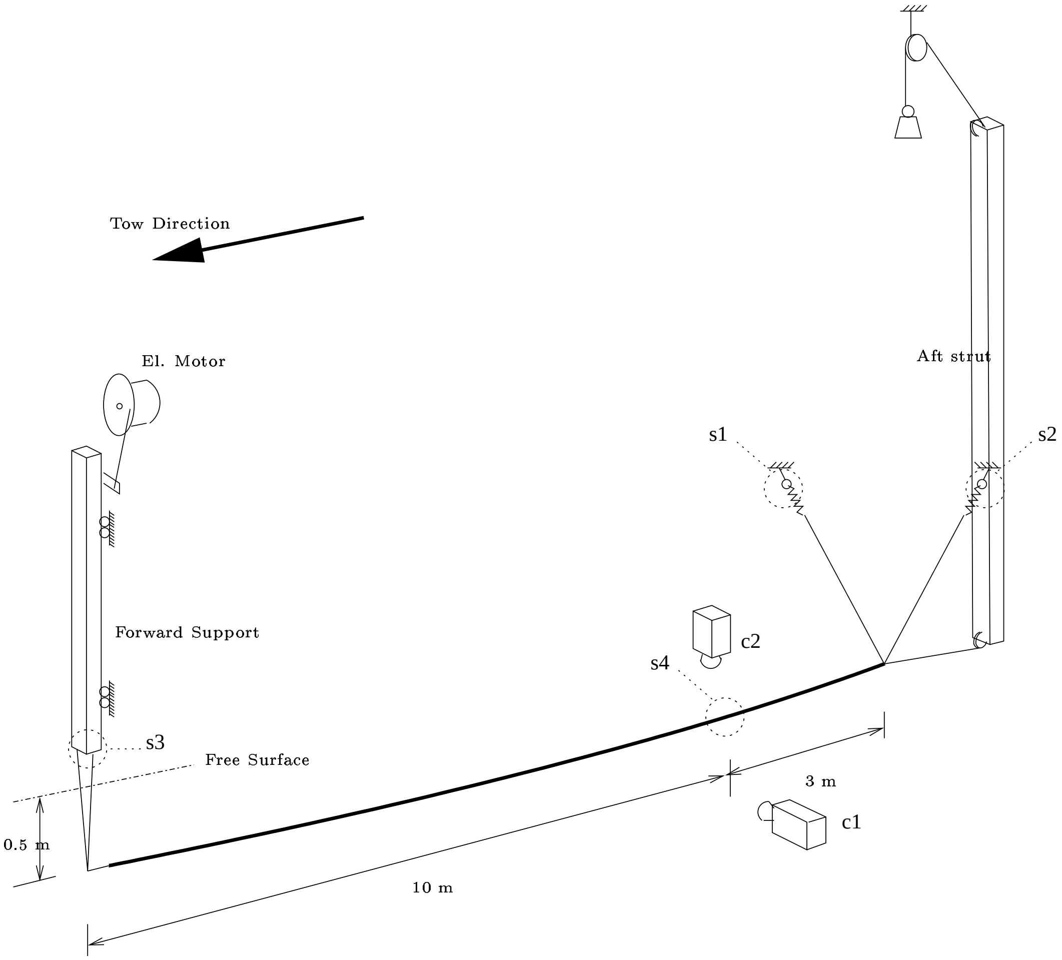

Figure 5.1: *Experimental set up for measuring response of a flexible cylinder. The shown assembly was mounted on the towing carriage in the large towing tank at NTNU/MARINTEK.*

sufficient for avoiding any effects on the cable from the free surface, see the discussion of error sources for the oscillating rigid cylinder.

Table 5.1: *Parameters for the cable used in experiments.*

Tow speed:	$U =$	0.5-2.5 ms^{-1}
Diameter:	$d =$	0.011 m
Length to diameter ratio	$\frac{L}{d} =$	1180
Reynolds numbers	Re_L	0.65-3.25 $\times 10^7$
Distributed structural mass:	$q =$	97.5 $\times 10^{-3}$ kgm^{-1}
Aft tension:	$T_0 =$	19.6 N
Aft spring stiffness	$k_p =$	48.2 Nm^{-1}
Period of oscillation	$T_p =$	0.3-30 s
Amplitude of oscillation:	$A_0 =$	0.05 m

Main parameters for the experiment are listed in table 5.1. The upstream end of the cable was connected to a foil shaped strut, minimizing the disturbance to the incoming flow. The strut was mounted on a force sensor (s3 in figure 5.1) measuring forces in all three directions. This in turn was mounted on beam moving on a rail allowing motion in the vertical direction. A linkage with pinned ends connected the beam to a disk driven by an electrical motor. The frequency of the forced motion was controlled by the rpm of the motor, while the amplitude was controlled by the distance from the center of the disk to the linkage connection point. A position sensor was used to register the actual vertical motion of the strut.

The downstream end of the cable was held by an assembly of two thin wires connected to springs and force sensors (s1 and s2 in figure 5.1). The V formed by these wires allowed measurement of position in both vertical and horizontal direction, assuming linear relations between extension and force in the springs. This was assured by using long and pretensioned springs. The extension of the cable was guided by pulleys through a vertical pipe and tension was applied by a known weight.

All force sensors were standard sensors used by MARINTEK. The downstream position measuring system comprising wires, springs and the force sensors s1 and s2 in figure 5.1 was calibrated as a whole before and after the experiments. The tow point force sensor was calibrated before the experiment and the factors were found to be in accordance with the data sheet for this sensor.

In addition to the force sensors two accelerometers were placed inside the cable 10 m downstream of the tow point (denoted s4 in figure 5.1). The choice of this location was somewhat arbitrary and mainly based upon practical considerations. Two underwater cameras were pointed at the same location, one on the left side looking forward, the other directly above the cable. The cameras are denoted c1 and c2 respectively in figure 5.1. Unfortunately the signals from the accelerometers gave very little useful information. The reason for this is unclear, but it might be the result of water penetration causing an earth fault in the sensors. The presented results for this location are therefore the result of a digital image processing of the video signals.

The data were recorded by the standard data acquisition system on the carriage. The sample frequency was set to 60 Hz and an analog filter with cut-off frequency of 20 Hz was used before analog to digital conversion of the data. The data were analyzed and plotted on a PC.

The cable was made of a Tygon tube, a commercially available flexible tubing. Delivered in a roll, the tubing has a tendency to keep this shape. To minimize this, the tubing was filled with water and placed under tension for a week. In addition some tension was applied in the tubing during the experiment. Dacron fibers were placed inside the flexible tubing in order to avoid any extension of the cable. The forward part of the cable was 10 m long and filled with a mixture of 15% (volume) water and 85% alcohol providing a negative bouyancy of 0.024 N, or 3 % of the weight. Spacers were placed at 1 meter intervals in order to keep the position between the fibers and the tubing. The aft part of the cable was 3 m long, and in addition to the fibers also the signal cables for the accelerometers were led through this part. Small cylinders of foam, about 25 mm long, were glued to the fiber with about 10 mm between them in order to provide the necessary buoyancy. The tubing was filled with water, making sure that no pockets of air were trapped inside. When control weighing the assembled cable in water after the test were ran, the aft part were found to be slightly positively buoyant. This indicates that some air may have been trapped after all. The result is that the cable had a slightly different shape than intended.

The roughness of the tubing surface was not measured, but it is assumed to be very smooth. According to equation (2.6) the admissible roughness height for assuming a smooth surface is:

$$k_{adm} \leq 100\frac{\nu}{U} = 4 \times 10^{-5} \text{ m} \tag{5.1}$$

for the highest tow velocity. It is most likely that this kind of roughness would have been discovered by inspection of the tube.

Figure 5.2 shows the coordinate system used for the results. Origin is in the tow point, and the positive y-axis is in to the paper plane.

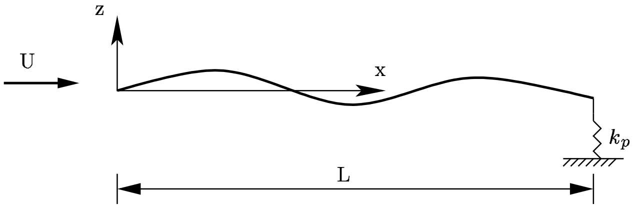

Figure 5.2: *Reference system for the flexible cylinder.*

5.2 Tow Point Forces

The main purpose of the force measurement was to establish the force coefficient in the tangential direction. It is assumed that this is given by the skin friction only, so an averaged skin friction coefficient is calculated from the measurements. Since the linearized model of a towed cable assumes time invariant tension, the time variation of the tow point tension is also of interest.

5.2.1 Measured friction coefficient

The reduction equation for the averaged friction coefficient C_F is

$$C_F = \frac{F_x}{\frac{1}{2}\rho\pi dLU^2} \tag{5.2}$$

Here F_x is the time average of the $x-$direction force in the tow point, corrected for drag from the foil strut (measured) and the aft appendage drag (estimated), see figure 5.3. The two dimensional drag coefficients for the wires in the aft support are taken from Blevins (1992) for appropriate Reynolds numbers.

The procedure for estimating the measurement errors is given in chapter 2, and applied for a similar problem in chapter 3. The tow force is the mean of all runs on a given velocity, giving a second order replication level. The variation of force with oscillation frequency were found to be quite small for the two highest tow speeds and is included in the precision error. Bias errors for the tow point forces are

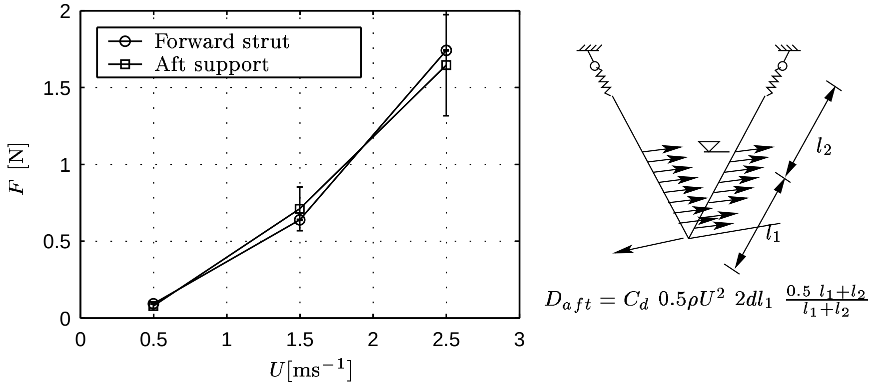

Figure 5.3: *Correction on tow force due to fore and aft support, bars represents 95% confidence interval. Estimation of drag on aft support is indicated in the right figure, the lengths are* $l_1 = 534$ *mm and* $l_2 = 465$ *mm. Diameter for the wires are 0.6 mm and drag coefficients per unit length are* $C_d = 1.2,\ 1.2$ *and* 1.0 *for the three velocities respectively.*

Forward Strut (B_{01}) Drag force on the forward strut were measured by separate runs. For the x-direction the bias error is assumed to correspond to the precision error of these measurements. The value is quite constant and equal to $B_{01} = 0.004$ N.

Aft support (B_{02}) The drag of the aft support is estimated from drag forces in the thin wires supporting the aft end. The assumed error of this calculation is set to 20% of the estimated value.

$$B_{02} = 0.2\ D_{aft} \tag{5.3}$$

Here D_{aft} is the estimated drag of the aft support,see figure 5.3.

Sensor Calibration (B_{03}) The force sensors are of standard MARINTEK design. The uncertainty of calibration is given to $B_{03} = 0.01F_0$, where F_0 is the measured force.

The sensor is exposed to the free stream airflow when traveling forward. This might cool the sensor and result in drift. The time series were inspected for drift but no such trends could be detected. The mean values are based on a full number of periods, and no filtering is done. The error due to signal processing is therefore neglected.

The uncertainty of the dynamic pressure was discussed in chapter 3. The precision error includes velocity measurements only. The flow due to generated waves are neglected, since the diameter to depth ratio of the cylinder this time is 0.026. The residual flow is calculated the same way as in chapter 3 and the result is given in table 5.2. The waiting time between runs was at least 4 minutes. The drag coefficient for the test cylinder is a representative estimate for the friction coefficient at high speeds. But the main contribution to the wake is from the aft strut indicated in figure 5.1 which is a rectangular hollow section with no streamlining. The drag coefficient is taken from Blevins (1992) for a square two-dimensional rectangle. The error is given by the result for the aft strut: $B_{04} = 0.06$ ms^{-1}. The uncertainty in the density is again $B_{05} = 0.1$ Kgm^{-3}.

The alignment was done by a meter stick with fixed points at the carriage and the water surface as references. The uncertainty should be within $\delta = 10$ mm, giving an angle maximum

Table 5.2: *Estimated Residual velocity u_1 after 4 minutes*

	C_D	d/A	$\frac{u_1}{U}$
Test Cylinder	0.0035	$\pi dl = 0.45\ m^2$	0.002
Aft Strut	2.2	0.05 m	0.06

angle of arctan $\left(\frac{\delta}{L}\right) = 0.044°$.

Both length and diameter of the model cable will vary due to the flexibility of the cable and production errors. The Dacron filaments were made slightly longer than the tubing, giving some tension in the outer wall. This was mostly done to counteract the tendency of the tubing to roll up on itself. The result is some uncertainty, particularly in the diameter. Testing gave a change in diameter of less than 0.5 mm for the relevant tension. Assuming the production error is of the same magnitude (no specification of this was available from the vendor) gives $B_{06} = 0.5$ mm. The stretching of the cable were found to be less than $B_{07} = 0.02$ m, taken from video recordings of the experiment.

The sensitivity coefficients for these parameters are:

$$\kappa_{01-03} = \frac{\partial}{\partial F_x}\left(\frac{F_x}{\frac{1}{2}\rho U^2\ dL}\right) = \frac{1}{\frac{1}{2}\rho U^2\ dL} \tag{5.4}$$

$$\kappa_{04} = \frac{\partial}{\partial U}\left(\frac{F_x}{\frac{1}{2}\rho U^2\ dL}\right) = -2\frac{F_x}{\frac{1}{2}\rho U^3\ dL} \tag{5.5}$$

$$\kappa_{05} = \frac{\partial}{\partial \rho}\left(\frac{F_x}{\frac{1}{2}\rho U^2\ dL}\right) = -\frac{F_x}{\frac{1}{2}\rho^2 U^2\ dL} \tag{5.6}$$

$$\kappa_{06} = \frac{\partial}{\partial d}\left(\frac{F_x}{\frac{1}{2}\rho U^2\ dL}\right) = -\frac{F_x}{\frac{1}{2}\rho U^2\ d^2 L} \tag{5.7}$$

$$\kappa_{07} = \frac{\partial}{\partial L}\left(\frac{F_x}{\frac{1}{2}\rho U^2\ dL}\right) = -\frac{F_x}{\frac{1}{2}\rho U^2\ dL^2} \tag{5.8}$$

The propagated error is then calculated as in chapter 2. The measured coefficient and the errors are listed in table 5.3. These numbers are based on the forced motion test, so the errors covers all variation due to oscillation of the streamer. This is the main error source, almost 30% for the lowest tow speed.

Table 5.3: *Measured Friction Coefficient. The error e represents the 95% confidence interval.*

U [ms^{-1}]	C_f	e
0.5	4.7×10^{-3}	1.6×10^{-3}
1.5	3.0×10^{-3}	0.4×10^{-3}
2.5	2.5×10^{-3}	0.3×10^{-3}

5.2.2 Models for the friction coefficient

In principle the friction coefficient is a function of the local Reynolds number, and therefore a function of the position along the cable. Possible expressions for this local coefficient are:

$$C_f(x) = 0.0015 + \left(0.20 + 0.016\left(\frac{2x}{d}\right)^{0.4}\right) Re_x^{-\frac{1}{3}} \tag{5.9}$$

$$C_f(x) = 0.0123 Re_x^{-0.08} \tag{5.10}$$

$$C_f(x) = 0.027 Re_x^{-\frac{1}{7}} \tag{5.11}$$

The first of these is a simplified formula suggested by White (1972) based on analysis of the axi-symmetric boundary layer on a smooth cylinder, see chapter 2. The second is a curve fit of velocity measurements in the axi-symmetric boundary done by Lueptow and Haritonidis (1987). The last expression is the expression for a smooth, flat plate. The averaged coefficients are found by integrating these expressions over the length of the cable and divide by the length:

$$C_F = 0.0015 + \left(0.30 + 0.015\left(\frac{2L}{d}\right)^{0.4}\right) Re_L^{-\frac{1}{3}} \tag{5.12}$$

$$C_F = 0.0134 Re_L^{-0.08} \tag{5.13}$$

$$C_F = 0.032 Re_L^{-\frac{1}{7}} \tag{5.14}$$

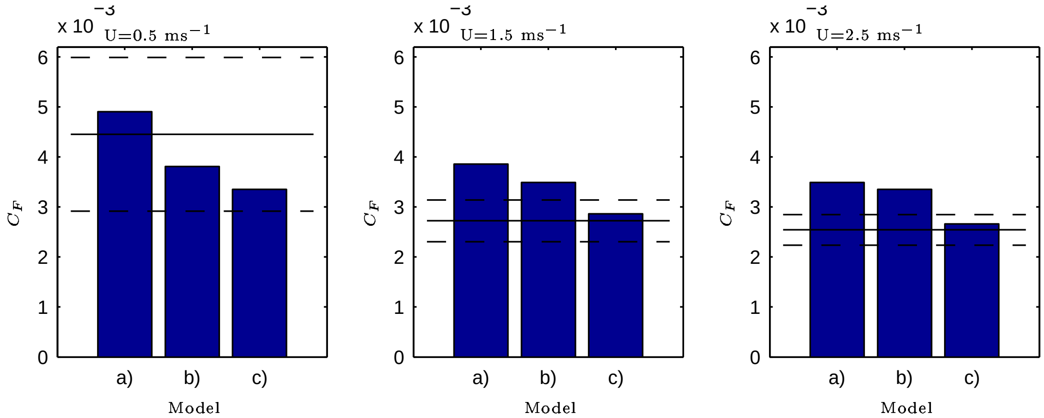

Figure 5.4: *Estimated friction coefficient. C_F: a) equation (5.12); b) equation (5.13); c) equation (5.14); —measurement; - -95% confidence interval of measurement.*

The results are compared to the measured values in figure 5.4 where the models are represented by bars and the measurements from table 5.3 are represented by lines. For low speed all models are within the confidence interval, which should be expected considering the high measurement error for this case. For the lowest speed the models based on a axi-symmetric boundary layer are closest to the measured mean, while for higher speed the equation for a flat plate seems to be the best estimate, and the assumption of a thick axi-symmetric boundary layer also for the oscillating cable seems questionable.

In the description of the set up of the experiment is was mentioned that the boundary layer might be laminar for parts of the model streamer. Since all models assumes a turbulent boundary layer they might overestimate the measured result. But this should be most profound at the lowest tow speed, and cannot explain the large over prediction of model *a*) and *b*) at the higher tow speed.

For the comparison of model and experiment in the next chapters, the measured friction coefficient will be used. For other cases, equation (5.14) will be used, given that Reynolds number based on radius is above $R_a = 1 \times 10^4$.

5.2.3 Dynamic Tension

The importance of the dynamic part of the tension is shown in figure 5.5. Here the Root Mean Square (RMS) values of tension in the tow force is plotted as ratio of the average tow force (the measured force in tow direction). The tension is calculated in equation (5.15)

$$T = \sqrt{F_x^2 + F_y^2 + F_z^2} \tag{5.15}$$

where F is the measured force in the indicated direction. The vertical force F_z is corrected for the inertia force of the forward strut.

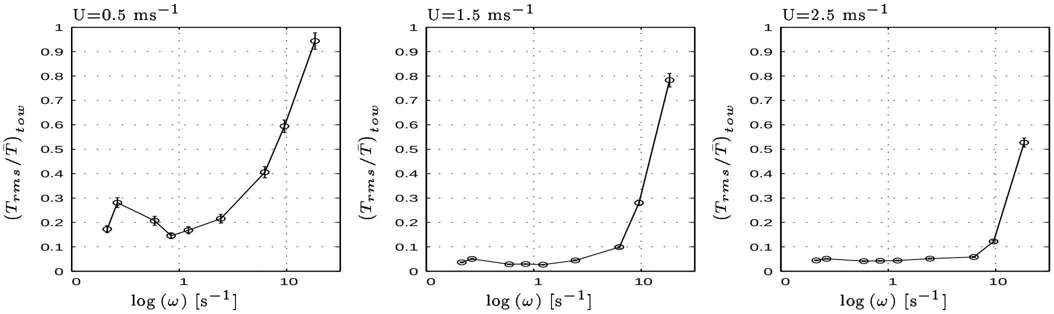

Figure 5.5: *Tow point tension: RMS to mean ratio.*

The dynamic part of the tension is below 10% of the mean for most cases, except at the lowest velocity and the highest frequencies. For all velocities the inertia forces for a harmonic motion increases with the square of the frequency, as do the hydrodynamic forces since they normally are proportional to the velocity squared. The rapid increase for high frequencies are therefore to be expected. The dynamic part of the tension does not necessarily have the same dependency on tow velocity as the tow force, so some variation with tow speed is to be expected.

5.3 Dynamic Response at x/L=0.77

The dynamic response of the cable was found at $x/L = 0.77$ by analyzing the video images of the cable. In this process each digital video frame were saved as a gray scale still image. In digital form such an image is a matrix containing the intensities in each pixel of the image. Since the camera stands still relative to the transverse motion this matrix represent a grid in which the cable moves. Such a frame is shown in the left part of figure 5.6. The image from the two cameras were mixed together when recording. The upper part is cable seen from above (Camera 'c2' in figure 5.1) and the lower part is the view from the side ('c1' in figure 5.1). The right part show the intensity along the white lines in the image. In this analysis the peak of these curves are assumed to give the current position of the cable. By relating the number of pixels along the lines and known dimension in the image, here the diameters, the motion of the cable could be traced.

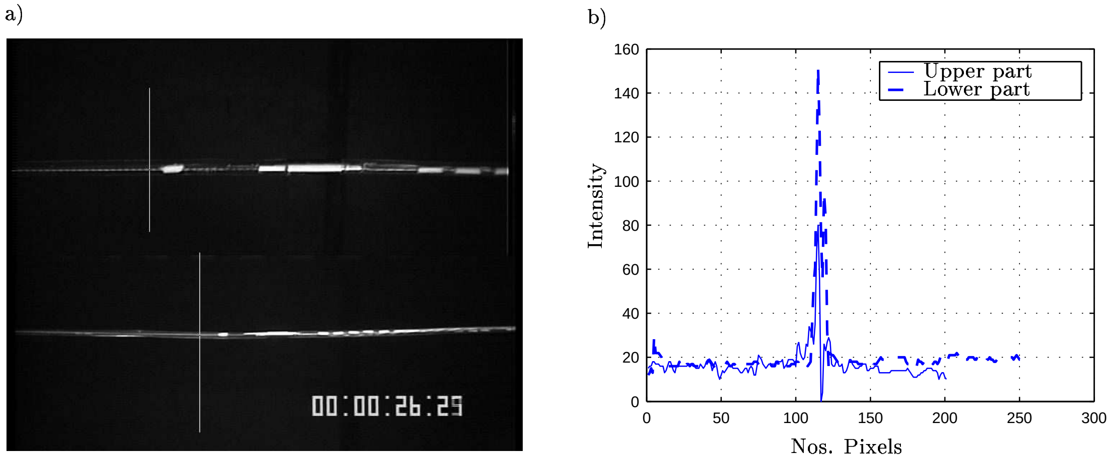

Figure 5.6: *Video Tracking: a) single frame of video recording, b) Intensity along lines indicated in the image.*

The reduction equation is here

$$Y = k\ X \tag{5.16}$$

where Y is the response, k relates position in pixels to e.g position in meters and X is the result (in pixels) from the image analysis. The 0'th order replication errors are summarized in table 5.4:

Resolution The video image has a resolution of 576 × 720 pixels and are recorded with 25 frames per. second. The resolution error is then $B_{01} = 0.5\ k$.

Scale The scale factor is found from the image, as

$$k = \frac{d}{X_d} \tag{5.17}$$

where X_d is the number of pixels to cover the cable diameter d. With the ranges as indicated in figure 5.6 the size of a pixel (k) is 0.5 mm and 1.1 mm for y- direction and z -direction respectively The resolution error gives a scale error of:

$$B_{02} = \frac{\partial k}{\partial X_d}\ \Delta X = -\frac{d}{X_d^2}\ S_{i01} \tag{5.18}$$

Perspective The method described above assumes that the distance from the camera to the cable is constant. Particularly for vertical camera, where the distance is small and motion of the cable large (relatively, that is) the effect of perspective on the scaling may be significant. The error is given by:

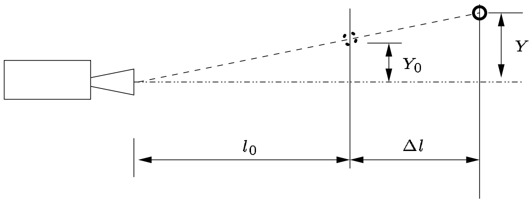

$$\begin{aligned} \frac{Y_0}{l_0} &= \frac{Y}{l_0 + \Delta l} \\ &\Downarrow \\ Y &= Y_0 \left(1 + \frac{\Delta l}{l_0}\right) \end{aligned}$$

thus $B_{03} = \frac{\Delta l}{l_0} X_0$. Here X_0 is the measured position, l_0 is the nominal distance between camera and cable, and Δl is taken from the amplitudes of the oscillations in the 'other direction' in figure 5.9 and figure 5.8.

Camera motion The method requires that the cameras are not moving, or that other optic effects disturbs the images. Since no motion or disturbance have been observed in the videos, these effects are neglected.

Data Analysis Instead of a low pass filter, a running average procedure was used in the data analysis. Figure 5.7 show the effect of varying the number of points in the averaging. The number of points is a trade off between avoiding noise and keeping the dynamics. Visual inspection of the time series indicated that 5 points on each side seemed reasonable. The numbers in the table is the standard deviation for points corresponding to $n = 4$ and $n = 6$ in figure 5.7.

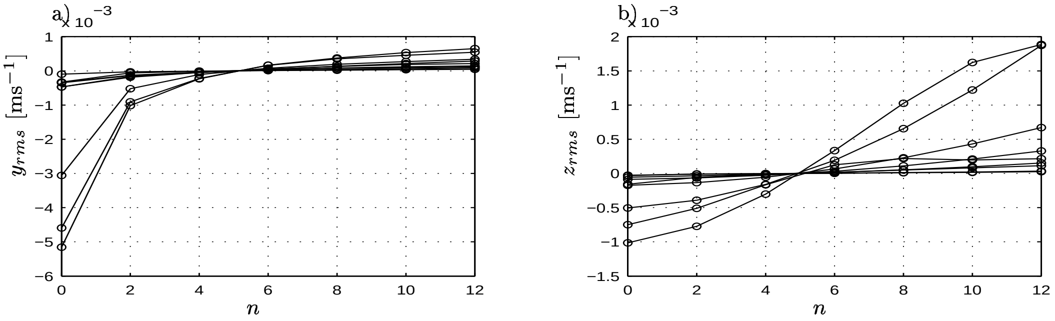

Figure 5.7: *Effect of Averaging on amplitude. Each point in the time series for $U = 2.5$ ms^{-1} are averaged based on n points on each side, and the resulting peak to peak amplitude values are compared to a reference value of $n = 5$. a) y -direction, b) z direction*

For the two or three lowest frequencies and tow speeds $U = 1.5$ ms^{-1} and $U = 2.5$ ms^{-1} the time series contains three or less complete oscillations. For these cases the 0'th replication level error estimates has to be used. For higher frequencies, the peak to peak amplitude is calculated for each complete oscillation (of the tow point). The deviation of these amplitudes are then used to calculate a precision error. The 0'th level errors are included as a bias error in these cases, giving a quite conservative error estimate. The image tracking procedure may

Table 5.4: *Elemental errors for video tracking of response at* $x/L = 0.77$

i	Source	S_i $y-direction$	S_i $z-direction$	κ_i
01	Resolution (measurement)	0.5 [pixel]	0.5 [pixel]	k
02	Resolution (scale factor)	1.1×10^{-5} [m/pixel]	5.5×10^{-5} [m/pixel]	X_0
03	Perspective	0.037 z_0 [m]	0.0055 y_0 [m]	1
04	Data Analysis	1.05×10^{-4} [m]	1.37×10^{-4} [m]	1

miss the cable for some images, which leads to large and faulty peaks in the time series. To remove such peaks from the results, the Chauvenet criterion for rejecting outliers were applied, see chapter 2.

5.3.1 Amplitude of motion

A inspection of time series of the forced motion at the tow point revealed that the input was not quite the pure sine signal aimed for. This was mainly due to the difference in motor load when lifting the front support from the downward part of the cycle. The response were therefore not pure sine functions either, and the peak to peak amplitudes are presented rather than oscillation amplitudes. Power density spectra of the time series confirms that the response is one the same frequency as the input. The exception is the highest frequencies, where no distinct peak could be detected in the spectra.

The mean peak to peak amplitudes for all time series are plotted in figure 5.8 and figure 5.9. See appendix B for tabulated results. The argument axis is the base 10 logarithm of the forced circular frequency, $\omega = 2\pi f$, where f is the frequency in Hz.

The trend for the in-line response is a small peak at $\omega \simeq 1$ rads^{-1} for all velocities. Unfortunately data was not obtained for low frequency for $U = 0.0$ ms^{-1}, so it is unknown if this peak were present in this case also. For frequencies above this peak the amplitude is almost independent of the tow speed, as expected from the independence principle. For the frequencies below and around the peak, the forward speed tend to attenuate the response. The transverse motion follows the same trend, it is speed dependent at low frequencies but not at higher ones. It is also non-zero for low frequencies so it seems likely that the vortex separation never becomes symmetric.

The bars in figures 5.8 - 5.9 gives the 95% confidence interval. This interval varies significantly between frequencies for the same velocity, and between velocities for the same frequency. The reason for this is unclear, but seems to be physical and is most likely related to some kind of interference or memory effect.

5.3.2 Traces of in-plane motion

The figures 5.10 - 5.13 show the trace of the y-z motion of the cable. The coordinate system used here is the same as in figure 5.2, with z as in-line and y as the transverse direction.

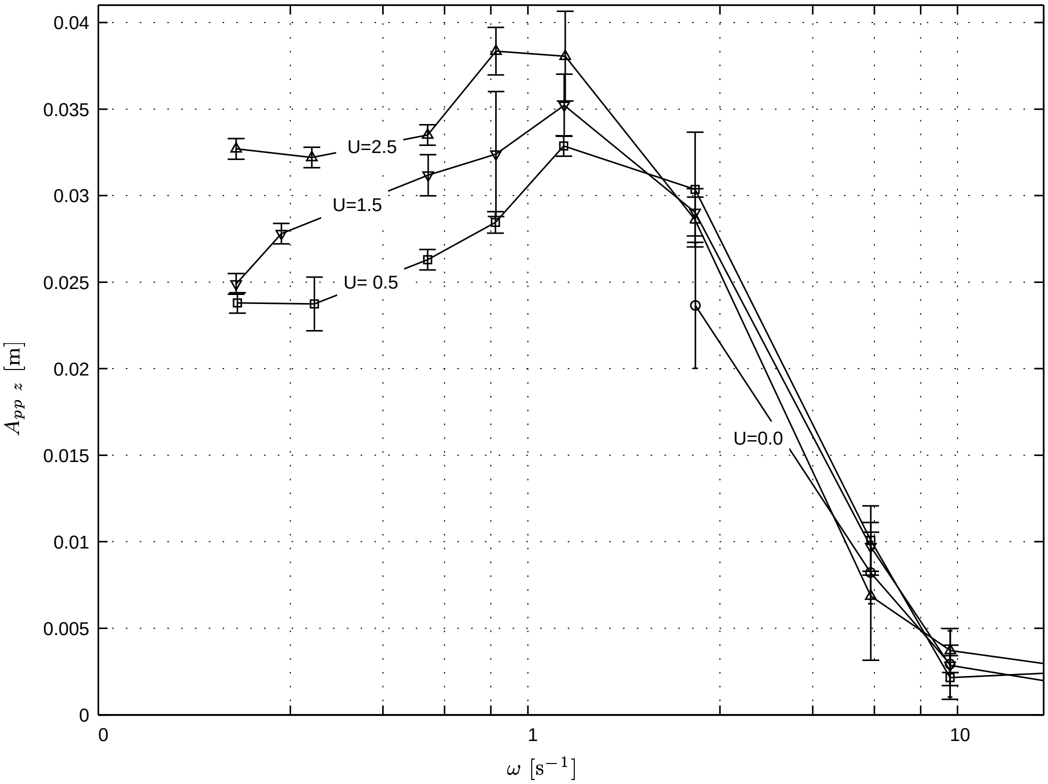

Figure 5.8: *In-line peak to peak amplitude of the dynamic response at $x/L = 0.77$. Peak to peak amplitude for forced motion at $x/L = 0$ iss $A_{0pp} = 0.1$ m. Frequency scale is logarithmic, indicated tow speeds U in ms^{-1}, and bars represent 95% confidence interval.*

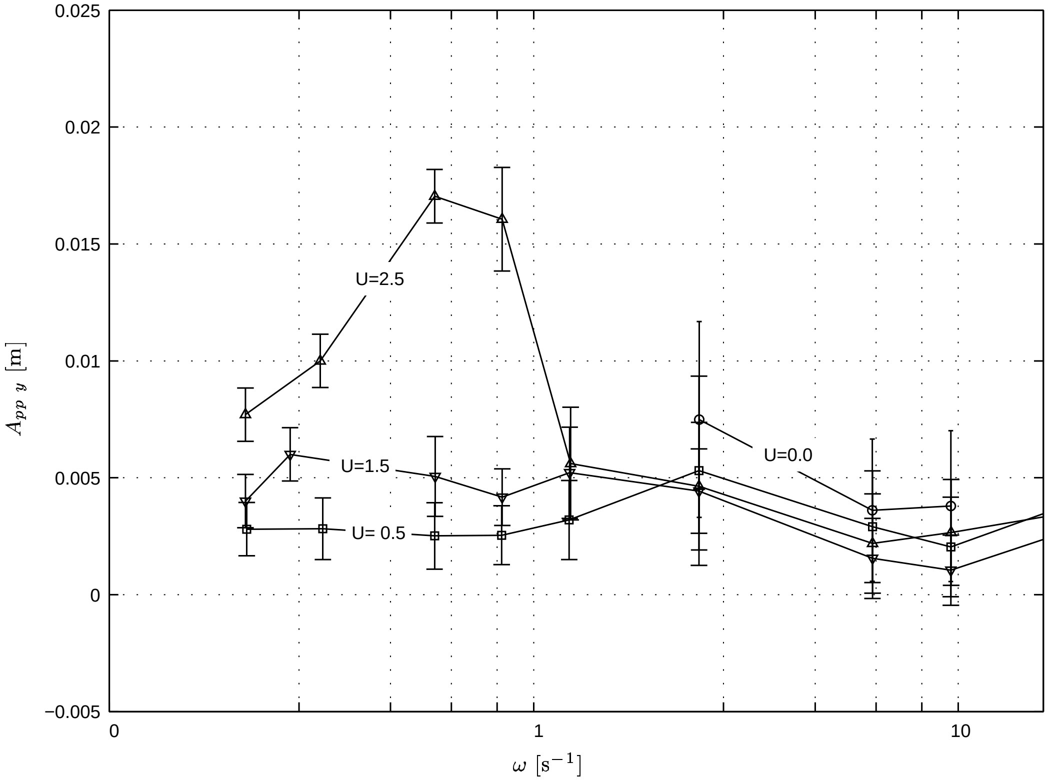

Figure 5.9: *Transverse peak to peak amplitude of the dynamic response at $x/L = 0.77$. Peak to peak amplitude for forced motion at $x/L = 0$ is $A_{0pp} = 0.1$ m. Frequency scale is logarithmic, indicated tow speeds U in ms^{-1}, and bars represents 95% confidence interval*

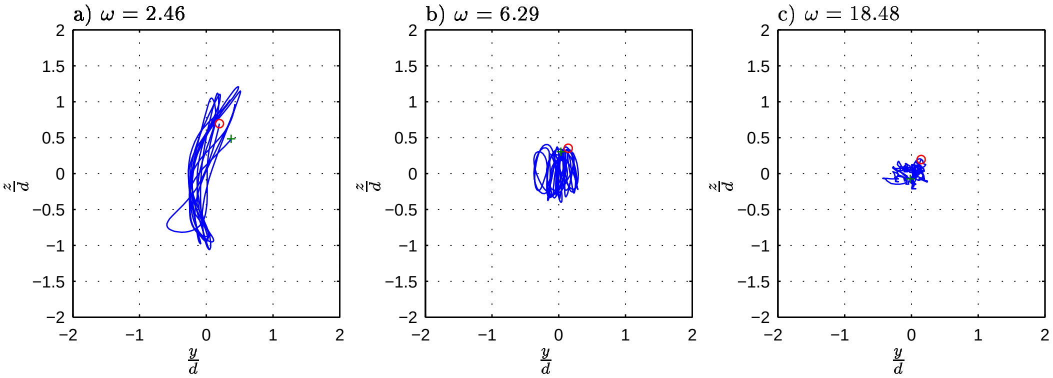

Figure 5.10: *Trace of motion in transverse plane at x/L=0.77, tow speed U=0.0 ms^{-1}, and forced motion amplitude in tow point $A_0/d = 4.5$.*

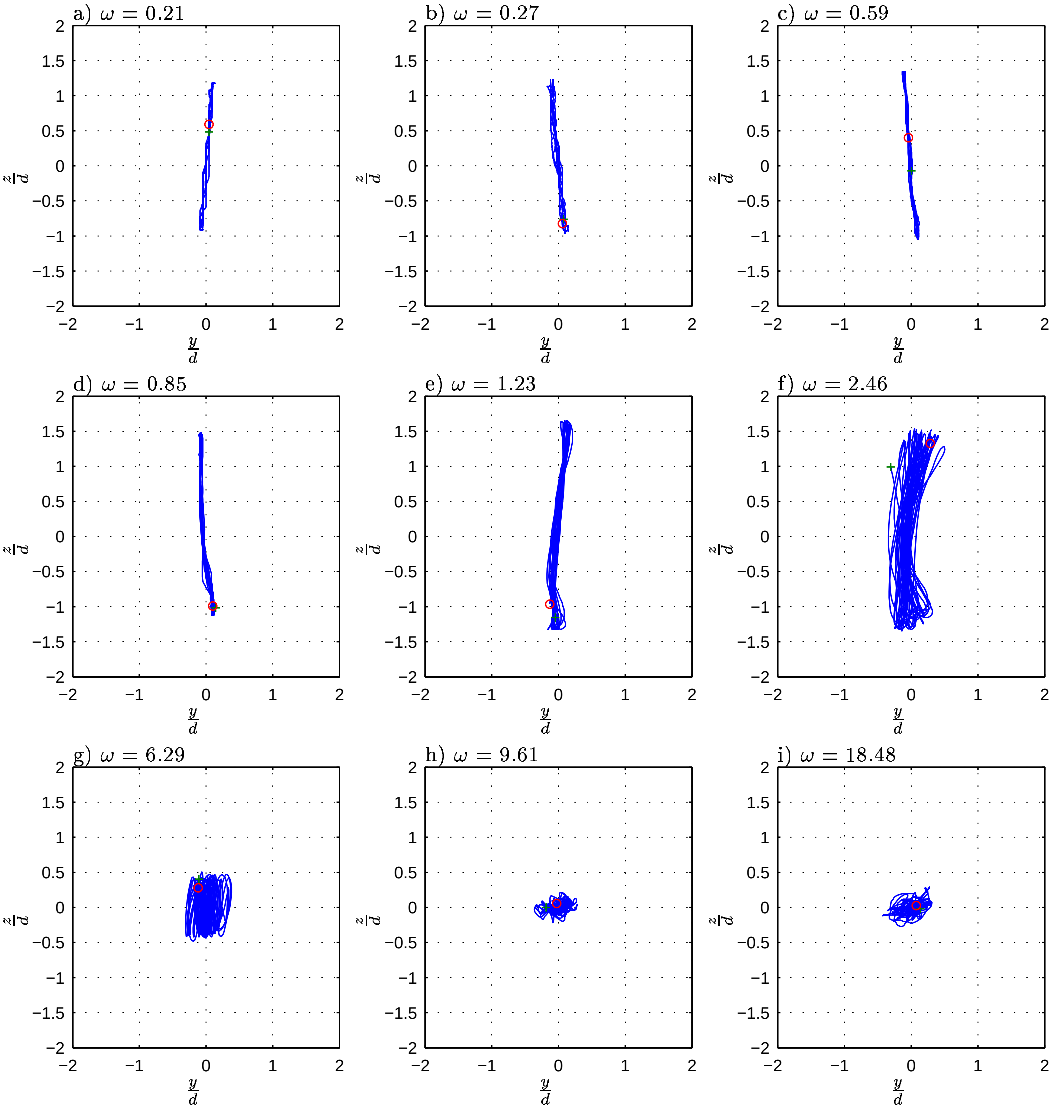

Figure 5.11: *Trace of motion in transverse plane at x/L=0.77, tow speed U=0.5 ms*$^{-1}$*, and forced motion amplitude in tow point* $A_0/d = 4.5$*.*

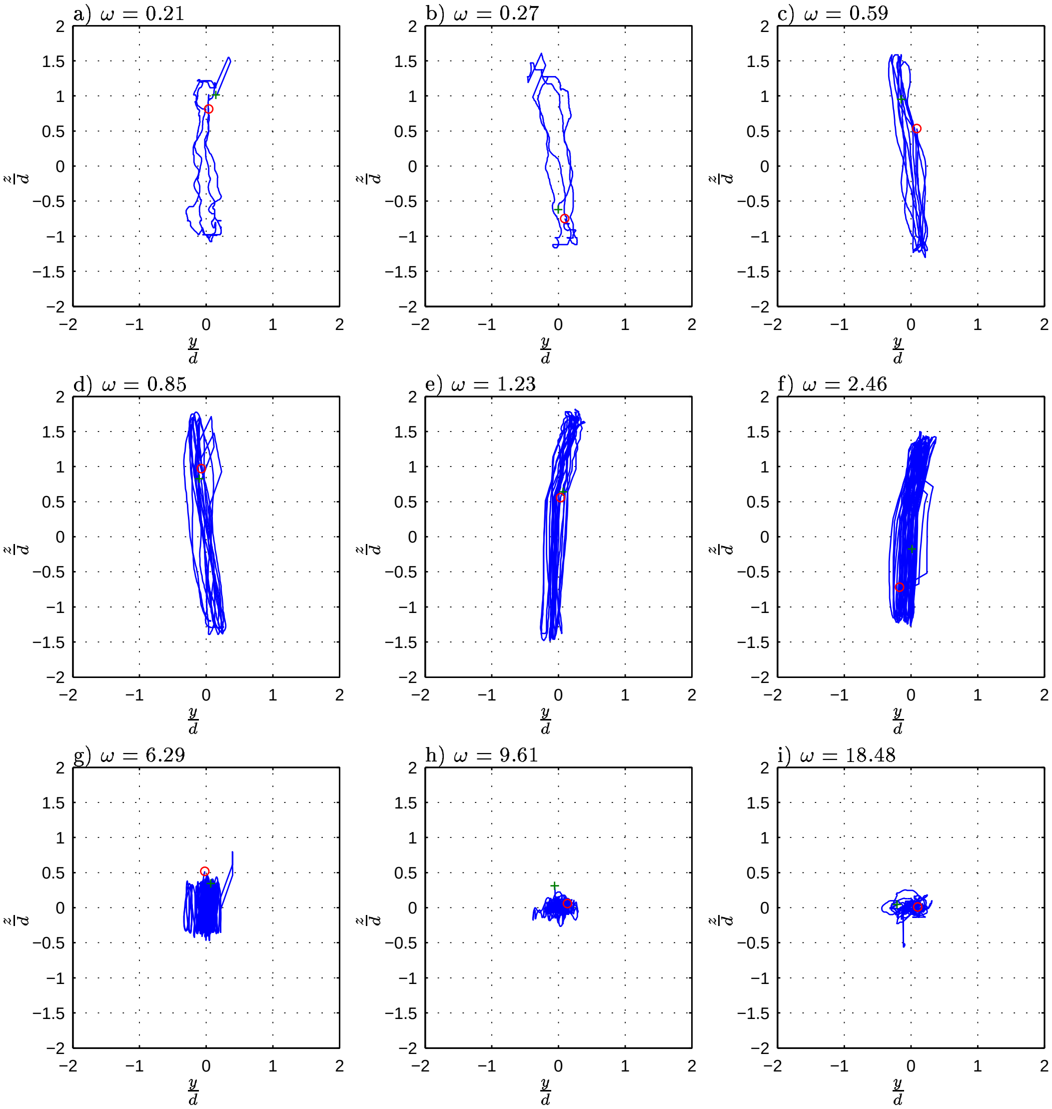

Figure 5.12: *Trace of motion in transverse plane at x/L=0.77, tow speed U=1.5 ms*$^{-1}$*, and forced motion amplitude in tow point* $A_0/d = 4.5$.

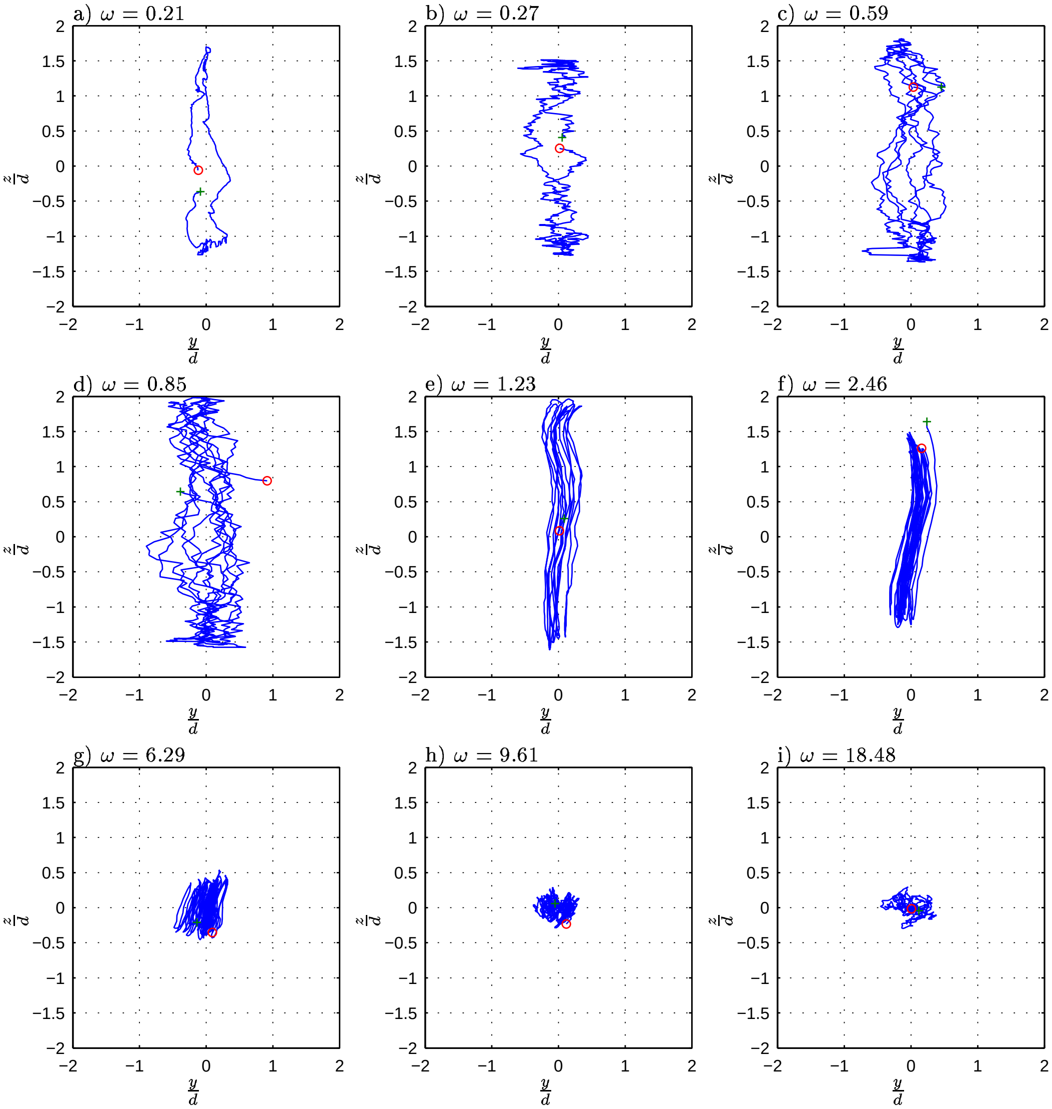

Figure 5.13: *Trace of motion in transverse plane at* x/L*=0.77, tow speed* U*=2.5* ms^{-1}*, and forced motion amplitude in tow point* $A_0/d = 4.5$.

CHAPTER 6

Linear model of a flexible cylinder

The linearized equation described in this chapter was developed by Paidoussis (1966) and discussed among others by Ablow and Schechter (1983), Kennedy (1987), Triantafyllou and Chryssostomidis (1988) and Dowling (1988). The main assumption in this context is that the transverse motions and velocities are small compared to the axial dimension and velocity. Here internal forces in the cable is limited to the effect of tension, while bending stiffness and material damping is neglected.

6.1 Equation of motion

The system is a long cylindrical body with length L and diameter d in an infinite fluid with density ρ, flowing with uniform velocity U parallel to the x axis. The upstream cylinder end is assumed fixed or having a described transverse motion. The downstream end is assumed connected to a transverse spring. The tension is assumed to be larger than zero at all locations, also at the downstream end. The case of a free end is discussed in length by e.g Dowling (1988) but will not be considered here. The coordinate system is shown in figure 6.1.

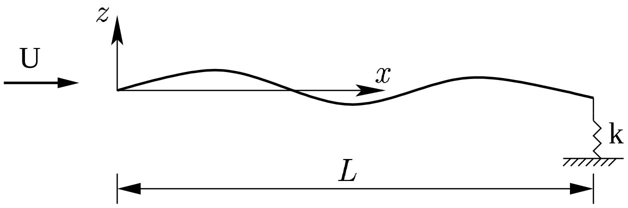

Figure 6.1: Coordinate system for linear model of a towed, flexible cylinder.

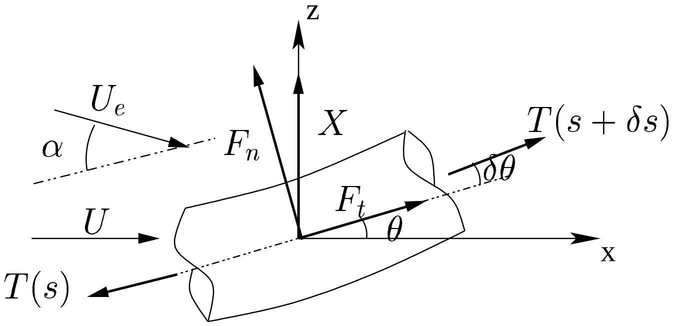

Figure 6.2: Cylinder element and forces.

The cylinder is assumed to have uniform cross-section area S and constant mass per unit length q. A small element of the cylinder with length δs is shown in figure 6.2. The relative velocity between the element and the surrounding fluid is given by:

$$V = \sqrt{U^2 + \left(\frac{\partial z}{\partial t}\right)^2} \tag{6.1}$$

$$\alpha = \arctan\left(\frac{1}{U}\frac{\partial z}{\partial t}\right) + \theta \tag{6.2}$$

Neglecting the effect of bending stiffness of the cable and assuming no elongation the equation of motion in a fixed coordinate system is:

$$q\delta s\frac{\partial^2 x}{\partial t^2} = -T(s)\cos(\theta) + T(s+\delta s)\cos(\theta+\delta\theta) + \delta s\left(F_t\cos(\theta) - F_n\sin(\theta)\right) \tag{6.3}$$

$$\begin{aligned} q\delta s\frac{\partial^2 z}{\partial t^2} &= -T(s)\sin(\theta) + T(s+\delta s)\sin(\theta+\delta\theta) \\ &\quad +\delta s\left(F_n\cos(\theta) + F_t\sin(\theta)\right) + X \end{aligned} \tag{6.4}$$

where all parameters and forces are per unit length. For a towed array that is close to neutral in water it will be assumed that θ is small, so that:

$$\begin{aligned} cos(\theta) &\simeq 1 \\ sin(\theta) &\simeq \frac{\partial z}{\partial x} \\ \delta s &\simeq \delta x \\ s &\simeq x \end{aligned}$$

Dividing the equation by δx and taking the limit as $\delta x \rightarrow 0$ gives:

$$q\frac{\partial^2 x}{\partial t^2} = \frac{\partial}{\partial x}T(x) + F_t - F_n\frac{\partial z}{\partial x} \tag{6.5}$$

$$q\frac{\partial^2 z}{\partial t^2} = \frac{\partial}{\partial x}\left(T(x)\frac{\partial z}{\partial x}\right) + F_n + F_t\frac{\partial z}{\partial x} + X \tag{6.6}$$

The expressions for the tension terms are found by keeping the first order terms of Taylor expansions of $T(s+\delta s)$ and realizing that $\theta + \delta\theta$ is also small.

Here the tension is written as a function of x only, thus any dynamic variation in the tension is neglected. This seems to be reasonable as long as the transverse motion is not large, the tow velocity is constant and the oscillation frequencies are not to large, see chapter 5.

6.1.1 External Forces

The hydrodynamic force on the cylinder is a function of the local relative velocity and the local angle of incidence. In the following it will be assumed that the angle of incidence is small, so that:

$$V^2 \simeq U^2, \text{ and } \alpha \simeq \frac{1}{U}\frac{\partial z}{\partial t} + \frac{\partial z}{\partial x} \tag{6.7}$$

Further, the total hydrodynamic force on the cylinder is divided into a tangential component (F_t), and a normal component (F_n). The normal component will again be written as a sum of a potential flow term (F_{np}) and a term due to viscous effects, denoted F_{nv}.

The potential force is given by slender body theory discussed in chapter 2.

$$\begin{aligned} F_{np} &= -\left(\frac{\partial}{\partial t} + U\frac{\partial}{\partial x}\right)(v\ a) \\ &= -a\left(\frac{\partial}{\partial t} + U\frac{\partial}{\partial x}\right)^2 z \\ &= -a\frac{\partial^2 z}{\partial t^2} - a\frac{\partial}{\partial x}\left(2U\frac{\partial z}{\partial t} + U^2\frac{\partial z}{\partial x}\right) \end{aligned} \tag{6.8}$$

Here $v = \frac{\partial z}{\partial t} + U\frac{\partial z}{\partial x}$ is the relative velocity between the element and the fluid, normal to the cable axis. The two dimensional added mass a is considered constant along the cable except at the boundaries.

The viscous effect per unit length of the cylinder is written

$$F_{nv} = -C_n\,\frac{1}{2}\rho V^2\,d. \tag{6.9}$$

The form and value of the coefficient C_n will be discussed in section section 6.3. Following Paidoussis (1966) it can be written

$$F_{nv} = C_n\,\frac{1}{2}\rho U\left(\frac{\partial z}{\partial t} + U\frac{\partial z}{\partial x}\right)\ d \tag{6.10}$$

The tangential force is assumed to be a result of skin friction only and is written as

$$F_t = \pi C_f\,\frac{1}{2}\rho U^2\,d. \tag{6.11}$$

In general C_f is a function of location x and possibly time t and is here made non-dimensional by the vetted area of the cable. For implementation a coefficient averaged over the length of the cable will be used: $C_F = \frac{1}{L}\int_L C_f\ dx$. In equation (6.11) only first order terms of the time derivative $\frac{\partial z}{\partial t}$ are kept, thus the angle α should be small.

The body force X is the sum of weight and buoyancy forces on the cylinder. Following Faltinsen (1990) these are:

$$X = -qg\delta s + \rho g S\delta s + \rho g S\frac{\partial}{\partial s}\left((h+z)\sin(\theta)\right) \tag{6.12}$$

The mass per unit length of the cable is denoted q and δs is a small length along the cylinder. The last term is a correction for not integrating the pressure over a closed surface where h is the water depth of the coordinate origin. Dividing by δs and taking the limit as $\delta s \rightarrow 0$ gives:

$$X_z = -W + B\left(1 + h\left(\frac{\partial^2 z}{\partial x^2}\right)\right) \tag{6.13}$$

This assumes small angle approximation and only linear terms in z and it's derivatives are kept. $W = qg$ is the dry weight and $B = \rho g S$ is the buoyancy, both per unit length of the cable. The last term has a component in the x-direction that is not shown in figure 6.2 or equation (6.3):

$$X_x = B\frac{\partial z}{\partial x} \tag{6.14}$$

Note that these terms do not disappear for a neutral cable. In the literature on heavy cables like mooring lines these terms are usually combined with the tension to form a so called effective tension, see Faltinsen (1990).

6.1.2 Linear equations

Substituting for the force terms in equation (6.5) and equation (6.6) gives a set of coupled equations:

$$\begin{aligned} q\frac{\partial^2 x}{\partial t^2} &= \frac{\partial}{\partial x}T(x) + \pi C_F\frac{1}{2}\rho dU^2 - B\frac{\partial z}{\partial x} && (6.15)\\ (q+a)\frac{\partial^2 z}{\partial t^2} &= \frac{\partial}{\partial x}\left(T(x)\frac{\partial z}{\partial x}\right) - 2aU\frac{\partial^2 z}{\partial x\partial t} - aU^2\frac{\partial^2 z}{\partial x^2} + \pi C_F\frac{1}{2}\rho dU^2\frac{\partial z}{\partial x} \\ &\quad -C_n\frac{1}{2}\rho dU\left(\frac{\partial z}{\partial t} + U\frac{\partial z}{\partial x}\right) - W + B\left(1 + h\left(\frac{\partial^2 z}{\partial x^2}\right)\right) && (6.16)\end{aligned}$$

Here only first order terms in $\frac{\partial z}{\partial x}$ and $\frac{\partial z}{\partial t}$ are kept. with the exception of the quadratic normal force term. Collecting terms of equal order

$$\begin{aligned} q\frac{\partial^2 x}{\partial t^2} &= \frac{\partial}{\partial x}T(x) + f_t - B\frac{\partial z}{\partial x} && (6.17)\\ m\frac{\partial^2 z}{\partial t^2} &= \frac{\partial}{\partial x}\left(Q(x)\frac{\partial z}{\partial x} - a_1\frac{\partial z}{\partial t}\right) + f_t\frac{\partial z}{\partial x} - f_{n1}\left(\frac{1}{U}\frac{\partial z}{\partial t} + \frac{\partial z}{\partial x}\right) - w && (6.18)\end{aligned}$$

Here

$$\begin{aligned} m &= q+a && (6.19)\\ Q(x) &= T(x)-aU^2+Bh && (6.20)\\ a_1 &= 2aU && (6.21)\\ f_t &= \pi C_F \frac{1}{2}\rho d U^2 && (6.22)\\ f_{n1} &= C_{n1}\frac{1}{2}\rho d U^2 && (6.23)\\ w &= W-B \end{aligned}$$

Equation (6.17) and equation (6.18) are linear and can be written as a sum of a static and a dynamic part. The solution is then written

$$z(x,t) = z_s(x)+z_d(x,t) \tag{6.24}$$

Inserting in equation (6.17) gives:

$$0 = \frac{\partial}{\partial x}T(x)+f_t-B\frac{\partial z_s}{\partial x} \tag{6.25}$$

For the assumption of inextensible cable to be valid some oscillation must be allowed in the x direction. On the other hand these are assumed so small that the inertia terms in this direction may be neglected, and only the static part of the equation is left.

For the transverse direction equation (6.18) is divided in a static and a dynamic part

$$\begin{aligned} 0 &= \frac{\partial}{\partial x}\left(Q(x)\frac{\partial z_s}{\partial x}\right)+f_t\frac{\partial z_s}{\partial x}-f_{n1}\left(\frac{\partial z_s}{\partial x}\right)-w && (6.26)\\ m\frac{\partial^2 z_d}{\partial t^2} &= \frac{\partial}{\partial x}\left(Q(x)\frac{\partial z_d}{\partial x}-a_1\frac{\partial z_d}{\partial t}\right)+f_t\frac{\partial z_d}{\partial x_d}-f_{n1}\left(\frac{1}{U}\frac{\partial z_d}{\partial t}+\frac{\partial z_d}{\partial x}\right) && (6.27) \end{aligned}$$

Equation (6.25) and equation (6.26) represents the static problem with $T(x)$ and z_s as unknowns. The transverse dynamics is given by equation (6.27), with tension known from the static solution.

6.1.3 Boundary Conditions

In the case of a seismic cable, some sort of support will be present in both ends of the cable in the form of lead-ins and tail-buoy towing lines. At the upstream end, $x=0$, the displacement is set equal to some prescribed motion

$$z(0,t) = Z_0 + A_0\sin(\omega t) \tag{6.28}$$

Where z_0 is the initial position of the tow point and A_0 the amplitude of the harmonic motion. In slender body theory the instantaneous change of diameter of the beginning of the cylinder should give rise to a infinite force at the upstream end. This is neglected here, mainly on the argument that there is a tow cable upstream, thus the transition is smooth. The effect may have to be addressed more closely if this tow cable is included in the model. With the harmonic boundary condition in equation (6.28) the problem is avoided since the force at the boundary is not considered.

At the downstream end, $x = L$, the boundary is modeled as a transverse spring and a tension.

$$\begin{aligned} \left[Q(x)\frac{\partial z_d}{\partial x} - a_1\frac{\partial z_d}{\partial t} \right]_{x=L} &= -kz|_{x=L} && (6.29) \\ T(x)|_{x=L} &= T_a && (6.30) \end{aligned}$$

The spring k on the right of equation (6.29) may be a linearized and simplified expression for the geometric stiffness of a heavy tow line or drogue, or it may be a simple control device. In all cases it is assumed to apply a constant tension in the cylinder. The left hand side of equation (6.29) can be rewritten

$$\left[Q(x)\frac{\partial z_d}{\partial x} - a_1\frac{\partial z_d}{\partial t} \right]_{x=L} = \left[T_a\frac{\partial z}{\partial x} - 2\,aU\left(\frac{\partial z}{\partial t} + U\frac{\partial z}{\partial x} \right) + Bh\frac{\partial z}{\partial x} \right]_{x=L} \qquad (6.31)$$

With the exception of the buoyancy term this is the form discussed by Paidoussis (1966), Triantafyllou and Chryssostomidis (1988) and Dowling (1988). The term $2\,aU\left(\frac{\partial z}{\partial t} + U\frac{\partial z}{\partial x}\right)$ describes the change in fluid momentum at the aft end of the cable. In the case of a free end the details are important, and the factor 2 is replaced by an empirical factor accounting for the three dimensionality of the flow at the tail end. For the present case the normal component of the applied aft tension $T_a\frac{\partial z}{\partial x}$ and the spring (or proportional regulator) on the left hand side will dominate, thus details of the flow are not further discussed. The form in equation (6.29) gives a so-called natural boundary condition in numerical methods and are therefore preferable.

6.2 Solutions for the Linear Equation

Analytic solutions of the linear equations unfortunately seem to have limited validity for real problems. They are on the other hand very useful for verification of numerical tools.

6.2.1 Static shape and tension

The static problem is given by equation (6.25) and equation (6.26) The result is a system of equations:

$$\begin{aligned} \frac{\partial}{\partial x}T(x) + f_t - B\frac{\partial z_s}{\partial x} &= 0 \\ \frac{\partial}{\partial x}\left(Q(x)\frac{\partial z_s}{\partial x} \right) + f_t\frac{\partial z_s}{\partial x} - f_{n1}\left(\frac{\partial z_s}{\partial x} \right) - w &= 0 \end{aligned}$$

Integrating the first equation and applying the downstream boundary condition in equation (6.30) gives

$$T(x) = T_a + f_t\,l - f_t\,x + B(z_s - z_s|_{x=L}) \qquad (6.32)$$

and

$$Q(x) = T_a + f_t\,l - f_t\,x + B(z_s - z_s|_{x=L} + h) - aU^2 \tag{6.33}$$

Inserting in the second equation and performing the derivation gives

$$(a_0 - f_t\,l)\,\frac{\partial^2 z_s}{\partial x^2} - f_{n1}\left(\frac{\partial z_s}{\partial x}\right) - w \quad = 0 \tag{6.34}$$

$$a_0 = T_a + f_t\,l - aU^2 + Bh \tag{6.35}$$

assuming $z_s - z_s|_{x=L} << h$. The solution is

$$z_s = C_1 - C_2\,(a_0 - f_t\,x)^{1-\frac{f_{n1}}{f_t}} - \frac{w\,x}{f_{n1}} \tag{6.36}$$

The coefficients are given by the system of equations:

$$\begin{aligned} C_1 - C_2\,a_0^{1-\frac{f_{n1}}{f_t}} &= Z_0 \\ -C_2\,\left(f_t - f_{n1}\right)(a_0 - f_t\,L)^{1-\frac{f_{n1}}{f_t}} - \frac{w}{f_{n1}}\,(a_0 - f_t\,L) & \\ = k\left(C_1 - C_2\,(a_0 - f_t\,L)^{1-\frac{f_{n1}}{f_t}} - \frac{w\,L}{f_{n1}}\right) & \end{aligned} \tag{6.37}$$

This solution of course requires that all parameters are constant along the cable.

6.2.2 Response Amplitude

To find the motion response amplitude along the cable due to a harmonic input at the tow point, the solution is expressed by

$$z_d(x,t) = \eta(x)\mathrm{e}^{i\omega t} \tag{6.38}$$

where $\eta(x)$ may be complex, describing amplitude and phase lag along the cable. Inserting this in equation (6.27) gives the equation

$$-m\omega^2\eta - \frac{\partial}{\partial x}\left((a_0 - f_t x)\frac{\partial \eta}{\partial x} - a_1 i\omega\eta\right) - f_t\frac{\partial \eta}{\partial x} + f_{n1}\left(\frac{i\omega\eta}{U} + \frac{\partial \eta}{\partial x}\right) = 0 \tag{6.39}$$

for the amplitude of oscillation as function of frequency. The coefficients are given in equations (6.19) - (6.24) and equation (6.35). Performing the derivation and collecting terms:

$$(-a_0 + f_t x)\frac{\partial^2 \eta}{\partial x^2} + d_\eta\frac{\partial \eta}{\partial x} + k_\eta \eta = 0 \tag{6.40}$$

where a_0 and f_t are defined as above, and

$$d_\eta \;=\; f_{n1} + a_1 i\omega \tag{6.41}$$

$$k_\eta \;=\; -m\omega^2 + f_{n1}\frac{i\omega\eta}{U} \tag{6.42}$$

A solution of equation (6.40) is:

$$\begin{aligned} \eta(x) &= \bar{x}^n \left(C_1 J_n(\bar{x}) + C_2 Y_n(\bar{x})\right) \\ n &= \frac{f_t - d_\eta}{f_t} \\ \bar{x} &= 2\sqrt{k_\eta}\sqrt{\frac{-a_0 + f_t x}{f_t^2}} \end{aligned} \tag{6.43}$$

where $J_n(x)$ and $Y_n(x)$ are Bessel functions of order n of the first and second kind, respectively. Note that both order and argument are complex numbers. The boundary conditions for the dynamic problem with forced oscillation of the tow point are:

$$z_d(0,t) = A_0 \sin(\omega t) \tag{6.44}$$

$$\left[(a_0 - f_t x)\frac{\partial \eta}{\partial x} - a_1\, i\omega\eta\right]_{x=L} = -k\eta(L,t) \tag{6.45}$$

$$\tag{6.46}$$

For the tow point

$$\begin{aligned} A_0 &= \bar{x}_0{}^n \left(C_1 J_n(\bar{x}_0) + C_2 Y_n(\bar{x}_0)\right) \\ \bar{x}_0 &= 2\sqrt{k_\eta}\sqrt{\frac{a_0}{a_1^2}} \end{aligned} \tag{6.47}$$

The derivative of equation (6.43) with respect to x (Spiegel 1968):

$$\begin{aligned} \frac{\mathrm{d}\eta(x)}{\mathrm{d}x} &= \frac{\mathrm{d}\bar{x}}{\mathrm{d}x}\frac{\mathrm{d}}{\mathrm{d}\bar{x}}\left(\bar{x}^n C_1 J_n(\bar{x}) + \bar{x}^n C_2 Y_n(\bar{x})\right) \\ &= \frac{\sqrt{k_\eta}}{\sqrt{-a_0 + f_t x}}\bar{x}^n \left(C_1 J_{n-1}(\bar{x}) + C_2 Y_{n-1}(\bar{x})\right) \end{aligned} \tag{6.48}$$

The downstream condition from equation (6.45) then is:

$$\begin{aligned} &\sqrt{k_\eta}\sqrt{-a_0 + f_t L}\left(C_1 J_{n-1}(\bar{x}_L) + C_2 Y_{n-1}(\bar{x}_L)\right) \\ &\quad = (-k + a_1 i\omega)\ \left(C_1 J_n(\bar{x}_L) + C_2 Y_n(\bar{x}_L)\right) \\ &\quad \bar{x}_L = 2\sqrt{k_\eta}\sqrt{\frac{a_0 + a_1 L}{a_1^2}} \end{aligned} \tag{6.49}$$

Unfortunately this solution is not very robust, particularly in solving for the coefficients. Therefore two approximations were made: The imaginary term in equation (6.41) is neglected, this corresponds to neglecting a slender body term in the hydrodynamic force. Also, the ratio f_t/f_{n1} is assumed $\simeq 1$, which should be true for unseperated flow.

In the cases where $f_t l << a_0$ (as in the experiment), the tension may be considered constant along the cable. Using average tension, equation (6.40) becomes:

$$\left(-a_0 + f_t\frac{l}{2}\right)\frac{\partial^2 \eta}{\partial x^2} + d_\eta\frac{\partial \eta}{\partial x} + k_\eta \eta = 0 \tag{6.50}$$

This is a damped wave equation. The solution is

$$\eta(x) = C_1 \mathrm{e}^{\lambda_1 x} + C_2 \mathrm{e}^{\lambda_2 x} \tag{6.51}$$

where

$$\begin{aligned}\lambda_1 &= 1/2 \frac{d_\eta + \sqrt{d_\eta^2 + 4 d_\eta (a_0 - f_t \frac{l}{2})}}{a_0 - f_t \frac{l}{2}} \\ \lambda_2 &= 1/2 \frac{d_\eta - \sqrt{d_\eta^2 + 4 d_\eta (a_0 - f_t \frac{l}{2})}}{a_0 - f_t \frac{l}{2}}\end{aligned}$$

In order to find the coefficients, the boundary conditions in equation (6.44) and equation (6.45) are written as a system of linear equations:

$$\begin{aligned}A_0 &= C_1 + C_2 \\ (a_0 - f_t \frac{L}{2}) \left(C_1 \lambda_1 \mathrm{e}^{\lambda_1 L} + C_2 \lambda_2 \mathrm{e}^{\lambda_2 L}\right) &= (-k + aU\ i\omega) \left(C_1 \mathrm{e}^{\lambda_1 L} + C_2 \mathrm{e}^{\lambda_2 L}\right)\end{aligned} \tag{6.52}$$

Finally there is a low frequency asymptote. Setting $\omega = 0$ and assuming linear damping only, equation (6.40) simplifies to

$$(-a_0 + f_t x) \frac{\partial^2 \eta}{\partial x^2} + f_{n1} \frac{\partial \eta}{\partial x} = 0 \tag{6.53}$$

The solution is

$$\eta(x) = C_1 + C_2 \left(x - \frac{a_0}{f_t}\right)^{1 - \frac{f_{n1}}{f_t}} \tag{6.54}$$

The coefficients are given by the system of equations:

$$\begin{aligned}A_0 &= C_1 - C_2 \left(\frac{a_0}{f_t}\right)^{1 - \frac{f_{n1}}{f_t}} \\ (a_0 - f_t L)\, C_2 \left(1 - \frac{f_{n1}}{f_t}\right) \left(L - \frac{a_0}{f_t}\right)^{-\frac{f_{n1}}{f_t}} &= -k \left(C_1 + C_2 \left(L - \frac{a_0}{f_t}\right)^{1 - \frac{f_{n1}}{f_t}}\right)\end{aligned} \tag{6.55}$$

6.2.3 Results for two model cases

Two model problems are defined as part of the verification process described in chapter 1, and will form a basis for most of the discussions in this chapter. The *low tension case* is assumed to represent a typical section of a seismic streamer between two birds, with boundary conditions representative of proportional controlled birds. The full streamer is described by Pedersen and Sørensen (2001). The *high tension case* models the dynamic response of the experimental setup described in chapter 5. Parameters are given in table 6.1.

The results for the amplitude response are shown in figure 6.3. There are very distinct eigenvalues, the first three are shown. At these frequencies the response is attenuated, for the

Table 6.1: *Parameters for model problems.*

		low tension case	high tension case
Diameter [m]	d	0.07	0.011
Length [m]	L	300	13
Tow depth [m]	h	8	0.5
Aft Tension [N]	T_a	1800	19.6
Aft Spring stiffness [Nm^{-1}]	k	24	48
Mass coefficient	C_m	1	1
Added mass coefficient	C_a	1	1
Friction coefficient	C_F	0.0024	.0036
Normal force coefficient	C_n	$\pi\, C_f$	$\pi\, C_f$
Tow Speed [ms^{-1}]	U	2.2	1.5
Excitation Amplitude [m]	A_0	1.0	.05
Excitation Frequency [rads^{-1}]	ω	0.01-0.6	0.1-10

high tension case more than three times the input amplitude. This contradicts the results found in the experiments and the normal assumption that high frequencies are damped out along a towed array (Triantafyllou and Chryssostomidis 1988). The reason for this discrepancy is believed to be the modeling of the hydrodynamic force, or damping in this case. This will be discussed below, after discussing a numerical tool for estimating the transverse response.

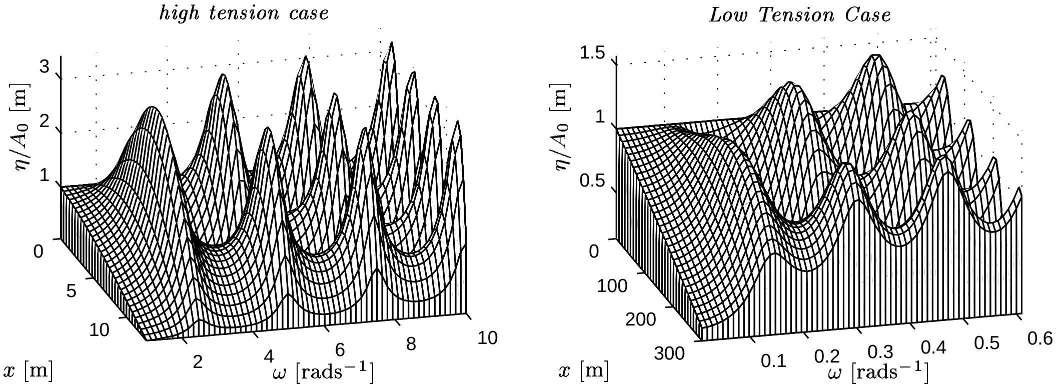

Figure 6.3: *Response amplitude for model cases. For high tension case constant tension is assumed and equation (6.51) is used. For streamer section equation (6.43) is used with order* $n = 0$.

6.2.4 Numerical solution for the Response Amplitude

Since all the analytical solutions found requires some approximations, it seems that a numerical method is necessary. This will also allow nonlinear expressions for the hydrodynamic force.

For the response amplitude in Equation (6.39) the boundary value problem (BVP) solver found in MATLAB®(Math Works Inc. 2000) seems suitable. This solves a system of first order differential equations:

$$\frac{\mathrm{d}y}{\mathrm{d}x} = f(x,y) \tag{6.56}$$

on the interval $x = [a,b]$. The boundary condition is given by:

$$f_{bc}\left(y(a), y(b)\right) = 0 \tag{6.57}$$

The second order problem in equation (6.39) must then be rewritten in a system of two first order equations with a solution vector $y = \left[\frac{\partial \eta}{\partial x}, \eta]\right]^T$:

$$\frac{\mathrm{d}y}{\mathrm{d}x} = \left[\begin{array}{c} y(1) \\ \frac{k_\eta y(2)+d_{eta} y(1)}{(a_0 - f_t x)} \end{array}\right] \tag{6.58}$$

The interval of the domain is of course $x = [0, L]$ and boundary conditions are found by rearranging equations (6.44) - (6.45) .

The solver is a finite difference code that implements the three-stage Lobatto IIIa formula. This is a collocation formula and the collocation polynomial provides a solution that is fourth order accurate uniformly in the interval. Mesh selection and error control are based on the residual of the continuous solution (Math Works Inc. 2000). An initial grid and an error tolerance level are inputs to the solver. In figure 6.4 the error solving for the analytical results above are shown. A relative error level of $1e-4$ gives an error in the solution of less than $2 \times 10^{-3}\%$ and is assumed sufficent.

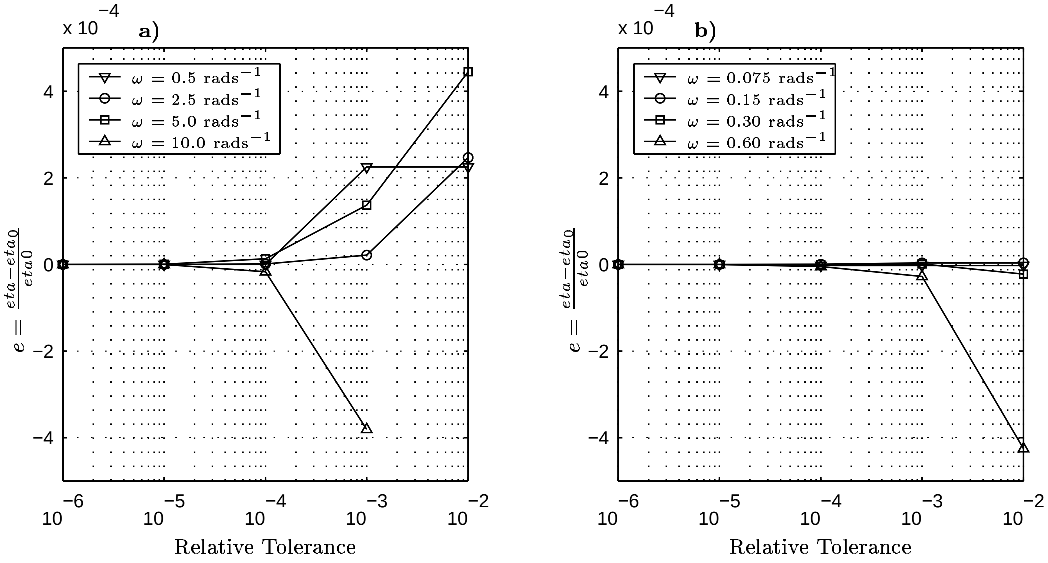

Figure 6.4: *Relative precision error for numerical solution: a) high tension case, the response is taken at* $x = 10$ *m, b) low tension case, the response is taken at* $x = 150$ *m.*

Figure 6.5 illustrates the difference between the approximations made in figure 6.3 and the keeping all terms in equation (6.39). With the exception of the highest frequency the error

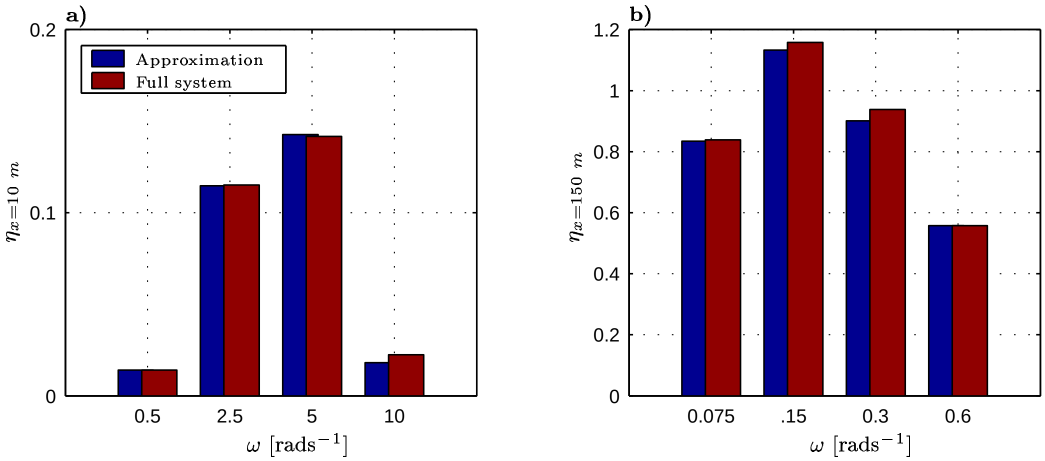

Figure 6.5: *Compared response for approximated analytic solution and the real system: a) high tension case b) low tension case.*

is less than 1% for the high tension case, and less than 4% for the low tension case, but still noticable.

6.2.5 Sensitivity and modeling errors

The influence coefficient shown in table 6.2 describes the sensitivity of the numerical model to small changes in input parameters. The influence coefficient is defined in the same way as in 3:

$$\kappa_i = \frac{1}{A_0} \frac{\partial A}{\partial X_i}\bigg|_{x=10} \tag{6.59}$$

Here A_0 is the amplitude with parameters from table 6.1 and X_i the input parameters. e_{ci} is the relative error due to a change in X_i. The values in table 6.2 are found by changing the input parameter by 10% in both directions, and then calculate the derivative by central difference. Note that the influence coefficient do have dimensions.

From table 6.2 and table 6.3 it is clear that the most important parameters are diameter and hydrodynamic force coefficients. The influence coefficients are for these parameters strong functions of ω, also in sign. The parameter f is a factor on the fluid momentum term in the aft boundary discussed in section 6.1.3. The effect of small changes in the aft boundary conditions T_a,k and f are small, thus more accurate modeling does not seem necessary. Change in tow depth (h) is for example found to be more influential than both the downstream boundary condition and the cable length (L), even for the present case of a neutral cable.

The total modeling error due to uncertainty in input parameters is given by:

$$e_{cP} = \sqrt{\sum_{i=1}^{N} (\kappa_i \Delta X_i)} \tag{6.60}$$

Here N is the numbers of parameters included. Values of ΔX_i for the high tension case may be found from chapter 5. The values of f and k are simply set to 100% and 20% respectively, which

Table 6.2: *Influence coefficients for the high tension case. The values refers to the relative change in amplitude at $x = 10$ m for a unit change in the listed parameter. The second column indicates dimension of the influence coefficients.*

Parameter	$[\kappa_i]$	$\omega = 0.5$ rads^{-1}	$\omega = 2.5$ rads^{-1}	$\omega = 5.0$ rads^{-1}	$\omega = 10.0$ rads^{-1}
d	m^{-1}	15	-47	-98	290
L	m^{-1}	-0.00066	0.01	0.032	0.014
h	m^{-1}	6.5e-006	0.067	0.2	0.15
T_a	N^{-1}	-3.5e-005	0.061	0.13	-0.07
k	mN^{-1}	-0.002	0.00054	0.0062	-0.024
f		9.4e-006	0.0044	0.015	-0.0064
C_m		0.033	-0.26	-1.6	0.18
C_a		0.034	-0.28	-1.6	0.25
C_f		-1.1	19	52	95
C_{n1}		2.8	-82	-70	-31
U		0.038	-0.53	-0.34	0.18

Table 6.3: *Influence coefficients for the low tension case. The values refers to the relative change in amplitude at $x = 150$ m for a unit change in in the listed parameter. The second column indicates dimension of the influence coefficients.*

Parameter	$[\kappa_i]$	$\omega = 0.075$ rads^{-1}	$\omega = .15$ rads^{-1}	$\omega = .3$ rads^{-1}	$\omega = .6$ rads^{-1}
d	m^{-1}	8.3	-19	31	120
L	m^{-1}	0.0022	-0.0085	0.012	0.022
h	m^{-1}	-0.001	0.016	-0.0086	-0.12
T_a	N^{-1}	-2.7e-005	0.00042	-0.00022	-0.003
k	mN^{-1}	-0.0078	0.017	-0.018	-0.024
f		0.0063	0.05	0.071	-0.06
C_m		0.17	-0.24	0.81	3.7
C_a		0.18	-0.22	0.86	3.8
C_f		-9.2	29	-1	-180
C_{n1}		-12	-120	-110	-16
U		-0.043	-0.32	-0.33	-0.37

should be conservative. The value for C_F is valid for $\omega \simeq 2.5$ rads^{-1} and tow speed $U = 1.5$ ms^{-1}. This value is assumed representative for all frequencies and velocities. For the mass coefficient the difference between neutral cable and the result based on actual weight during the experiment is used.

An estimate of the error due to the linearizion of the hydrodynamic force in equation

(6.7) is included by setting:

$$\Delta C_{n1} = C_{n1}\left(\sin\left(\arctan\left(\frac{\omega A_0}{U}\right)\right) - \frac{\omega A_0}{U}\right) \tag{6.61}$$

6.2.6 Effect of structural terms

The equation of motion in this chapter does not include the effect of bending resistance and damping due to the cable structure, on the assumption that these effects are small. Using the maximum values of calculated responses, an estimate of the size of these terms can be made.

The effect of bending resistance and damping in the cable material is modeled by adding the terms

$$EI\frac{\partial^4 z}{\partial x^4} + \eta I\frac{\partial^4 \dot{z}}{\partial x^4} \tag{6.62}$$

in equation (6.6) (Bergan, Larsen, and Mollestad 1986). Here I is the moment of inertia of a section of the cable, E the modulus of elasticity and η the viscous damping of the material. From data sheets of the Tygon tube, $E = 4.5MPa$. This is a restoring force, and by using numerical derivatives of the calculated response, the bending resistance is found to be at most 0.5% of the restoring force due to tension. The effect on the response is then assumed negligible, also in the error analysis.

The material damping η for the Tygon tube is not given in the data sheets, so a system based approach is used to estimate damping. From very simple experiments in air with parts of the Tygon tubing it was estimated that the damping is less than 1% of critical damping, which will be denoted as a damping ratio $\zeta \simeq 0.01$. The damping force is then expressed

$$2q\zeta\omega_{d0}\frac{\partial z}{\partial t} \tag{6.63}$$

where q is the structural mass of the cable and ω_{d0} is the appropriate dry eigenfrequency of the system. This has the same form as the linear part of the hydrodynamic damping so it can be treated as an error in the linear coefficient. This force is found to be about 7% of the linear part of the hydrodynamic force, but possibly as much as 30% for $\omega = 10$ rads^{-1} (and also $\omega_{d0} = 10$ rads^{-1}). The error estimates for structural damping in table 6.4 are calculated by treating the structural damping as and error in the parameter C_{n1}, and the effect on the response is noticeable.

The modeling errors are summarized in table 6.4. The total error is the quadratic sum of errors from numeric method, parameter uncertainty, linearizion and structural damping. The values are strictly speaking valid only for the tow speed of $U = 1.5$ ms^{-1} but will be assumed representative also for other velocities. The main uncertainty lies in the material damping, and since the estimate here is quite rough, this should be further investigated for a real streamer.

6.3 Hydrodynamic forces

From table 6.2 and table 6.3 it was concluded that the model is very sensitive to hydrodynamic coefficients. This, of course, is the reason for the extensive experimental presented in this work

Table 6.4: *Relative modeling errors for the high tension case.*

Source	$\omega = 0.5$ rads^{-1}	$\omega = 2.5$ rads^{-1}	$\omega = 5.0$ rads^{-1}	$\omega = 10.0$ rads^{-1}
Numeric	$1{\times}10^{-4}$	$1{\times}10^{-4}$	$1{\times}10^{-4}$	$1{\times}10^{-4}$
Parameters	0.016	0.006	0.0093	0.012
Linearizion	0.000	$92{\times}10^{-4}$	0.0016	0.007
Structural Damping	0.003	0.063	0.108	0.106
Total	0.016	0.063	0.108	0.107

in the first place. In this section the results from the rigid cylinder experiments are applied to the flexible cylinder.

The linear model in this chapter assumes that the variation in tension along the cable is linear and constant in time, so the only contribution to the tension is a constant friction coefficient both in time and space. An averaged friction coefficient was discussed in chapter 5, and the results from this discussion are used in the model.

The starting point for the following discussion is that the normal forces on the towed cylinder are mainly a function of the local angle of attack, which is a function of time and position. Figure 6.6 gives an indication of the span of angles experienced by the flexible cylinder in the experiment. Here only the part of the angle due to transverse velocity is included, but since the space derivative is small, the figures should be representative. At the tow point ($x/L = 0$) the amplitude of the angle depends very much on the frequency, while at $x/L = 0.77$ this dependence is almost negligible, at least for higher tow speeds. The figure indicates that most of the time the local angle is too low for the cross flow principle to hold.

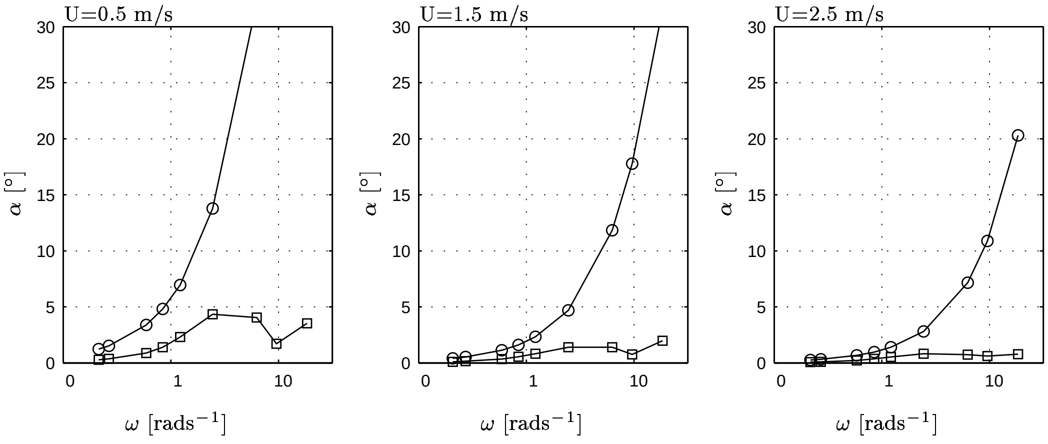

Figure 6.6: *RMS of angle of attack* $\tan(\alpha) = \frac{\omega z_{rms}}{U}$ *at two locations:* ○ $x/L = 0$; □ $x/L = 0.77$.

For the rigid cylinder it was found that the normal force depends on the symmetry of the initial vortexes. For the flexible cylinder it is assumed that the vortex buildup and shedding is always asymmetric, as was found for the oscillating rigid cylinder. That some motion in the bi-normal direction takes place is confirmed by the trace plots in chapter 5.

Table 6.5: *Normal force coefficient for low frequencies.* α_0 *is the local amplitude of angle of attack.*

Id.	Formula	Comment
a)	$C_n = \pi C_F$	Assume friction force parallel with free flow. (Paidoussis 1966)
b)	$C_n = 8R_{ed}^{-\frac{1}{2}} \sin(\alpha_0)^{\frac{3}{2}}$	Friction Coefficient adapted from Taylor (1952) $R_{ed} = \frac{Ud}{\nu}$
c)	$C_n = 4\pi \left(\frac{\pi}{Re_d\ KC}\right)^{\frac{1}{2}} \sin^{\frac{3}{2}}(\alpha_0)$	Drag coefficient for oscillating cylinder adapted from Faltinsen (1990, p. 237)
d)	$C_n = \sin(3°)\sin(\alpha_0)$	Lift Coefficient from Kennedy (1987)
e)	$C_n = 0.08\sin(\alpha_0)$	Linear model for rigid cylinder, see chapter 4

6.3.1 Normal force at low frequencies

Table 6.5 list suggested expression and values for the normal force coefficient at low frequencies, or low angles of attack which in this case is more or less synonymous. Models a)-c) assumes that the flow stay attached to the cylinder and was described in chapter 2. Items d) and e) is believed to be dominated by pressure effects due to their magnitude, and that some form of separation do occur, although Kennedy (1987) explains the linear term as a skin friction force.

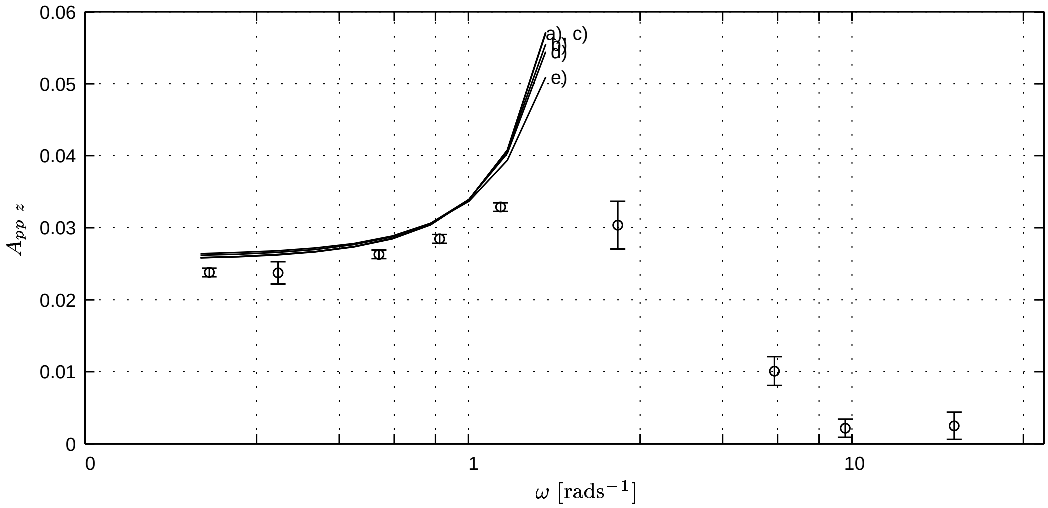

Figure 6.7: *Response amplitude for linear model and flexible cylinder, experiment, tow speed* $U = 0.5$ *m/s :* ○ *Experiments (Bars represents 95% confidence); Curve a) – e); see table 6.5.*

Compared to the experiment as in figures 6.7 - 6.9, the assumption of non-separated flow seems to hold at low frequencies, with a possible exception of the highest tow speed. The

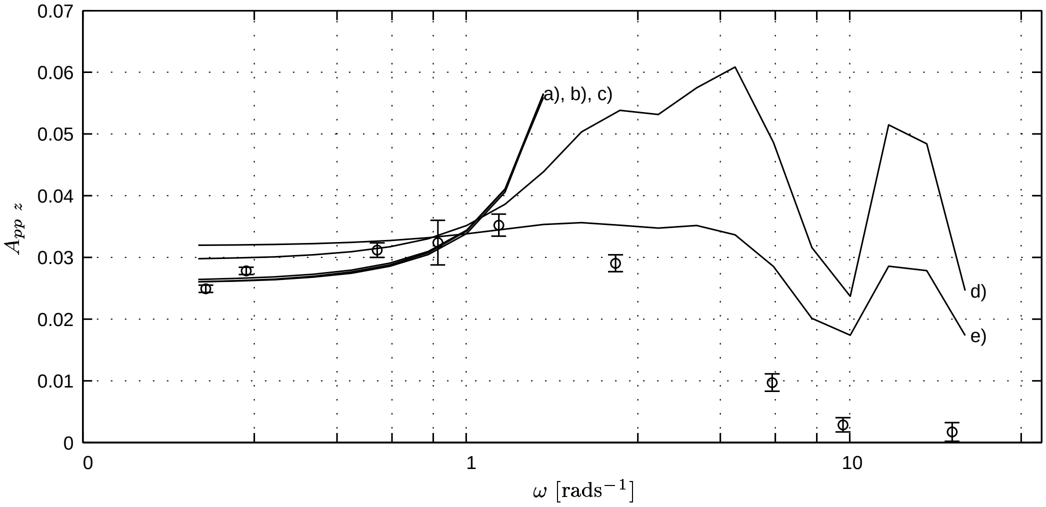

Figure 6.8: *Response amplitude for linear model and flexible cylinder, experiment, tow speed* $U = 1.5$ *m/s* : ○ *Experiments (Bars represents 95% confidence); Curve a) − e); see table 6.5.*

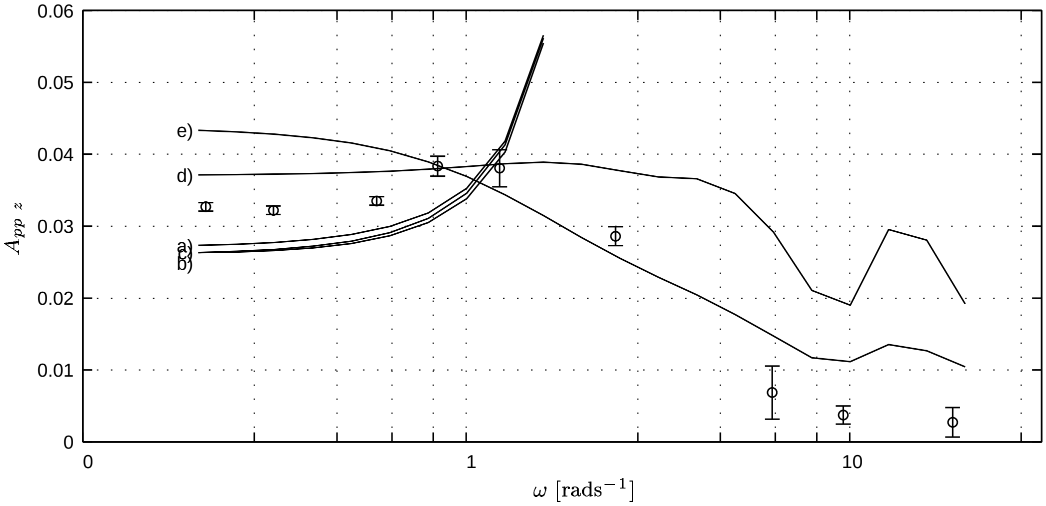

Figure 6.9: *Response amplitude for linear model and flexible cylinder, experiment, tow speed* $U = 2.5$ *m/s* : ○ *Experiments (Bars represents 95% confidence); Curve a) − e); see table 6.5.*

difference in models a), b) and c) are on level with the experimental error, so this cannot be used to distinguish between them. In practice this means that there is no argument for not using the simplest one, model a). For higher frequencies, where higher angle of attacks occur the high values in model d) and e) perform better than friction coefficient in a). Still, these linear models give good results only for a limited range of frequencies. In general, for the lowest frequencies increasing the coefficient increases the response, so in this frequency range the hydrodynamic force acts as a driving force rather than a damping force. This is a result of the angle being dominated by the space derivative term and not the transverse velocity.

Table 6.6: *Coefficients in second order expansion of C_n.*

Id.	C_a	C_{n1}	C_{n2}	Comment
f)	1.0	0.011	0.8	Constant coefficients from chapter 3
g)	0.8	0.0	1.0	Morison's equation with coefficients from chapter 4
h)	0.8	0.08	1.0	Morison's equation with added linear term

6.3.2 Normal force at medium to high frequencies

For low frequencies, the damping was calculated as a linear function of the transverse velocity. When the flow separates, the normal force is dominated by pressure forces, which are usually assumed to be proportional to the square of the normal velocity. This is included in the model in equation (6.39) by adding a term

$$f_{n2}\left(\frac{i\omega\eta}{U}+\frac{\partial\eta}{\partial x}\right)\left|\frac{i\omega\eta}{U}+\frac{\partial\eta}{\partial x}\right| \tag{6.64}$$

Here the angle is still assumed small and

$$\begin{aligned} f_{n2} &= C_{n2}d\frac{1}{2}\rho U^2 \\ \left|i\omega\eta \mathrm{e}^{i\omega t}+U\frac{\partial\eta}{\partial x}\mathrm{e}^{i\omega t}\right| &= \left|i\omega\eta+U\frac{\partial\eta}{\partial x}\right| \end{aligned}$$

This term is readily implemented in the numeric solver described above. To include both linear and quadratic terms is equivalent to formulate the normal force coefficient in equation (6.9) by a second order expansion in α:

$$C_n = C_{n1}\sin(\alpha)+C_{n2}\sin(\alpha)\left|\sin(\alpha)\right|| \tag{6.65}$$

Results for three alternative combinations of coefficients listed in table 6.6 are plotted in figures 6.10 - 6.12. The first of these (model f))is the constant coefficient model based on experiments with constant pitch angle in chapter 3, assuming turbulent boundary layer. The second (model g))is the result from curve fitting Morison's equation in chapter 3, also changing the added mass coefficient. The best correspondence between model and experiment at moderate to high frequencies is obtained by model h) where the linear term from model e) is added to model g). This simply combines the models valid at different angle of attack regimes, and since all regimes are present for the flexible cylinder, this seems like a obvious thing to do. In the next chapter the linear model a) will be combined with this in a time domain simulation that uses the instantaneous value of the angle of attack. In the current frequency domain calculation, the force is calculated based on the amplitude of the angle at each position. This tends to overestimate the force at low to moderate frequencies compared to the result with instantaneous angles.

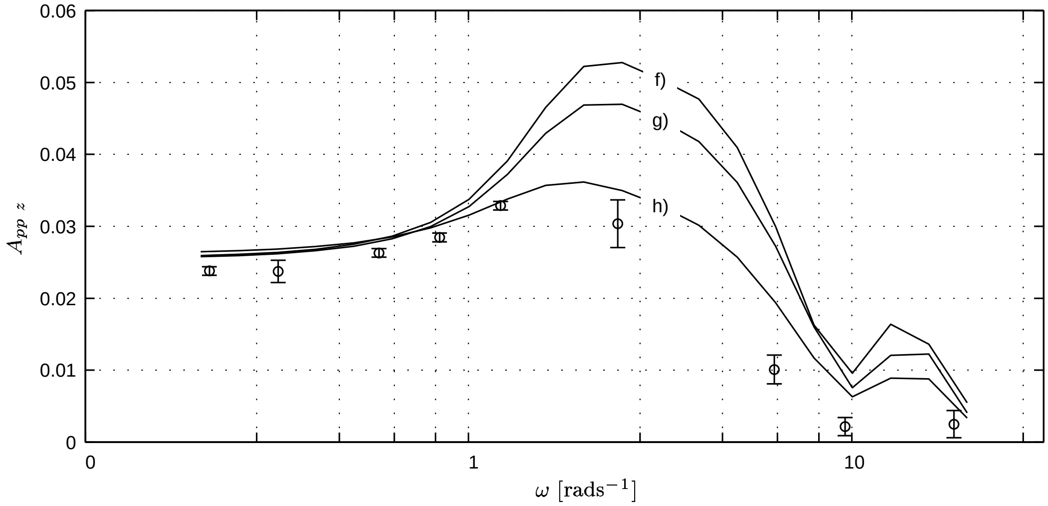

Figure 6.10: *Response amplitude for non-linear model and flexible cylinder, experiment, tow speed* $U = 0.5$ *m/s :* ○ *Experiments (Bars represents 95% confidence); Curve* $f) - h)$*; see table 6.6.*

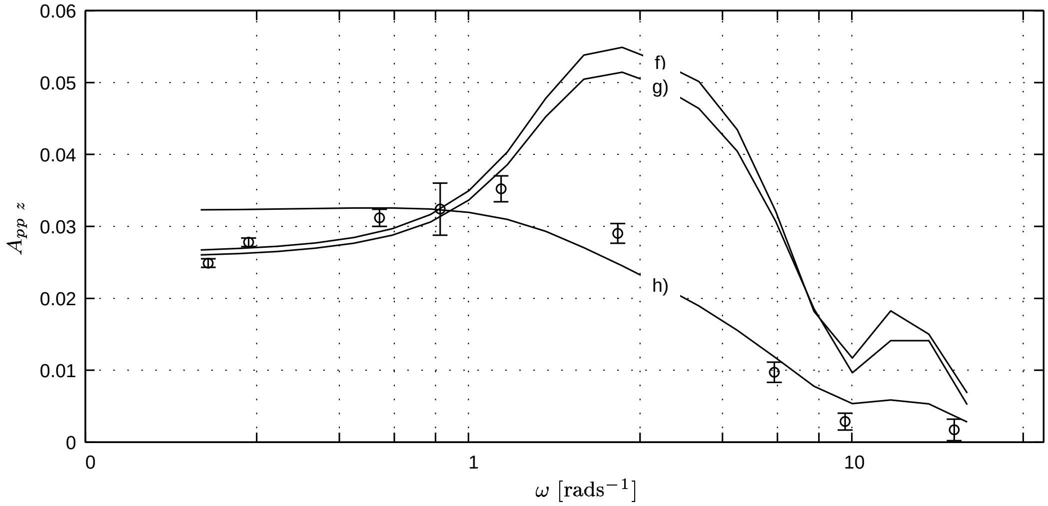

Figure 6.11: *Response amplitude for non-linear model and flexible cylinder, experiment, tow speed* $U = 1.5$ *m/s :* ○ *Experiments (Bars represents 95% confidence); Curve* $f) - h)$*; see table 6.6.*

When slender body theory is used for maneuvering of ships, the part of the hull where separation occurs is not included. For the case of a towed flexible cylinder it will be very difficult to estimate where the flow is attached and where it is separated, and it could be argued that only the first term in equation (6.8) should be kept. In the discussion of figure 6.5 it was found that the difference in the response by dropping the second term are about 4%. The difference in phase is about the same. Considering the uncertainties in the hydrodynamic forces this is not very large, so neglecting it does not introduce a large error. But in cases with low tension and

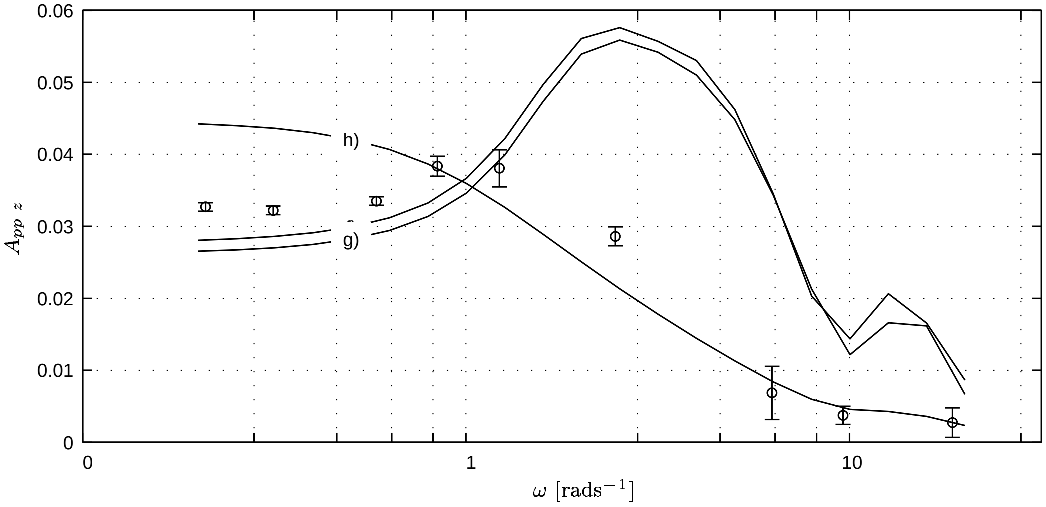

Figure 6.12: *Response amplitude for non-linear model and flexible cylinder, experiment, tow speed* $U = 2.5$ *m/s :* ○ *Experiments (Bars represents 95% confidence); Curve* $f) - h)$*; see table 6.6.*

in particular for a cable with a free end, the second part of equation (6.8) are critical for the stability of the cable (Dowling 1988). The best choice therefore seems to be consistent and keep all potential force terms.

Another argument for neglecting the slender body terms is to facilitate the analytical solution in equation (6.43). Unfortunately the order and arguments in the Bessel functions becomes large negative and complex due to the high linear coefficient. This give a very ill-conditioned system of equation in equation (6.47) and equation (6.49), and cannot be solved in general. The possibility of using an analytical solution with methods for equivalent linear expressions similar to Triantafyllou and Chryssostomidis (1988) is therefore not pursued. On the contrary, the next chapter turns to numerical simulation of the cable in the time domain.

6.4 Conclusions

From experiments and the linear model, some conclusions can now be drawn considering modeling of a flexible cable:

- Although an analytical solution can be found for the response amplitude of a towed array, the applicability is very limited. This because for realistic cases the solution becomes highly oscillatory and unstable. It also require a linear damping model.

- From the sensitivity studies and the comparisons between calculations and experiments it is obvious that a major challenge in modeling towed arrays is the correct estimation of the hydrodynamic forces. A single model valid at all frequencies was not found.

- At very low frequencies the angle of attack was so low that an assumption of no separation seems valid. In this case only the skin friction forces are involved.

- For higher frequencies, the angles of attack increases and the findings for a rigid cylinder in earlier chapters seems valid for this case too. This is in particular tru for the rather high linear term associated with asymmetric vortex shedding in chapters 3 and 4.

CHAPTER 7

Time domain simulation

In this chapter a Finite Element Method (FEM) is developed that can be used for time domain simulation of the transverse motion of a towed flexible cylinder. The method solves the complete solution, so no division into a static and a dynamic part is necessary. The non-linear formulation of the hydrodynamic force from last chapter is incorporated. The assumption of small perturbation of transverse position is kept and tension is still assumed constant in time. As before only the transverse motion in one direction is considered.

7.1 Finite Element Model

The transverse motion is the only dependent variable, and the only non-linear term is the hydrodynamic force. It is then relatively simple to develop a finite element code for the problem, including higher order elements. This is in general a robust and accurate way to numerically solve PDE equations. Alternatives like finite difference schemes and segmented models have also been proposed, particularly for cables with large deformations (Ablow and Schechter 1983; Hover 1997; Vaz and Witz 1997).

7.1.1 Variational Formulation of the equation of motion

Inserting for the tension, equation (6.16) is now written

$$m\frac{\partial^2 z}{\partial t^2} = \frac{\partial}{\partial x}\left((a_0 - f_t x)\frac{\partial z}{\partial x} - a_1\frac{\partial z}{\partial t}\right) + f_t\frac{\partial z}{\partial x} + F(\alpha) - w \tag{7.1}$$

Here the linearized hydrodynamic force term is replaced by a general nonlinear term $F(\alpha) = C_n(\alpha)\frac{1}{2}\rho d V^2$

Multiplying equation (7.1) by a *weight function* $w(x)$ and integrating over the length gives the variational form (see e.g Egeland and Gravdahl (2002)):

$$m\int_L w\frac{\partial^2}{\partial t^2}z\mathrm{d}x + \int_L \frac{\mathrm{d}w}{\mathrm{d}x}\left((a_0 - f_t x)\frac{\partial z}{\partial x} - a_1\frac{\partial z}{\partial t}\right)\mathrm{d}x - \int_L wf_t\frac{\partial z}{\partial x}\mathrm{d}(x) = \int_L w\left(F(\alpha) - X\right)\mathrm{d}x - \left[w\left((a_0 - f_t x)\frac{\partial z}{\partial x} - a_1\frac{\partial z}{\partial t}\right)\right]_{x=0}^{L} \tag{7.2}$$

The second and last term in 7.2 are obtained by integration by parts. This is also known as *weak formulation.* Boundary conditions are either of Neumann type, in which case

$$w\left((a_0 - f_t x)\frac{\partial z}{\partial x} - a_1\frac{\partial z}{\partial t}\right) = g(t) \tag{7.3}$$

where $g(t)$ is given for one or both of $x = 0$ and $x = L$. Alternatively the solution is known on the boundary (Dirichlet condition).

An approximation of the solution is

$$z(x,t) \simeq \sum_{j=1}^{m}\Phi_j(x)q_j(t) \tag{7.4}$$

The functions $\Phi_j(x)$ are usually known as shape functions. Setting $w_j(x) = \Phi_j(x)$ and inserting in equation (7.2) gives, after some rearranging:

$$\boldsymbol{M}\ddot{\boldsymbol{q}} + \boldsymbol{D}\dot{\boldsymbol{q}} + \boldsymbol{K}^a\boldsymbol{q} + \boldsymbol{K}^b\boldsymbol{q} = \boldsymbol{F} + \boldsymbol{F_{bc}} \tag{7.5}$$

here $\boldsymbol{M}, \boldsymbol{D}, \boldsymbol{K^a}, \boldsymbol{K^b}$ are $m \times m$ matrices while $\boldsymbol{q}, \boldsymbol{F}, \boldsymbol{F_{bc}}$ are $m \times 1$ vectors. Superscripts $\dot{()}$ and $\ddot{()}$ denotes first and second time derivatives respectively. The entries of the matrices and vectors in equation (7.5) are given by

$$\boldsymbol{q} = [q_1, q_2, \ldots, q_m]^T \tag{7.6}$$

$$\boldsymbol{M}_{ij} = m\int_L \Phi_i\Phi_j\mathrm{d}x \tag{7.7}$$

$$\boldsymbol{D}_{ij} = a_1\int_L \Phi_i'\Phi_j\mathrm{d}x \tag{7.8}$$

$$\boldsymbol{K}_{ij}^a = \int_L \Phi_i'(a_0 - f_t x)\Phi_j'\mathrm{d}x \tag{7.9}$$

$$\boldsymbol{K}_{ij}^b = -f_t\int_L \Phi_i\Phi_j'\mathrm{d}x \tag{7.10}$$

$$\boldsymbol{F}_{ij} = \int_L \Phi_i(F(\alpha) - X)\mathrm{d}x \tag{7.11}$$

$$\boldsymbol{F_{bc}} = [g_{x=0}, 0, \ldots, 0, g_{x=L}]^T \tag{7.12}$$

Here superscript $(')$ is used to denote the (true) derivative with respect to space variable x. Several choices are possible for the shape functions, like sets of orthogonal functions that satisfies the boundary conditions. Here the FEM is chosen, mostly due to its flexibility in the definition of the system and its natural way of handling moving boundaries.

7.1.2 Lagrange Interpolation Formulas and Finite Element Method

By placing n points equally spaced along the cable, the approximate solution in equation (7.4) can be written:

$$z(x,t) \simeq \hat{z}(x_0 + ph, t) \simeq \sum_k A_k^n(p) q_k \tag{7.13}$$

where x_0 is the position of the first point, p is the new parameter for position, h is the distance between successive points and $A_k^n(p)$ are given by Lagrange interpolation formulas. See Abramowitz and Stegun (1965, p. 878) for expressions and further definitions. Note that for $p = k_i$; $A_k^n(p) = 1$ for $k = k_i$ and $A_k^n(p) = 0$ for $k \neq k_i$. Said another way, the values q_k are the value of $\hat{z}$ in the node points. The matrices in equations (7.7) - (7.11) may now be written

$$\boldsymbol{M}_{ij} = m \int_L A_i^n A_j^n \mathrm{d}x \tag{7.14}$$

$$\boldsymbol{D}_{ij} = a_1 \int_L A_i^n (A_j^n)' \mathrm{d}x \tag{7.15}$$

$$\boldsymbol{K}_{ij}^a = \int_L (A_i^n)'(a_0 - f_t x)(A_j^n)' \mathrm{d}x \tag{7.16}$$

$$\boldsymbol{K}_{ij}^b = -f_t \int_L A_i^n (A_j^n)' \mathrm{d}x \tag{7.17}$$

$$\boldsymbol{F}_{ij} = \int_L A_i^n (F(\alpha) - X) \mathrm{d}x \tag{7.18}$$

The functions A_k^n are polynomials, thus the derivative, products and integrals may be found analytically.

Rather than a boundary condition another piece of cable may be attached to one of the boundaries. Requiring continuity a constraint force is introduced for the node common to both cable segments. This constraint force may be canceled by adding the rows in the matrices where it occurs, see Egeland and Gravdahl (2002). Then a new coupled equation system for both cable segments are formed, with matrices:

$$\boldsymbol{E} = \begin{bmatrix} e_{11}^{(1)} & \cdots & e_{1n}^{(1)} & & \\ & \ddots & & \mathbf{0} & \\ e_{n1}^{(1)} & \cdots & e_{nn}^{(1)} + e_{11}^{(2)} & \cdots & e_{1n}^{(2)} \\ & \mathbf{0} & & \ddots & \\ & & e_{n1}^{(2)} & \cdots & e_{nn}^{(2)} \end{bmatrix} \tag{7.19}$$

where superscripts denote cable segment and $\boldsymbol{E}$ and its entries may be any of the matrices $\boldsymbol{M}, \boldsymbol{D}, \boldsymbol{K}, \boldsymbol{F}$ in equation (7.5). This of course can be repeated any number of times. In the literature, such cable segments are known as elements and the described method is a special case of the *finite element method.*

Note that neither the order n of the Lagrange polynomial or the parameters of the cable segment need to be constant for all elements. In fact an element does not need to be a cable segment at all, but could be an attached mass like a buoy or a tow fish.

7.1.3 Implementation and Time Integration

The described method was implemented in MATLAB®, using the polynomial functions included in this package. Derivation and integration of polynomials were done analytically, while the polynomial products in equations (7.14) - (7.18) were found by convolution of coefficient vectors (Math Works Inc. 2000). The term $(a_0 - f_t x)$ is also a polynomial and is integrated analytically.

The forces included in the *generalized* force vector on the right side of equation 7.5 may be either of distributed or point type. Superscripts are used to distinguish the type, c for continuous force and p for point forces. The distributed forces are typically hydrodynamic and body forces, while the most common point force is the Neumann boundary condition, here implemented as a point force on the boundary node.

For a continuous force the integral

$$\boldsymbol{F^c}_{ij} = \int_L A_i^n F(\alpha)\mathrm{d}x \tag{7.20}$$

must be evaluated numerically. One way of doing this is to make the same approximation for the force as for the solution:

$$F(x,t) \simeq \hat{F}(x_0 + ph, t) \simeq \sum_k A_k^n(p) F_k \tag{7.21}$$

where F_k is the force evaluated in the nodes. Then

$$\boldsymbol{F^c} = \boldsymbol{L F_k} \tag{7.22}$$

where $\boldsymbol{F_k}$ is a vector of forces evaluated in the nodes, while $\boldsymbol{L}$ is an operator matrix with entries

$$\boldsymbol{L_{ij}} = \int_L A_i^n A_j^n \mathrm{d}x \tag{7.23}$$

In chapter 6 it was found that the hydrodynamic force depends on the angle between the cable axis and the incoming flow:

$$\alpha = f\left(U, \frac{\partial z}{\partial t}, \frac{\partial z}{\partial x}\right) \tag{7.24}$$

The time derivative (the velocity of the nodes) is available from the time integration procedure described below, while the space derivative was found by a central difference approximation.

Point forces can only be located in node points. They can be expressed by the Kronecker delta function:

$$F_i^p = F^p \delta(x - x_i) \tag{7.25}$$

where i denotes the node index and x_i is the position of the node. The variational form is:

$$\boldsymbol{F^p}_i = \int_L A_i^n F^p \delta(x - x_k)\mathrm{d}x = F_i^p \tag{7.26}$$

due to the properties of A_i^n and the Kronecker delta function.

An explicit variable step procedure was used for time integration, see software documentation entry on *ODE45* (Math Works Inc. 2000). Equation (7.5) must the be rewritten to a first order system:

$$\dot{\boldsymbol{x}} = \boldsymbol{A}\boldsymbol{x} + \boldsymbol{B} \tag{7.27}$$

where

$$\boldsymbol{x} = \begin{bmatrix} \boldsymbol{q} \\ \dot{\boldsymbol{q}} \end{bmatrix} \tag{7.28}$$

$$\boldsymbol{A} = \begin{bmatrix} \mathbf{0} & \boldsymbol{I} \\ \boldsymbol{M}^{-1}\boldsymbol{K} & \boldsymbol{M}^{-1}\boldsymbol{D} \end{bmatrix} \tag{7.29}$$

$$\boldsymbol{B} = \begin{bmatrix} \mathbf{0} \\ \boldsymbol{M}^{-1}\left(\boldsymbol{L}\boldsymbol{F}^{\boldsymbol{c}} + \boldsymbol{F}^{\boldsymbol{p}}\right) \end{bmatrix} \tag{7.30}$$

For Dirichlet boundary conditions, the appropriate rows in these matrices are replaced by known solutions on the boundary.

7.1.4 Convergence and consistency

The implemented code was tested on the sample problems in table 6.1 and compared to the analytic solutions in section 6.2. Only elements with $n = 2$ and $n = 3$ nodes were tested since higher order polynomials tended to be unstable. The amplitude were found for each period of the resulting time series and the value used for error calculation was the mean of 6 periods in the steady state portion of the time series. The mean is used since there is a small variation from period to period most probably due to sampling. The results for the *high tension case* are shown in figure 7.1 and for the *low tension case* in figure 7.2. The advantage of a higher order polynomial should be obvious, since the convergence is much faster for the second order polynomial. Note that particularly for frequencies close to eigenfrequency the error does not seem to converge exactly to zero. This is believed to be the result of a slight difference in the application of the aft boundary condition. For the FEM method a point force is applied as part of the dynamic equation on the last element, while in the analytic solution the condition is set directly on the dependent variable. Changing the downstream boundary condition to a fixed position reduces the error by an order of magnitude. The case of $\omega = 0.15$ rads^{-1} for the streamer section was also tested with 601 grid points (second order, 300 elements). The error was found to $(A_{FEM} - A_0)/A_0 = -4.7 \times 10^{-4}$, which is lower than the variation from period to period, and on level with the time integration tolerances. Here A_{FEM} is the result from time domain simulation and A_0 the analytic solution in the frequency domain.

7.1.5 Non-linear hydrodynamic force

In a time domain simulation any non-linear effect can be incorporated as long as the time integration routine is stable. In this case it means that all the non-linear terms in the hydrodynamic force discussed in chapter 2 can be included. The non-linear expressions for the normal part of

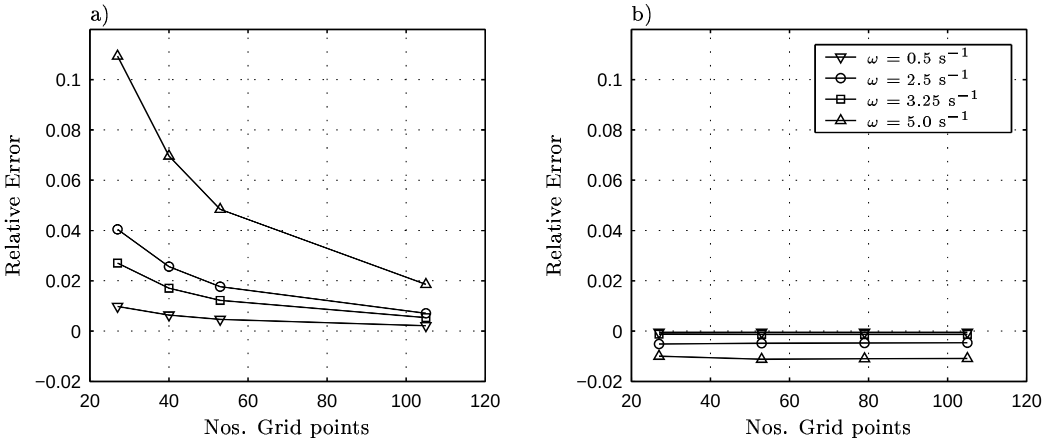

Figure 7.1: *Relative error in estimated amplitude and convergence of FEM for high tension cases: a) first order elements, b) second order elements. The error is given with respect to the analytic result in chapter 6.*

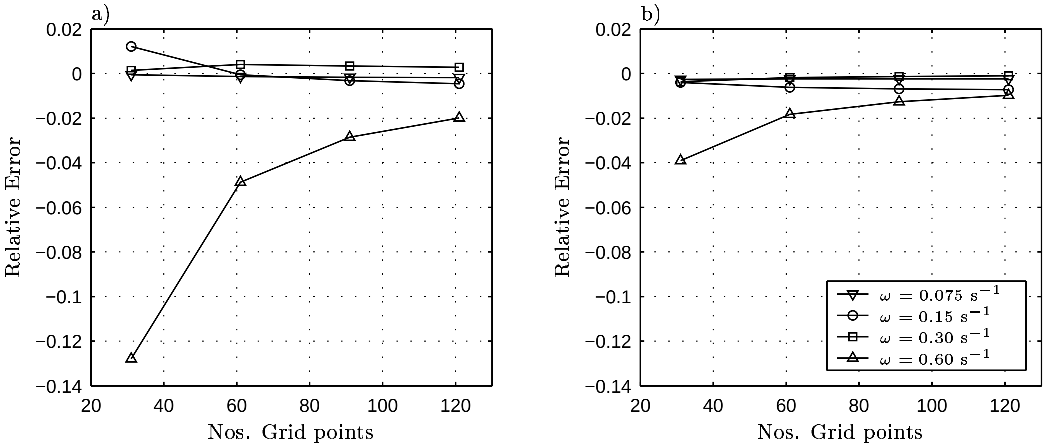

Figure 7.2: *Relative error in estimated amplitude and convergence of FEM for low tension case: a) first order elements, b) second order elements. The error is given with respect to the analytic result in chapter 6.*

hydrodynamic force then are:

$$F_{nv} = -C_n \, \frac{1}{2}\rho V^2 \, d \tag{7.31}$$

$$V^2 = \left(U^2 + \left(\frac{\partial z}{\partial t} \right)^2 \right) \tag{7.32}$$

$$\alpha = \arctan\left(\frac{1}{U} \frac{\partial z}{\partial t} \right) + \frac{\partial z}{\partial x} \tag{7.33}$$

$$C_n = f(\alpha) \left(C_{n1} \sin(\alpha) + C_{n2} \sin(\alpha) \left| \sin(\alpha) \right| \right) \tag{7.34}$$

Here the true and instantaneous angle of attack and inflow velocity are used for calculation of the force. The function $f(\alpha)$ is used to reduce the force coefficient for low angle of attack. It is defined as a scaled inverse tangent function

$$\begin{aligned} f(\alpha) &= \frac{1}{2} + \frac{1}{\pi}\arctan\left(k(\alpha-\alpha_0)\right) \\ k &= \frac{1}{\alpha_0}\tan\left(\pi\left(\frac{1}{2}-\frac{\pi C_F}{C_{n1}}\right)\right) \end{aligned} \tag{7.35}$$

An alternative would be to simply change expression for the force at $\alpha < \alpha_0$, but the use of a smooth function significantly reduces the simulation time. The importance of these corrections are indicated in figure 7.3. Part *a*) shows the reduction of force at very low inflow angles, part *b*) shows the relation between tow and relative velocity, and *c*) the relation between linearized and true expression for trigonometric functions. From figure 7.3 it can be concluded that using tow velocity rather than relative velocity underestimates the force, while the small angle approximation to the trigonometric function will overestimate it.

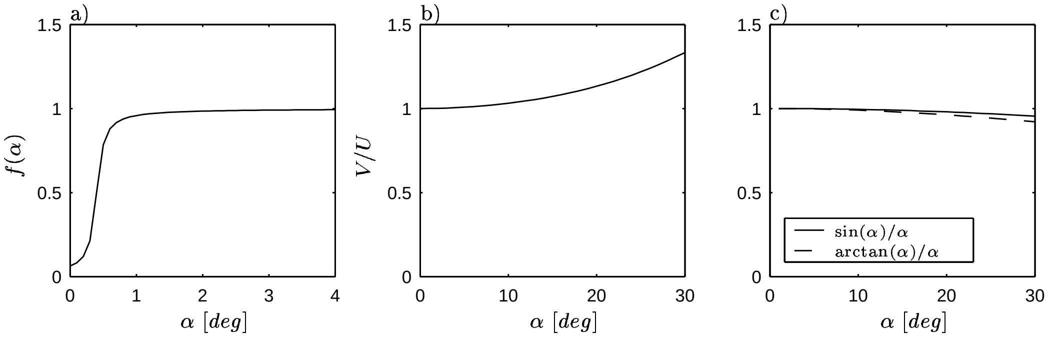

Figure 7.3: *Importance of non-linear terms: a) $f(\alpha)$ as in equation (7.35); b) $V/U = 1+tan^2(\alpha)$; c) Linearizion of trigonometric functions*

In chapter 6 the suggested set of parameters was:

$$\begin{aligned} C_a &= 0.8 \\ C_{n1} &= 0.08 \\ C_{n2} &= 1.0 \end{aligned} \tag{7.36}$$

The peak to peak amplitude for all tow speeds are given in figures 7.4 - 7.6, where the results in chapter 6 are included together with measurements. The improved results in the time simulation is a result of using the instantaneous angle of attack rather than the amplitude as in chapter 6. This includes the reduction of force for local angle of attack less than 1°, which results in better comparison with experiment both for low and high frequencies and in the transition region. As seen from the figures, the comparison with experimental data is now quite good, a fact that will be discussed further in the next section.

The dashed line in figure 7.4 is the result when $C_{n2} = 2.0$. This is the upper limit for the oscillating cylinder in chapter 4 at zero forward speed. It is included to illustrate that at

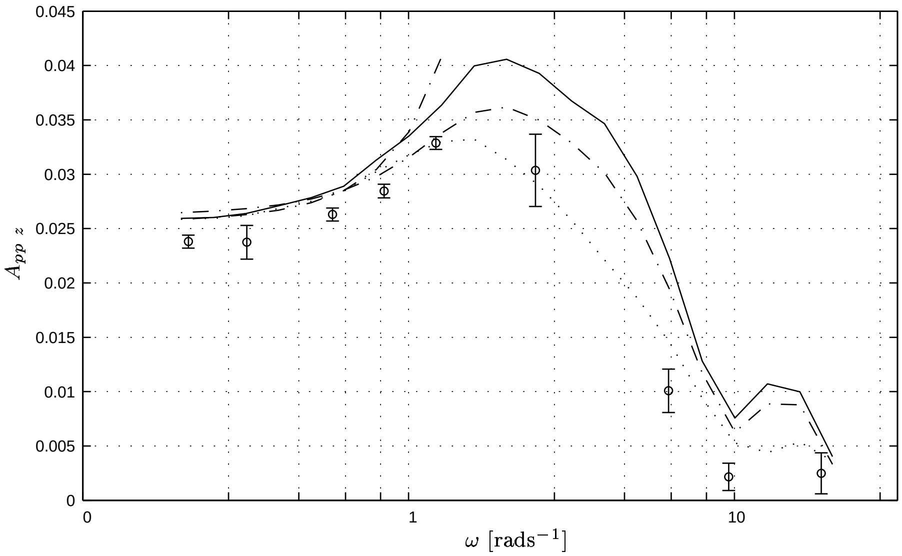

Figure 7.4: *Response amplitude for FEM model, tow speed $U = 0.5$ m/s : ○ Experiments (Bars represents 95% confidence); — FEM model results; -- Low speed modification of hydrodynamic coefficients; -·- Frequency domain results from chapter 6, models a) and h).*

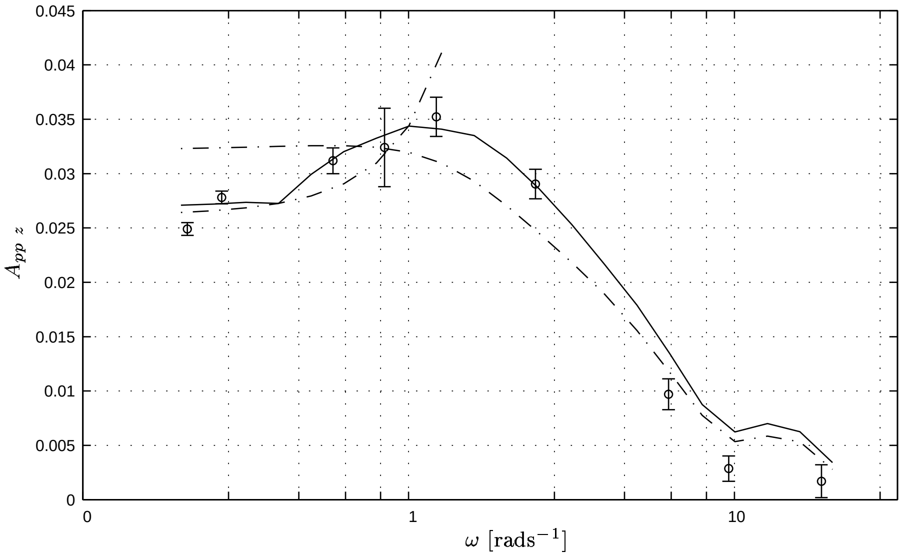

Figure 7.5: *Response amplitude for FEM model, tow speed $U = 1.5$ m/s : ○ Experiments (Bars represents 95% confidence); — FEM model results; -·- Frequency domain results from chapter 6, models a) and h).*

low forward speed, the KC number effects known from the pure cross flow case does become important.

The coefficients in equation (7.36) are based on the results from curve fitting of Morison's

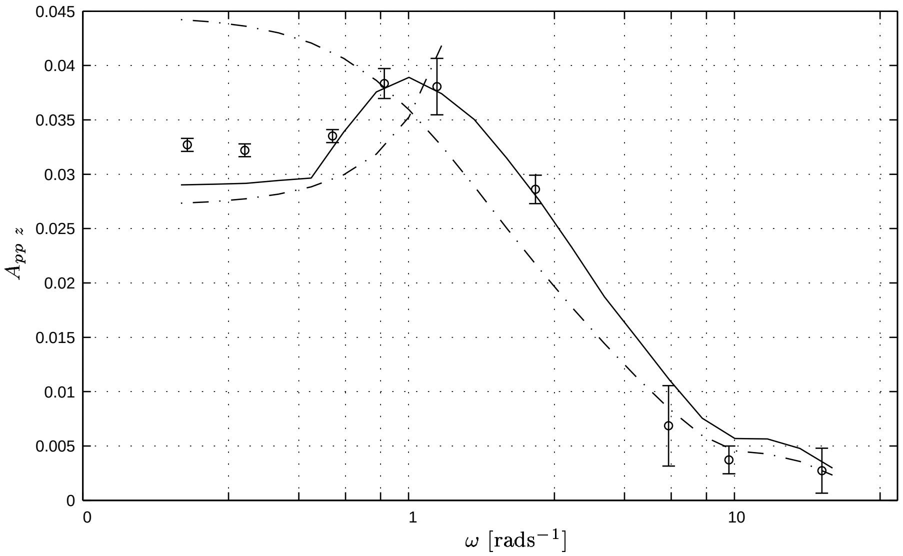

Figure 7.6: *Response amplitude for FEM model, tow speed $U = 2.5$ m/s : ○ Experiments (Bars represents 95% confidence); — FEM model results; -·- Frequency domain results from chapter 6, models a) and h).*

equation in chapter 4. It is probable that other combinations of C_a and C_{n2} may be equally suitable. The current model was tested with $C_a = 1$ and $C_{n2} = 1.3$, which gave a comparable answer, but these coefficient cannot be traced back to the other experiments.

7.1.6 Error estimate for hydrodynamic forces

The uncertainty in the simulation was in chapter 2 denoted e_{num}. Here it includes a conservative value for the parameter errors and structural damping from table 6.4 (e_{numa}) and the numeric uncertainty from figure 7.1 *b*) with 60 grid points (e_{numb}):

$$e^r_{num} = \sqrt{e^2_{numa} + e^2_{numb}} \tag{7.37}$$

where superscript r denotes a relative error. Linear interpolation is used between frequencies in table 6.4 for e_{numa}. The modeling error is the root square sum of the difference between calculated and measured value and the uncertainty in the simulation:

$$e_{mod} = \sqrt{\left(A^s_{pp} - A^m_{pp}\right)^2 + \left(e^r_{num} A^s_{pp}\right)^2} \tag{7.38}$$

where superscripts s and m denotes simulated and measured values respectively. The ratio of the modeling error and the measurement (experimental) error e_{mod}/e_{exp} are shown in figure 7.7. As expected from figure 7.4, the curve for $U = 0.5$ ms^{-1} is not impressive, and clearly indicates that improvement of the model is possible. For the high speeds, which is more interesting from the application to seismic cables, the modeling error is more acceptable. At least for intermediate frequencies the ratio is less than two. These frequencies corresponds to angles of attack mostly below 10°, see figure 6.6. For higher frequencies the estimate error is 2-3 times the measurement error and still within a reasonable accuracy. For the highest frequency the dynamic part of the tension becomes significant and the local angles of attack becomes high. In this region the numerical model is not expected to be valid, even if the error ratio is low. For low frequencies the modeling error is also larger than optimal. For these cases the measured value is based on a single oscillation in the time series, and the measurement only includes the bias errors. It is then a little optimistic to call this a 95% confidence interval, and the error of the estimate may still be acceptable.

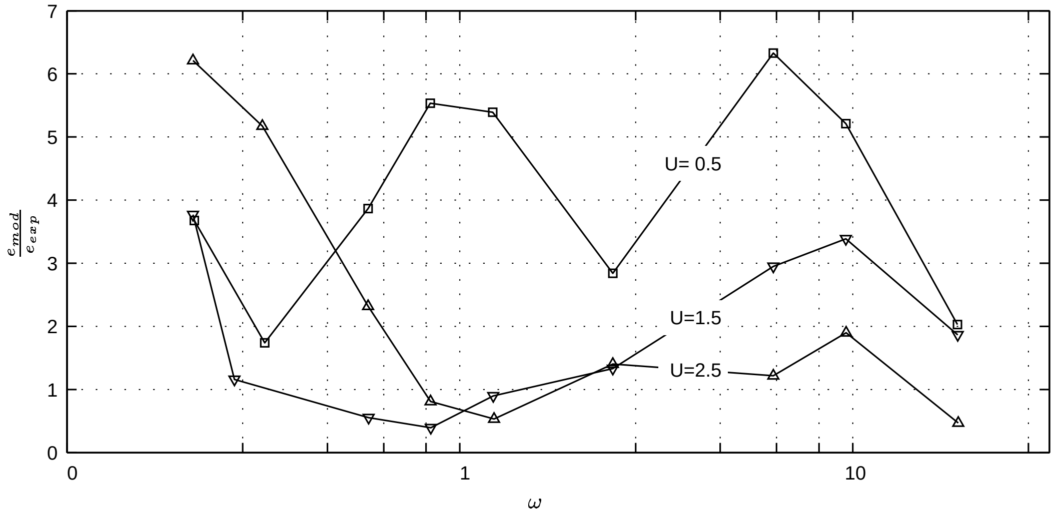

Figure 7.7: *Modeling error over measurement errors for peak to peak amplitude at x/L=0.77. Tow speed U in* ms^{-1}.

As a measure of the model error valid for all frequencies, the standard error of estimate can be found:

$$S_m = \sqrt{\frac{1}{N-1}\sum_{j=1}^{N}\left(\left(\frac{A^e_{pp\ j} - A^m_{pp\ j}}{A^m_{pp\ j}}\right)^2 + (e^r_{num\ j})^2\right)} \tag{7.39}$$

$$SEE^r = t\ S_m \tag{7.40}$$

here j indicates measured frequencies. The variation is taken over low and intermediate frequencies for each tow speed, and the factor t is given by student's t distribution. The result for the three velocities are given in table 7.1, indicating an error of less than 10% for the high tow speeds.

7.2 Results for a streamer section

In the remainder of this chapter, the normal response of a part of a real streamer will be discussed. Although similar to the low tension case described previously, all parameters are listed again in table 7.2. Note that the mass coefficient C_m is the structural mass of the cable.

Table 7.1: *95% Confidence interval for hydrodynamic forces in the simulation of the experiment.*

Tow speed (ms^{-1})	0.5	1.5	2.5
Standard error of estimate SEE^r	0.21	0.07	0.09

Table 7.2: *Parameters for streamer section.*

	symbol	value
Diameter [m]	d	0.07
Length [m]	L	300
Aft Tension [N]	T_a	1800
Aft Spring stiffness [N/m]	k_p	24
Tow Speed [ms^{-1}]	U	2.2
Tow depth [m]	h	8
Normal Force	equations (7.31) - (7.34)	
Mass coefficient	C_m	1
Added mass coefficient	C_a	0.8
Friction coefficient	C_F	0.0024
Normal force coefficients	C_{n1}	0.08
	C_{n2}	1.0

The convergence for forced motion of the tow point are shown in figure 7.8 for second order elements. Part *a*) shows the amplitude period by period while part *b*) is found the same way as above. The amplitude seems to converge after about 15 periods and 120 grid points gives an error of about 0.2%. This is taken as an acceptable trade off between accuracy and simulation time, considering the uncertainty in e.g. the hydrodynamic force.

In figure 7.9 the peak to peak response amplitude for the streamer section is given, for two input amplitudes. Compared to figure 6.3 *b*) the amplitude at higher frequencies are almost completely damped out, but note that for the low amplitude some motion is carried trough to the downstream end, even for high frequencies.

7.2.1 Adding weight

The streamer section described in table 7.2 is neutral in water. For a real streamer this may be difficult to achieve due to local variations in density of both the streamer and sea water. Mean shapes and amplitudes of oscillation for 0, 0.5, and 1% negative bouyancy are shown in figure 7.10. The curves for response amplitude seems to shift toward left, or lower frequencies, for increased weight. Also, the mean increases with frequency in the order of 20-30%, so decoupling of static and dynamic motion is questionable even for low frequencies when the tension in the cable is low. Note that the tension is not changed with added weight in the analysis, so tension variation due to a sagging cable is not included.

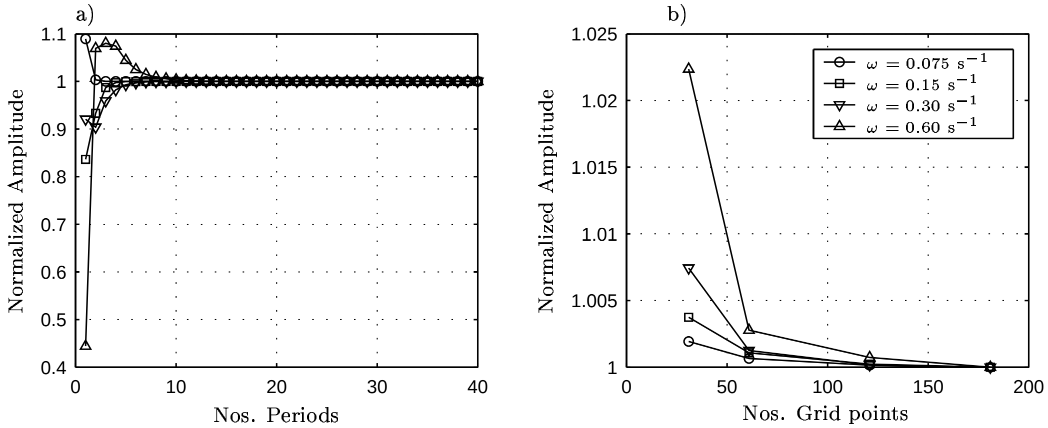

Figure 7.8: *Convergence of FEM for streamer section: a) Time, b) Grid. All results are normalized with last (assumed best) value.*

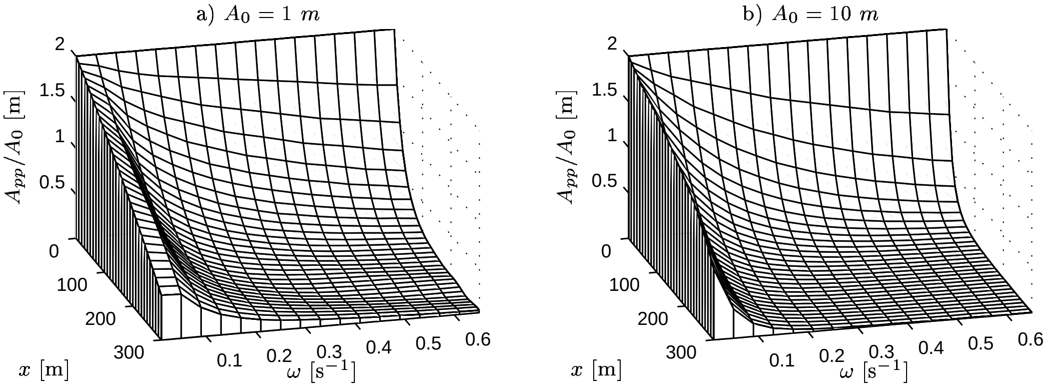

Figure 7.9: *Peak to peak response for streamer section. The section is oscillated with amplitude* A_0 *and frequency* ω *in the tow point.*

7.3 Wave induced motion of a streamer section

Any wave induced motion of a towed steamer is usually neglected due to the large distance between the wave frequency and the eigenfrequency of a typical streamer, e.g Triantafyllou and Chryssostomidis (1988) and Pedersen (1996). But high damping in the case of forced motion should correspond to high excitation forces in waves, so it seems worth the effort to do a more detailed study.

The effect of an incoming wave is included by modifying the velocity in the normal hydrodynamic forces. As for the buoyancy, the assumption of time invariant tension is questionable, since the particle velocity under a wave has a horizontal component which will modify the friction force along the cable. Also, this component will modify the angle and inflow velocity for the viscous hydrodynamic force. For the sake of consistency, only the normal, or in this case vertical, component of the wave motion will be included, both for potential and viscous parts of

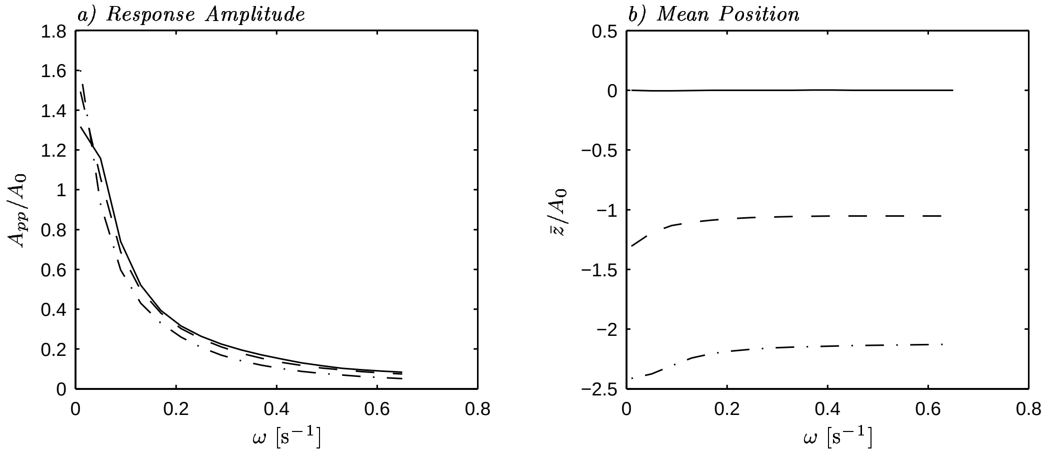

Figure 7.10: *Response amplitude at midspan for streamer section with non-zero buoyancy:* — $C_m = 1.00$*;* -- $C_m = 1.005$*;* -·- $C_m = 1.01$*.*

the hydrodynamic force. This is similar to using Morison's equation for a cylinder at rest, where wave induced velocity along the cylinder axis is neglected.

7.3.1 Regular waves

For a regular sinusoidal wave with period T propagating along an axis with angle β to the x axis the induced acceleration and velocities are (Faltinsen 1990, table 2.1):

$$\begin{aligned}
w_w &= \omega\zeta_a \mathrm{e}^{-kh}\cos\left(\omega_e t - k\cos(\beta)\,x\right) && (7.41)\\
\dot{w}_w &= -\omega^2\zeta_a \mathrm{e}^{-kh}\sin\left(\omega_e t - k\cos(\beta)\,x\right) && (7.42)\\
\zeta_a &= \text{Wave amplitude}\\
\omega &= \text{Wave frequency: } \frac{2\pi}{T}\\
\omega_e &= \text{Encounter frequency: } \omega + kU\cos(\beta)\\
k &= \text{Wave number: } \frac{\omega^2}{g}\\
h &= \text{Tow depth}
\end{aligned}$$

The effect of forward speed is accounted for in the *encounter frequency.* The velocities are calculated at the mean tow depth rather than at instantaneous position. For long waves and small amplitudes this should be reasonable.

The hydrodynamic forces depends on the relative velocity between the cable and the surrounding water. Even if the induced velocity under a wave might be of the order of the tow speed, the cable will normally move with the wave, so that the relative velocity and acceleration is small. For this reason the inertia part must be included, even if the ratio between cable diameter and wave length is small. Also, this means that the local angle of attack is small, so that a cross flow model of the hydrodynamic force would not perform well.

The viscous hydrodynamic forces are calculated by modifying the normal velocity term in equations (7.31) - (7.34) .

$$\begin{aligned} v_r &= \dot{z} - w_w && (7.43) \\ \alpha &= \arctan\left(\frac{v_r}{u_r}\right) + \frac{\partial z}{\partial x} && (7.44) \\ V^2 &= U^2 + v_r^2 && (7.45) \end{aligned}$$

For the inertia part of the hydrodynamic force, the slender body force given by equation (6.8) is modified by the relative velocity:

$$\begin{aligned} F_{np} &= -\left(\frac{\partial}{\partial t} + U\frac{\partial}{\partial x}\right) a\left(\dot{z} + Uz' - w_w\right) \\ &= -a\ddot{z} - a\frac{\partial}{\partial x}\left(2U\dot{z} + U^2 z'\right) + a\dot{w}_w + aUw_w' && (7.46) \\ w_w' &= k\omega\zeta_a \mathrm{e}^{-kh} \sin\left(\omega_e t - k\cos(\beta)\, x\right) && (7.47) \end{aligned}$$

Here the wave induced velocity normal to the cable is taken as the vertical component, due to the assumption of small perturbations of the cable position, see chapter 6. The first two terms in equation (7.46) are the same as in equation (6.8), while the last two are additional loads. In addition there is the *Froude-Kriloff* force (Faltinsen 1990):

$$F_{fk} = \rho\frac{\pi d^2}{4}\dot{w}_w \qquad (7.48)$$

The sum of the third term in equation (7.46) and equation (7.48) gives the inertia term in Morison's equation.

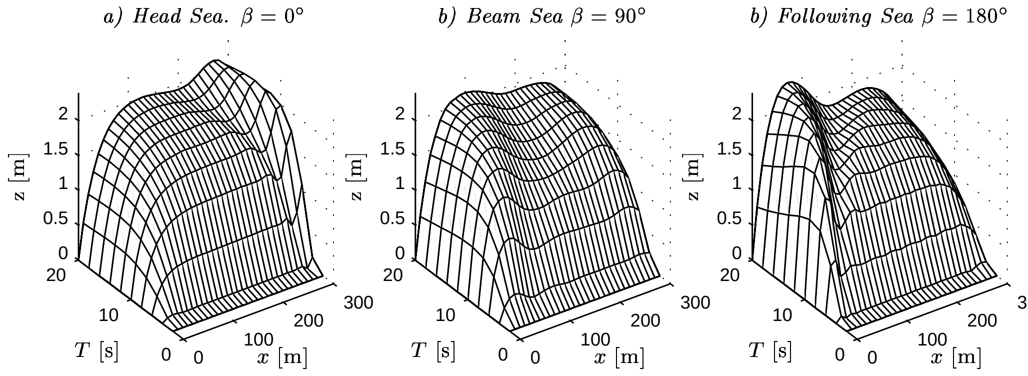
a) Head Sea. $\beta = 0°$ *b) Beam Sea $\beta = 90°$* *b) Following Sea $\beta = 180°$*

Figure 7.11: *Response of streamer section to regular waves with period T. Wave height is $H_w = 2$ m. The streamer is pinned in the tow point and supported by a spring in the aft end.*

Amplitudes of the normal response for head, beam and following sea are given in figure 7.11. The maximum value is highest for following sea, and least for head sea. This is expected since the response is increasing with wave period, and the encounter period is highest for following

Table 7.3: *Influence coefficients κ_i for streamer in head sea. Results refers to max amplitude. Wave height is 2 m.*

Index		Wave period:	$T_s = 10$ s	$T_s = 20$ s
1	Diameter	d	2	-0.56
2	Length	L	0	-0.00012
3	Tow depth	h	-0.035	-0.0075
4	Aft tension	T_a	0	0
5	Aft spring stiffness	k_p	-0.0021	-0.00023
6	Mass Coefficient	C_m	0.064	-0.034
7	Added mass coefficient	C_a	0.065	-0.012
8	Friction Coefficient	C_F	0.1	2.2
9	Normal Force Coefficients	C_{n1}	-0.99	-1.1
10		C_{n2}	-0.095	-0.026
11	Tow Speed	U	-0.054	-0.032
12	Wave height	H_w	0.45	0.47

sea. The location of the maximum response is toward the end for head sea and toward the tow point for following sea. For beam sea the peak is less profound. It is still located at the forward end, indicating that a fixed end returns more of the wave like motion of the cable than a free end.

7.3.2 Sensitivity and errors

The influence coefficients in table 7.3 are found the same way as in chapter 6, but refers to the maximum amplitude along the streamer. The simulations were done in head sea, but the results are similar for other directions.

As in chapter 6 the diameter is among the most important parameters. More interesting is the fact that the aft boundary condition has a very small influence, thus active control of the dynamic response may be hard to obtain. The response seems to be dominated by viscous forces rather than inertia, and it is the linear coefficients C_F and C_{n1} that are the most influential. The maximum response amplitude is higher than the wave amplitude, thus increasing the normal force coefficient decreases the response.

Error sources and estimated values are listed in table 7.4. The influence coefficient for tow speed can be used to make an estimate of the error from neglecting the horizontal component of the wave induced velocity. The amplitude of this velocity is u_w=0.9 ms^{-1}, and the value $u_w/U = 0.4$ is used for precision in table 7.4. Simulations with the horizontal component included in the viscous force confirmed the small error in the response amplitude, but gave a significant constant force at low periods. The influence coefficient for tow depth may be used to estimate the error from using mean position in force calculations. The max amplitude from figure 7.11 is $z_{max} = 1.2$ m, and $z_{max}/h = 0.006$ is used for precision. The effect of material damping is neglected in this analysis.

Force model error is taken from table 7.1 and numerical error from figure 7.2. The

Table 7.4: *Model errors for the streamer section in waves.*

	κ_i	τ_i	S_i	e_{ri}
Horizontal component of velocity	0.054	1	0.4	0.022
Mean position	0.035	1	0.15	0.005
Hydrodynamic force	from table 7.1			0.097
Numeric	from figure 7.2			0.02
Total (quadratic sum):				0.102

estimated error is then found to be 10.2% or about 1.5 diameters. This is not impressive but acceptable.

7.3.3 Irregular waves

To investigate the response of a streamer in a real sea condition, the expressions for velocity and acceleration in equation (7.41) and equation (7.42) are replaced with realizations of the Pierson-Moskowitz spectrum (Faltinsen 1990). The velocity and acceleration is calculated from the sum of 100 harmonic components with random phase. Results for head, beam and following sea are shown in figure 7.12. The standard deviation of the cable position from simulation of 30 min in two conditions are given in figure 7.12. The error level are assumed to be as for the regular wave, i.e about 10%.

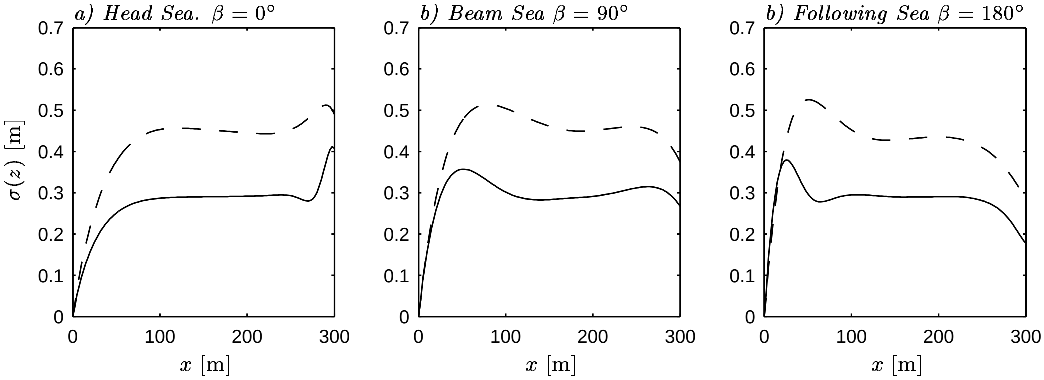

Figure 7.12: *Response of streamer section to irregular waves. Peak period:* — $T_p = 10$ *s;* -- $T_p = 20$ *s. Significant Wave height is* $H_s = 2$ *m. The streamer is pinned in the tow point and supported by a spring in the aft end.*

The condition $T_p = 10$ s and H_s roughly corresponds to sea state 4, which according to data in Faltinsen (1990, p. 30) is very common in both the North Atlantic and North Pacific. Cumulative probability plots of wave periods in the North Sea gives that the peak period is equal to or above 10 seconds for about 40% of the time, but very seldom as high as 20 s. It is therefore likely that the standard deviation of the cable due to wave induced motion is less than

0.4 m for realistic conditions. This seems to be small enough to accept the assumption that the streamer is not excited by the waves.

7.4 Depth control

Depth control devices are used to counter the errors in buoyancy of the streamer. The traditional concept is a wing where the angle of attack is controlled by a local controller, known as birds (Pedersen 1996). The device will contribute to the tension in the cable, since it will have drag components both from the device itself and due to lift. As before this will be neglected here and only the normal force is included.

Since the length of a bird is very small compared to the streamer it might be considered as a point load. The produced lift force is:

$$L = \frac{\rho}{2}\frac{\mathrm{d}C_L}{\mathrm{d}\alpha}\alpha_e U_e^2 S_b \tag{7.49}$$

where:

$\frac{\mathrm{d}C_L}{\mathrm{d}\alpha}$ – Lift curve slope

$\alpha_e = \alpha_c - \arctan\left(\frac{1}{U}\frac{\partial z}{\partial t} - w_w\right)$ -effective angle of attack

S_b – Planform area of the wing

The commanded angle of attack α_c is given by a PID controller:

$$\alpha_c = K_p(z - z_{ref}) + K_i \int (z - z_{ref})\, dt + K_d \frac{\partial z}{\partial t} \tag{7.50}$$

where:

K_p – Proportional gain

K_i – Integral gain

K_d – Derivative gain

z_{ref} – Reference setting

Other effects like dead-band, time lag, and dynamic effects on lift are not included. Parameters for the bird are from Pedersen (1996) and listed in table 7.5. The model is extended to $L = 600$ m with a bird placed at $x = 300$ m. The integral error at the bird is found by adding a term to the state space.

The standard deviation and mean with and without a depth control device in following irregular waves are given in figure 7.13. Also included is the case of a mounted wing with no active control, i.e a damping device. The streamer in this case has 0.5% negative bouyancy and the wave loading is a half hour realization of Pearson -Moskowitz spectrum with $T_0 = 10$ s and $H_s = 2$ m. The wave train is the same for all three cases.

At the position of the bird, the mean is zero and the motion is reduced compared to the cases of no and passive bird. But the active control induces motion in it's vicinity so the reduction in maximum motion along the streamer is limited. A passive bird at zero angle has little or no effect on either mean position or motion of the streamer. In this case no optimization of the bird controller is done, see Türkyilmaz (2003) for a discussion on control algorithms.

Table 7.5: *Parameters for a depth control device.*

Planform area [m]	S_b	0.09
Lift Curve slope [N/rad]	$\frac{\mathrm{d}C_L}{\mathrm{d}\alpha}$	2.5
Proportional gain [deg/m]	K_p	2.4
Integral gain [deg]	K_i	0.09
Derivative gain [deg s/m]	K_d	0

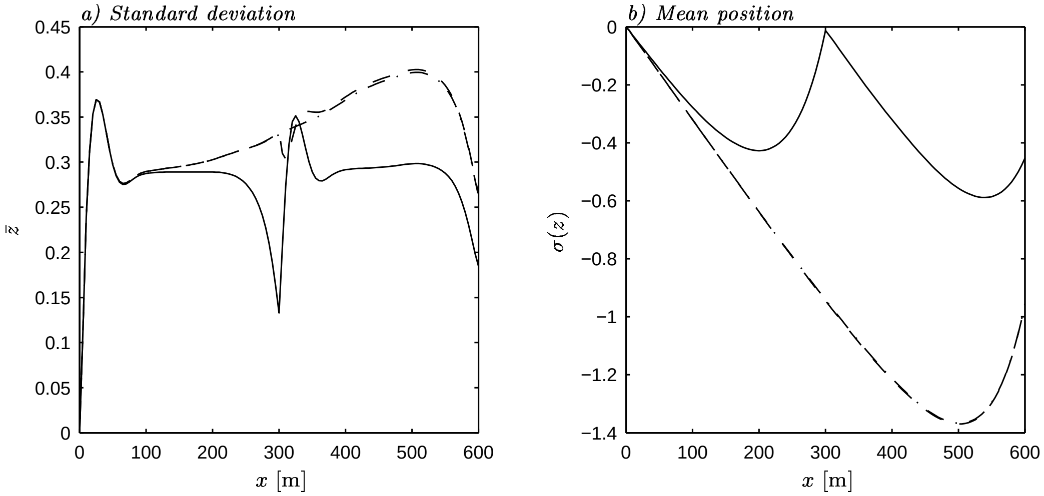

Figure 7.13: *Effect of bird on a streamer section in following irregular waves. : — PI controlled bird; -- Passive bird; -·- No bird. The bird is placed at x=300 m.*

7.4.1 Quasi-static model of a streamer

If motion due to waves and only low frequency motion is considered, a quasi-static cable model between the birds may be an option. The idea is based on a suggestion for further work in Pedersen (1996), an was developed in cooperation with Line Aune, M.Sc. Implementation and application of the model can be found in Aune (2003).

Consider the bird briefly described above. The forces and coordinates for such a bird are shown in figure figure 7.14. Her η describes the normal direction and ξ the tangent direction.

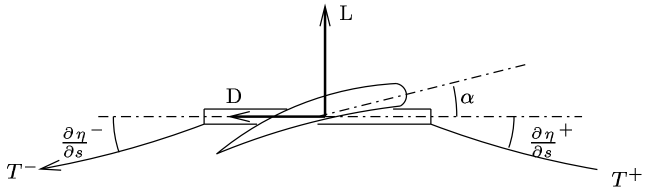

Figure 7.14: *Forces on a depth control device (bird)*

The normal direction is drawn in the vertical direction, but might just as well been the horizontal. Assuming low frequencies, the inertia forces are neglected and the equilibrium of the bird gives (2 DOF and small $\frac{\partial \eta}{\partial s}$):

$$\begin{aligned} 0 = &\quad D - T^- + T^+ && (7.51) \\ 0 = &\quad L - T^- \frac{\partial \eta}{\partial s}^- + T^+ \frac{\partial \eta}{\partial s}^+ && (7.52) \\ & && (7.53) \end{aligned}$$

Where m and a are the mass and added mass of the bird. The produced lift force is:

$$L = \frac{\rho}{2} \frac{\mathrm{d}C_L}{\mathrm{d}\alpha} \alpha_e u^2 A \tag{7.54}$$

$\frac{\mathrm{d}C_L}{\mathrm{d}\alpha}$ – lift curve slope

$\alpha_e = \alpha_0 + \alpha_c - \frac{\dot{\eta}}{u}$, effective angle of attack

α_0 - reference angle

α_c - commanded angle (controller angle)

A – planform area of the foil

u – perturbed velocity

This can be linearized to:

$$L \approx \frac{\rho}{2} \frac{\mathrm{d}C_L}{\mathrm{d}\alpha} A \left(\alpha_0 + \alpha_c\right) U^2 - \frac{\rho}{2} \frac{\mathrm{d}C_L}{\mathrm{d}\alpha} A \dot{\eta} U \tag{7.55}$$

The appendage drag of the bird consist of induced drag and friction forces on the wing (and body, in the case of a clamped on device).

$$D_i = \frac{\rho}{2} A_w \left(C_f + C_{Di}\right) u^2 \tag{7.56}$$

A_w – vetted area

C_f – skin friction coefficient

C_{Di} – induced drag coefficient

From this and the expressions for tension in chapter 6, the tension at all locations in the streamers can be calculated. The unknowns in equation (7.52) are then the normal velocity of the bird and the derivatives of the cable position. Assuming that the position of all birds are known, the derivatives are found from the equations for static shape in chapter 6. Due to the low velocities, linear expressions for hydrodynamic forces may be applied.

The transverse velocity of the bird can then be expressed as a function of the current position of the neighbor birds, current tow speed and current control input to the bird. Finding this for all birds and then integrate these velocities in time, a new position of the birds are established, and the procedure can be repeated. Inputs are motion or force at the forward and aft end of the streamer. Motion in both transverse directions are decoupled, so extension to 3-D is trivial. It probably also can be extended to cases with large deflections, alternatively with numerical solution of the static shape of the cable between the birds and the non-linear version of equation (7.52).

CHAPTER 8

Conclusion and further work

In the introduction it was stated that an important difficulty in modeling a seismic system is the uncertainty of the hydrodynamic forces on a cylinder in near axial flow, and in the previous chapters much effort have been put into improved models for these forces. But also the effective numeric simulation of the PDE describing the motion of a cable is a challenge, as indicated by the use of higher order elements in the Finite Element Method.

8.1 Hydrodynamic force model

The hydrodynamic forces in near axial flow are divided in a potential part that is modeled by the slender body approximation, and a viscous part that is written in a 'Lift Coefficient' form. The lift coefficient is expanded in a second order series in the angle of attack α, the angle between the cylinder axis and the incoming flow.

Experiments in chapter 3 showed the importance of the inflow condition to the normal forces on a cylinder at stationary angles. In cases where the vortices initially formed at the nose were symmetric, the results found in literature were more or less recovered. But in cases where the initial vortex pair were asymmetric, the normal force was found to be linear with the angle of attack for small angles, and not quadratic as expected. For larger angles it was indicated that the cross flow principle may be used, but a change from laminar to turbulent flow in the cylinder boundary layer due to the longitudinal component of the flow does affect the coefficient to use in the equations.

For an oscillating cylinder or cable the axial flow diminish the memory effect normally found for cylinders oscillating normal to their axis, i.e in cross flow. The KC number is therefore not an important parameter when α is less than 10-15°. The second order term in the normal force coefficient expansion seems to be a little higher than expected from drag of a cylinder in cross flow, while the added mass coefficient is a little low. The linear term found in the stationary case is also found in this case. For angles of attack below 0.5° separation is limited and the linear term should be replaced by the friction coefficient.

The improved model of the hydrodynamic force is given in section 7.1.5 where it is implemented in a time domain solution.

The values of the coefficients are based on experiments, and extensive error analysis of the experimental results were performed. The analysis includes both precision and bias uncertainty where bias uncertainty was defined as uncertainties not covered when repeating the experiment. Even for the case of towing a rigid cylinder, where the experiment was repeated six times, this bias uncertainty was estimated to contribute 10-15% of the total error. Error and sensitivity analysis of the numeric models again confirmed that the main problem is modeling the hydrodynamic force. For the flexible cable in near axial flow the error of the hydrodynamic force model is estimated to 10% for appropriate angles of attack. This includes realistic tow speeds and oscillating frequencies from .1 to 10 times the dry eigenfrequency of the cable.

The missing part on this topic is a good explanation for the high linear term. It seems to be connected to asymmetrical vortex shedding from the cylinder, and might be a 3-D phenomena. For further investigation the first step should be to try to reproduce the results in chapter 3 in a CFD calculation. Visualization and flow field velocity measurement around the cylinder with triggered asymmetric shedding also an interesting approach, either in towing tanks or in water or wind tunnels.

8.2 Simulation of a towed system

The linear equation of motion of a flexible cylinder has been developed in detail and possible solution strategies discussed. For realistic cases it seems that a numeric approximation is necessary, preferably in the time domain. A time domain finite element scheme was developed (chapter 7) valid for small oscillation amplitudes and near neutral buoyancy. Second order finite elements were found essential in order to obtain convergence of the simulations.

Applying the FEM model to a streamer section in chapter 7 it was found that the boundaries had little effect on the dynamic response for large areas of the streamer. Active control like birds are then effective in reducing the static deviation of cable position, but have little effect in damping the dynamic motion. For modeling it was found that the most sensitive parameters are the diameter of the cable and the coefficients in hydrodynamic model, including the friction coefficient of longitudinal flow.

At the onset of this work the goal was to model the complete system of ship, lead-in and streamers with control devices. Obviously, this was not achieved and development of such systems is definitely in the further work category. To simulate maneuvering and special operation of the full system an effective three dimensional model of a cable that allows high deformation is necessary. The extension of a FEM model to three dimensions is of course an alternative, but the resulting system of equations tends to be mathematically stiff resulting in slow integration in time. A promising alternative is to describe the cable by integration of Euler angles along its length. When torsion of the cable is neglected and it is assumed inextensible, the cable can in this way be described by two parameters. This reduces the system of equations to two, rather than three plus a compatibility relation normally necessary. The simplest way to facilitate this seems to be by a Lagrangian approach and the use of d'Alemberts principle, an alternative way to write the equations of motion.

References

AAMO, O. AND T. FOSSEN (2000). Finite element modelling of mooring lines. *mathematics and computers in simulation 53*, 415–422.

ABLOW, C. AND S. SCHECHTER (1983). Numerical simulation of undersea cable dynamics. *Ocean Engineering 10*(3), 443–457.

ABRAMOWITZ, M. AND A. STEGUN, I (Eds.) (1965). *Handbook of mathematical functions.* Dover Publications Inc.

AUNE, L. (2003). Modeling, simulation and control of towed seismic streamer cables in vertical and horizontal direction. Master's thesis, Norwegian University of Science and Technology.

BEARMAN, P., J. GRAHAM, AND E. OBASAJU (1984). A model equation for the transverse forces on cylinders in oscillatory flows. *Applied Ocean Research 6*(3), 166–172.

BERGAN, P., P. LARSEN, AND E. MOLLESTAD (1986). *Svingning av konstruksjoner* (Second ed.). Tapir. In norwegian.

BHATTACHARYYA, S., C. VENDHAN, AND K. SUDARSAN (2000). Finite elemnt method for hydroelastic instability of underwater towed cylindrical structures. *Journal of Sound and Vibration 237*(1), 119–143.

BLEVINS, R. D. (1992). *Applied Fluid Dynamics Handbook.* Krieger Publishing Company.

BRYSON, A. (1959). symmetric vortex separation on circular cylinders and cones. *Journal of Applied Mechanics*, 643–648.

CASARELLA, M. J. AND M. PARSONS (1970). Cable systems under hydrodynamic loading. *Marine Technology Society journal 4*(4), 27–44.

CHAKRABARTI, S. (1987). *Hydrodynamics of Offshore Structures.* Computational Mechanics Publications, Springer Verlag.

COLEMAN, H. AND W. STEELE (1989). *Experimentation and Uncertainty Analysis for Engineers.* Jon Wiley and Sons.

Comsol AB (2000). *FEMLAB User's Guide and Introduction, version 2.0.* Stockholm, Sweden: Comsol AB.

DOWLING, A. P. (1988). The dynamics of flexible slender cylinders. part 1: Neutrally buoyant elements. *Journal of Fluid Mechanics 187*, 507–533.

EGELAND, O. AND J. GRAVDAHL (2002). *Modeling and simulation for automatic control.* Marine Cybernetics.

ERSDAL, S. AND O. FALTINSEN (2002, June). Dynamics of towed cables with active controls. In *Proceedings of the International Offshore Mechanics and Arctic Engineering Symposium 21st.*

FALTINSEN, O. M. (1990). *Sea Loads on Ships and Offshore Structures.* Cambridge University Press.

FALTINSEN, O. M. (2000). Single cylinder current loads. Lecture notes.

FALTINSEN, O. M. (2004). Hydrodynamics of high-speed marine vehicles. To be published by Cambridge University Press.

HEENAN, A. AND J. MORRISON (2002). Turbulent boundary layers on axially inclined cylinders. part 1. surface-pressure/velocity correlations. *Experiments in Fluids 32*, 547–557.

HOERNER, S. AND H. BORST (1985). *Fluid-Dynamic Lift.* Published by the Author.

HOVER, F. S. (1997). Simulation of stiff massless tethers. *Ocean Engineering 24*(8), 765–783.

HOVER, F. S., M. GROSENBAUGH, AND M. TRIANTAFYLLOU (1994). Calculation of dynamic motions and tensions in towed underwater cables. *IEEE Journal of Ocean Engineering 19*(3), 765–783.

International Towing Tank Conference (1990). *Report of the Panel on Validation Procedures.* International Towing Tank Conference. 19'th.

JORGENSEN, L. AND E. PERKINS (1958). Investigation of some wake vortex characteristics of an inclined ogive cylinder body at mach number 2. Report 1371, NACA.

KENNEDY, R. (1987). Forced vibration of a thin flexible cylinder in viscous flow. *Journal of Fluid Mechanics 115*, 189–201.

KOUMOUTSAKOS, P. AND A. LEONARD (1995). High-resolution simulations of the flow around an impulsively started cylinder using vortex methods. *Journal of Fluid Mechanics 296*, 1–38.

KREYSZIG, E. (1988). *Advanced Engineering Mathematics* (6 ed.). Jon Wiley and Sons.

LIGHTHILL, M. (1960). Note on the swimming of slender fish. *Journal of Fluid Mechanics 9*, 305–317.

LOPES, J.-L., M. PAIDOUSSIS, AND C. SEMLER (2002). Linear and nonlinear dynamics of cantilevered cylinders in axial flow. part 2: The equations of motion. *Journal of Fluids and Structures 16*(6), 715–732.

LUEPTOW, R. AND J. HARITONIDIS (1987). The structure of the turbulent boundary layer on a cylinder in axial flow. *Physics of Fluids 30*(10), 2993–3005.

MARSHALL, J. (2003). Wake dynamics of a yawed cylinder. *Journal of Fluids Engineering 125*, 97–103.

Math Works Inc. (2000). *Using Matlab, version 6.* Math Works Inc.

NEWMAN, J. (1977). *Marine Hydrodynamics.* MIT press.

PAIDOUSSIS, M. (1966). Dynamics of flexible slender cylinders in axial flow. part 1: Theory. *Journal of Fluid Dynamics 26*, 717–736.

PAIDOUSSIS, M. (1973). Dynamics of cylindrical structures subjected to axial flow. *Journal of Sound and Vibrations 204*, 835–840.

PAIDOUSSIS, M., E. GRINEVICH, D. ADAMOVIC, AND C. SEMLER (2002). Linear and nonlinear dynamics of cantilevered cylinders in axial flow. part 1: Physical dynamics. *Journal of Fluids and Structures 16*(6), 691–713.

PEDERSEN, E. (1996). *A Nautical Study of Towed Marine Seismic Streamer Cable Configurations.* Ph. D. thesis, Norwegian University of Science and Technology.

PEDERSEN, E. AND A. SØRENSEN (2001). Modeling and control of towed marine seismic streamer cables. In *IFAC*.

RAMBERG, S. (1983). The effects of yaw and finite length upon the vortex wakes of stationary and vibrating circular cylinders. *Journal of Fluid Mechanics 128*, 81–107.

SANDERS, J. (1982). Three-dimensional dynamic analysis of a towed system. *Ocean Engineering 9*(5), 483–499.

SARPKAYA, T. (1966). separated flow about lifting bodies and impulsive flow about cylinders. *AIAA journal*, 414–420.

SARPKAYA, T. AND M. ISAACSON (1981). *Mechanics of Wave Forces on Offshore Structures.* Van Nostrand Reinhold Company.

SARPKAYA, T., T. RAINES, AND D. TRYTTEN (1982, May). Wave forces on inclined smooth and rough circular cylinders. In *Fourteenth annual Offshore Technology Conference*.

SCHLICHTING, H. (1979). *Boundary-Layer Theory* (Seventh ed.). McGraw-Hill.

SEMLER, C., J.-L. LOPES, N. AUGU, AND M. PAIDOUSSSIS (2002). Linear and nonlinear dynamics of cantilevered cylinders in axial flow. part 2: The equations of motion. *Journal of Fluids and Structures 16*(6), 715–732.

SPIEGEL, M. (1968). *Mathematical Handbook of Formulas and Tables.* Schaum's Outline Series. McGraw-Hill.

TAYLOR, G. (1952). Analysis of the swimming of long and narrow animals. *Proceedings Royal Society of London 214*, 158–183.

TRAUB, L. AND O. REDINIOTIS (2003). Analytic prediction of surface pressures over a hemisphere-cylinder at incidence. *Journal of Aircraft 40*(4), 645–652.

TRIANTAFYLLOU, G. AND C. CHRYSSOSTOMIDIS (1988). The dynamics of towed arrays. In *Proceedings of the International Offshore Mechanics and Arctic Engineering Symposium 7th*.

TÜRKYILMAZ, Y. (2003). *Modeling and Control of Towed Seismic Cables.* Ph. D. thesis, Norwegian University of Science and Technology.

VAZ, M.A.AND PATEL, M. AND J. WITZ (1997). Three-dimensional transient behavior of towed marine cables. *Journal of Ship Research 41*(1), 45–56.

VERLY, R. (1982). A simple model of vortex induced forces in waves and oscillating currents. *Applied Ocean Research 4*(2), 117–120.

WHITE, F. (1972). An analysis of axisymmetric turbulent flow past a long cylinder. *Journal of Basic Engineering 94*, 200–206.

WINGET, J. AND R. HUSTON (1976). Cable dynamics, a finite segment approach. *Computers and Structures 6*, 475–480.

ZILLIAC, G., D. DEGANI, AND M. TOBAK (1991). Asymmetric vorticies on a slender body of revolution. *AIAA Journal 29*(5), 667–675.

Appendix A

Laboratories at NTNU/MARINTEK

A.1 Towing Tanks

Figure A.1 show the towing tank facilities at NTNU/MARINTEK. The main data are tabulated in figure A.2. The facilities also includes a wave maker and an optical position measurement system.

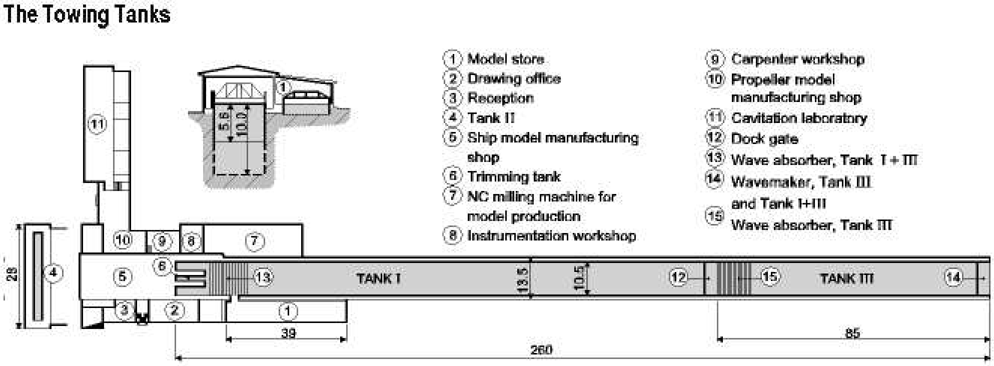

Figure A.1: Towing Tanks at NTNU/MARINTEK

A.2 MCLab

Marine Cybernetics Laboratory (MCLab) is an experimental laboratory for testing of ships, rigs, underwater vehicles and propulsion systems. Main dimensions are given in figure A.3. The carriage is described in figure A.4.

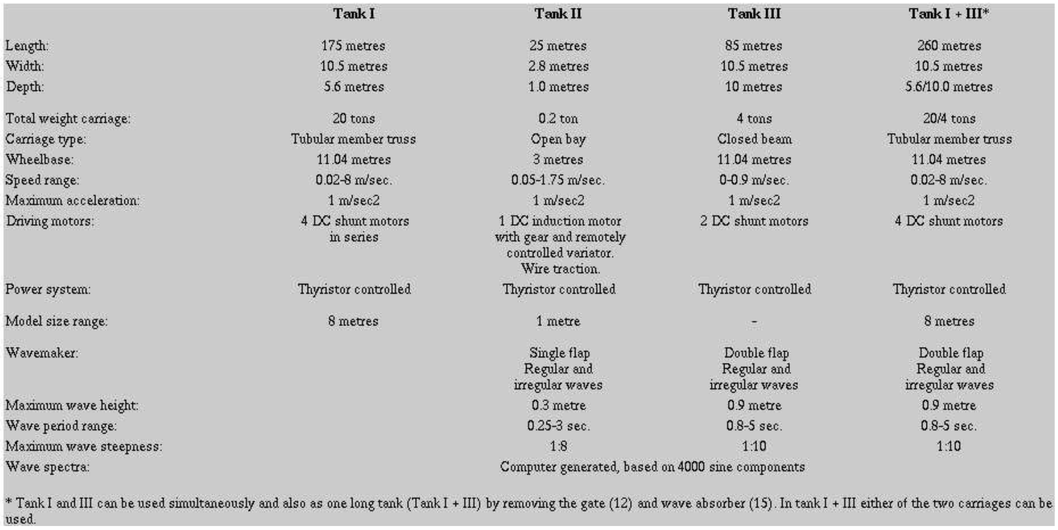

	Tank I	**Tank II**	**Tank III**	**Tank I + III***
Length:	175 metres	25 metres	85 metres	260 metres
Width:	10.5 metres	2.8 metres	10.5 metres	10.5 metres
Depth:	5.6 metres	1.0 metres	10 metres	5.6/10.0 metres
Total weight carriage:	20 tons	0.2 ton	4 tons	20/4 tons
Carriage type:	Tubular member truss	Open bay	Closed beam	Tubular member truss
Wheelbase:	11.04 metres	3 metres	11.04 metres	11.04 metres
Speed range:	0.02-8 m/sec.	0.05-1.75 m/sec.	0-0.9 m/sec.	0.02-8 m/sec.
Maximum acceleration:	1 m/sec2	1 m/sec2	1 m/sec2	1 m/sec2
Driving motors:	4 DC shunt motors in series	1 DC induction motor with gear and remotely controlled variator. Wire traction.	2 DC shunt motors	4 DC shunt motors
Power system:	Thyristor controlled	Thyristor controlled	Thyristor controlled	Thyristor controlled
Model size range:	8 metres	1 metre	-	8 metres
Wavemaker:		Single flap Regular and irregular waves	Double flap Regular and irregular waves	Double flap Regular and irregular waves
Maximum wave height:		0.3 metre	0.9 metre	0.9 metre
Wave period range:		0.25-3 sec.	0.8-5 sec.	0.8-5 sec.
Maximum wave steepness:		1:8	1:10	1:10
Wave spectra:		Computer generated, based on 4000 sine components		

* Tank I and III can be used simultaneously and also as one long tank (Tank I + III) by removing the gate (12) and wave absorber (15). In tank I + III either of the two carriages can be used.

Figure A.2: Main parameters for the Towing Tanks at NTNU/MARINTEK

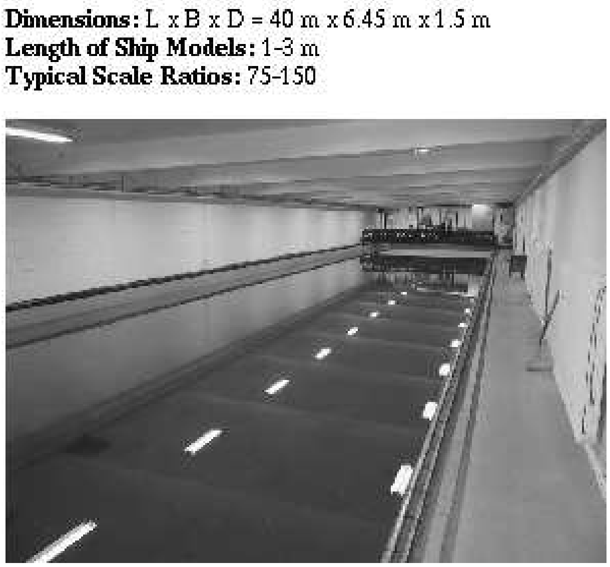

Dimensions: L x B x D = 40 m x 6.45 m x 1.5 m
Length of Ship Models: 1-3 m
Typical Scale Ratios: 75-150

Figure A.3: Marine Cybernetics Laboratory at NTNU/MARINTEK

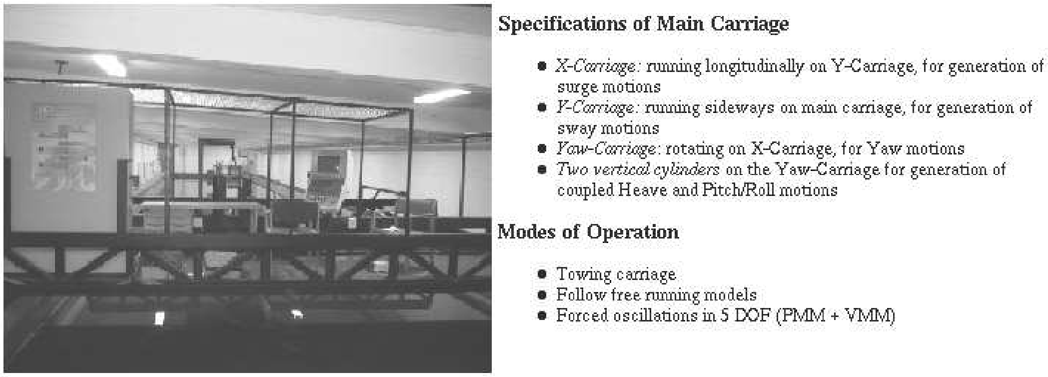

Specifications of Main Carriage

- *X-Carriage:* running longitudinally on Y-Carriage, for generation of surge motions
- *Y-Carriage:* running sideways on main carriage, for generation of sway motions
- *Yaw-Carriage:* rotating on X-Carriage, for Yaw motions
- *Two vertical cylinders* on the Yaw-Carriage for generation of coupled Heave and Pitch/Roll motions

Modes of Operation

- Towing carriage
- Follow free running models
- Forced oscillations in 5 DOF (PMM + VMM)

Figure A.4: Main parameters for the MCLab carriage

Appendix B

Tabulated results from experiments

The coordinate systems are given in the chapters describing the experiments. For the constant yaw angles in table B.1rcCny25 the in-line direction is the y-direction, thus C_{n2} dexibes the in-line, or normal, force coefficent and C_{n3} describes the out of plane, or bi-normal, force. C_{n5} and C_{n6} are pitch and yaw moments, respectively. For rotation in pitch, table B.5rcCnp15 the z-direction is inline. This is the case for all the oscillation results too, both rigid and flexible.

Table B.1: *Force coefficients for rigid cylinder and constant yaw angle, U=1.0 m/s*

α	C_n1	e_1	C_n2	e_2	C_n3	e_3	C_n4	e_4
-2	-0.0016	0.001	-0.0023	0.0027	0.00072	0.0036	0.00011	0.00087
-1	-0.00055	0.00026	0.00044	0.0021	0.0018	0.0037	-9.9e-005	0.00024
0	0	0	0.0019	0.0022	0.0016	0.0038	0	7.9e-005
1	0.0023	0.00023	0.00087	0.0024	0.0015	0.004	7e-005	0.0006
2	0.0034	0.00042	-0.0017	0.0032	0.0013	0.0031	-0.00015	0.00029
3	0.0046	0.00053	-0.0037	0.0033	0.0012	0.0024	-8.6e-005	0.00032
4	0.0058	0.00096	-0.0053	0.0036	0.0013	0.0025	-0.00028	0.00073
6	0.0097	0.0018	-0.0074	0.0028	0.00083	0.0064	0.00019	0.00075
8	0.016	0.0015	-0.0083	0.0029	0.00065	0.008	0.00086	0.00077
10	0.03	0.004	-0.0074	0.0035	-0.00011	0.011	0.0021	0.00095
12	0.054	0.005	0.0018	0.0027	0.0021	0.015	0.0035	0.0023
16	0.097	0.0018	0.0025	0.0024	0.0019	0.0081	0.0065	0.0032
20	0.17	0.0049	0.018	0.0021	0.0042	0.029	0.0085	0.0074
25	0.25	0.0067	0.013	0.0073	0.0069	0.025	0.011	0.012
30	0.32	0.0053	0.016	0.014	0.0067	0.037	0.012	0.017

Table B.2: *Force coefficients for rigid cylinder and constant yaw angle, U=1.5 m/s*

α	C_n1	e_1	C_n2	e_2	C_n3	e_3	C_n4	e_4
-2	-0.0024	0.00054	-0.0036	0.0022	0.00056	0.0029	3.4e-005	0.0011
-1	-0.00075	0.00021	0.00057	0.0021	0.00081	0.0033	-6.2e-005	0.00039
0	0	0	0.0019	0.0022	0.00091	0.0034	0	3e-005
1	0.0021	0.00027	0.00094	0.0025	0.00088	0.0032	-0.00013	0.00054
2	0.0033	0.00061	-0.0017	0.0032	0.00072	0.0028	-0.00024	0.00028
3	0.0044	0.00045	-0.0041	0.0035	0.00079	0.0021	-0.00013	0.00022
4	0.0058	0.00069	-0.0057	0.0034	0.00087	0.0027	-0.00022	0.00064
6	0.0098	0.0013	-0.0076	0.0028	0.0012	0.0076	0.00049	0.00053
8	0.016	0.002	-0.0089	0.0023	0.00036	0.0092	0.0007	0.00051
10	0.024	0.0022	-0.0083	0.0024	0.0015	0.013	0.0013	0.00088
12	0.034	0.0039	-0.0097	0.0022	0.0015	0.014	0.002	0.0016
16	0.091	0.0041	0.00053	0.0022	0.0018	0.011	0.0062	0.0057
20	0.16	0.0035	0.019	0.0051	0.0011	0.03	0.0099	0.011
25	0.25	0.0048	0.0089	0.0023	-0.0006	0.028	0.013	0.0095
30	0.31	0.0093	0.011	0.0036	0.0022	0.055	0.015	0.011

Table B.3: *Force coefficients for rigid cylinder and constant yaw angle, U=2.0 m/s*

α	C_n1	e_1	C_n2	e_2	C_n3	e_3	C_n4	e_4
-2	-0.0025	0.00054	-0.0044	0.0024	2.3e-005	0.0025	-8.1e-006	0.0011
-1	-0.0011	0.00039	-0.00012	0.0021	0.00033	0.0029	-0.00015	0.00044
0	0	0	0.0017	0.0021	0.00058	0.0029	0	1.5e-005
1	0.002	0.00033	0.00079	0.0024	0.0006	0.0028	-8e-005	0.00047
2	0.003	0.00048	-0.0021	0.0031	0.00058	0.0024	0.00015	0.00064
3	0.0043	0.00043	-0.0044	0.0037	0.00072	0.002	-0.00021	0.00041
4	0.0055	0.00067	-0.0061	0.0042	0.001	0.003	-0.00031	0.00079
6	0.0092	0.0013	-0.008	0.0033	0.0016	0.0081	0.00034	0.00071
8	0.015	0.0018	-0.0093	0.0026	0.0017	0.0095	0.00058	0.00043
10	0.024	0.0022	-0.009	0.0032	0.0025	0.013	0.0012	0.001
12	0.033	0.0033	-0.0095	0.0025	0.0026	0.014	0.002	0.0019
16	0.059	0.0093	-0.0069	0.0039	0.00027	0.022	0.0056	0.0083
20	0.16	0.0025	0.011	0.0077	-0.00054	0.039	0.0099	0.0086
25	0.24	0.0045	0.00096	0.007	-0.0011	0.038	0.013	0.0042

Table B.4: *Force coefficients for rigid cylinder and constant yaw angle, U=2.5 m/s*

α	C_n1	e_1	C_n2	e_2	C_n3	e_3	C_n4	e_4
-2	-0.0023	0.00041	-0.0042	0.0025	-0.00013	0.0022	-1.4e-005	0.00094
-1	-0.00098	0.0004	7e-005	0.0022	0.00023	0.0024	-0.00011	0.00038
0	0	0	0.0019	0.0021	0.00041	0.0024	0	8.2e-006
1	0.0019	0.00026	0.00081	0.0022	0.00043	0.0023	-5.4e-005	0.0005
2	0.0031	0.00039	-0.002	0.0031	0.00036	0.0021	-0.00013	0.00024
3	0.0042	0.00046	-0.0046	0.0039	0.00058	0.0022	-0.00024	0.00042
4	0.0052	0.00054	-0.0062	0.0044	0.00079	0.0034	-0.00024	0.00068
6	0.009	0.0011	-0.0089	0.0028	0.0011	0.0089	0.00037	0.00068
8	0.015	0.0019	-0.0097	0.003	0.0018	0.01	0.00048	0.00052
10	0.023	0.0023	-0.0092	0.0032	0.0024	0.014	0.0013	0.00091
12	0.033	0.0036	-0.01	0.0028	0.0026	0.014	0.002	0.0016
16	0.055	0.0031	-0.0092	0.002	0.00058	0.023	0.0039	0.0052
20	0.14	0.017	0.0088	0.015	0.0028	0.036	0.0048	0.0086
25	0.22	0.0058	-0.0062	0.016	-0.0015	0.042	0.012	0.0026

Table B.5: *Force coefficients for rigid cylinder and constant pitch angle, U=1.0 m/s*

α	C_{n2}	e_c [%]	C_{n3}	e_c [%]	C_{n5}	e_c [%]	C_{n6}	e_c [%]
0	-0.000653	-72.5	-0.000292	-175	-0.000326	26.2	-0.000162	-131
1	-0.000271	-618	-0.000193	-72.6	-0.000491	16.3	-0.000194	13.7
2	0.000912	149	0.000445	92.6	-6.23e-005	-322	-6.97e-005	-272
3	0.00144	5.81	0.00088	39.2	-2.04e-005	8.97	9.06e-005	-3.31
4	0.00266	39.7	0.0013	16	0.000111	-290	0.000272	-12.7
6	0.00627	7.28	0.00201	31	5.09e-006	5.18	0.00127	10.8
8	0.0113	3.09	0.00268	51.1	-0.000199	36.6	0.00161	15.2
10	0.0195	9.57	0.00284	43	-0.00091	54.2	0.00196	28.9
12	0.0314	5.2	0.00216	118	-0.00085	-9.15	0.00215	44.9

Table B.6: *Force coefficients for rigid cylinder and constant pitch angle, U=1.5 m/s*

α	C_{n2}	e_c [%]	C_{n3}	e_c [%]	C_{n5}	e_c [%]	C_{n6}	e_c [%]
0	-0.000416	-29.8	9.93e-005	287	-0.000208	-22.6	-6.06e-005	-74.3
1	5.81e-005	1.16e+003	-0.000113	-186	-0.000297	83.1	-7.56e-005	-13.6
2	0.000777	109	4.36e-005	706	-0.000274	115	-1.54e-005	594
3	0.0017	51.2	0.000187	372	-0.000205	170	5.64e-005	-147
4	0.00274	10.9	0.000465	179	-9.77e-005	72.9	0.000178	83.5
6	0.00608	9.31	0.000721	170	-0.000101	62.3	0.00077	58.2
8	0.0104	13.9	0.00161	136	-0.000147	143	0.00101	66.6
10	0.0165	5.21	0.00218	155	-0.00041	-13.6	0.00144	90.3
12	0.023	5.7	0.000977	472	-0.000677	-14.4	0.0017	123

Table B.7: *Peak to peak force amplitude for oscillating rigid cylinder.*

Tow Speed [m/s]	W_0 [m/s]	F_y [N]	e [N]	F_z [N]	e
0.0	0.15	0.44	0.32	1.00	0.13
	0.20	1.56	0.92	2.03	0.33
	0.25	2.84	1.45	3.38	0.82
	0.30	3.27	1.54	4.56	0.71
	0.35	5.51	2.92	6.20	0.79
	0.40	3.16	3.39	6.87	1.03
0.2	0.05	0.10	0.08	0.36	0.07
	0.10	0.14	0.17	0.62	0.08
	0.14	0.26	0.17	0.95	0.10
	0.18	0.59	0.34	1.41	0.12
	0.22	1.30	0.32	2.02	0.15
	0.26	1.92	0.84	2.76	0.29
	0.29	1.36	1.03	3.52	0.28
	0.32	1.12	0.49	4.27	0.32
	0.36	2.09	1.32	5.06	0.39
0.4	0.05	0.15	0.12	0.39	0.08
	0.10	0.14	0.09	0.66	0.09
	0.15	0.34	0.23	0.89	0.09
	0.19	0.39	0.17	1.45	0.12
	0.24	1.09	0.29	2.15	0.15
	0.28	1.86	0.64	2.96	0.16
	0.32	1.95	0.96	4.00	0.27
	0.36	1.92	0.79	5.04	0.29
0.6	0.05	0.21	0.10	0.72	1.07
	0.10	0.47	0.33	0.86	0.45
	0.15	0.30	0.18	0.98	0.34
	0.20	0.52	0.21	1.27	0.30
	0.24	1.12	0.27	1.87	0.16
	0.29	1.77	0.32	2.78	0.25
	0.33	2.27	0.43	3.87	0.24
	0.37	2.33	0.46	5.06	0.35
1.0	0.05	0.40	0.16	0.73	1.12
	0.10	0.61	0.93	0.77	0.30
	0.15	0.55	0.41	1.04	0.34
	0.20	0.67	0.43	1.28	0.19
	0.25	0.68	0.40	1.63	0.22
	0.29	0.77	0.65	1.92	0.21
	0.34	0.92	0.47	2.40	0.20
	0.39	1.22	0.42	3.21	0.22

Table B.8: *Peak to peak amplitude for oscillating flexible cylinder at $x/L = 0.77$. Forced amplitude at $x/L = 0$ is 0.01 m*

		y-direction		z-direction	
Tow Speed [m/s]	ω [rad/s]	$A_{pp\ y}$ [m]	e [m]	$A_{pp\ z}$ [m]	e [m]
0.0	2.4525	0.0075	0.0042	0.0237	0.0036
	6.2722	0.0036	0.0030	0.0082	0.0018
	9.5985	0.0038	0.0032	0.0029	0.0019
0.5	0.2109	0.0028	0.0011	0.0238	0.0006
	0.3187	0.0028	0.0013	0.0237	0.0015
	0.5841	0.0025	0.0014	0.0263	0.0006
	0.8402	0.0025	0.0013	0.0284	0.0006
	1.2122	0.0032	0.0017	0.0329	0.0006
	2.4505	0.0053	0.0040	0.0304	0.0033
	6.2768	0.0029	0.0024	0.0101	0.0020
	9.6008	0.0020	0.0021	0.0022	0.0013
	18.4638	0.0039	0.0035	0.0025	0.0019
1.5	0.2094	0.0040	0.0011	0.0249	0.0006
	0.2668	0.0060	0.0011	0.0278	0.0006
	0.5858	0.0051	0.0017	0.0312	0.0012
	0.8431	0.0042	0.0012	0.0324	0.0036
	1.2157	0.0052	0.0019	0.0352	0.0018
	2.4505	0.0044	0.0018	0.0290	0.0014
	6.2768	0.0016	0.0017	0.0097	0.0014
	9.6040	0.0010	0.0015	0.0029	0.0012
	18.4824	0.0028	0.0026	0.0017	0.0015
2.5	0.2094	0.0077	0.0011	0.0327	0.0006
	0.3142	0.0100	0.0011	0.0322	0.0006
	0.5843	0.0170	0.0011	0.0335	0.0006
	0.8422	0.0161	0.0022	0.0383	0.0014
	1.2215	0.0056	0.0024	0.0381	0.0026
	2.4510	0.0046	0.0027	0.0286	0.0013
	6.2808	0.0022	0.0021	0.0069	0.0037
	9.6193	0.0027	0.0023	0.0037	0.0013
	18.5405	0.0035	0.0022	0.0027	0.0021

PREVIOUS DR.ING. THESES

From the previous Department of Marine Hydrodynamics

Løtveit, Magne : A Study of Pressure- and Velocity Relations in the Slip-Stream of Propellers of Single Screw Ships to clarify the Propeller Action behind the Hull. 1963. (in Norwegian)

Dahle, Emil Aall : A Study of the Coefficients in the Differential Equations for the Rolling Motion of a Vessel. 1971. (in Norwegian)

Langfeldt, Jan N. : A Theoretical and Experimental Study of the Feasibility of Two-Phase (Gas-Water) Jet Propulsion of Craft. 1972.

Berg, Tor Einar : Manoeuvring of Vessels. 1978. (in Norwegian)

Skjørdal, Svein O. : Wave Induced Oscillations of Ship Hulls. 1978.

Nielsen, Finn G. : Hydrodynamic Relations of Oil Booms. 1980.

Liapis, Nicolas : Hydrodynamic Analysis of the Ship-Buoy System. 1980.

Pettersen, Bjørnar : Calculation of Potential Flow about Ship Hulls in Shallow Water with Particular Application to Manoeuvring. 1980.

Rye, Henrik : Ocean Wave Groups. 1981.

Utnes, Torbjørn H. : Forward-Speed Effects on the Hydrodynamic Motion Coefficients of a Surface-Piercing Body. 1982

Børresen, Rolf : The unified theory of ship motions in water of finite depth. 1984.

Aarsnes, Jan Vidar : Current Forces on Ships. 1984.

Skomedal, Nere : Application of a Vortex Tracking Method to Three-Dimensional Flow Past Lifting Surfaces and Blunt Bodies. 1985.

Løken, Arne Edvin : Three-dimensional second order hydrodynamic effects on ocean structures in waves. 1986.

Aanesland, Vidar : : A Theoretical and Numerical Study of Ship Wave Resistance. 1986.

Sortland, Bjørn : Force Measurements in Oscillating Flow on Ship Sections and Circular Cylinders in a U-Tube Water Tank. 1986.

Falch, Sigurd : A numerical study of slamming of two-dimensional bodies. 1986.

Lian, Walter : A numerical study of two-dimensional separated flow past bluff bodies at moderate KC-numbers. 1986.

Braathen, Arne : Application of a vortex tracking method to the prediction of roll damping of a two-dimensional floating body. 1987.

Gang Miao : Hydrodynamic Forces and Dynamic Responses of Circular Cylinders in Wave Zones. 1989.

Greenhow, Martin : Linear and Non-Linear Studies of Waves and Floating Bodies. Part I and Part II. 1989.

Chang Li : Force Coefficients of Spheres and Cubes in Oscillatory Flow with and without Current. 1989.

Jæger, Arild : Seakeeping, Dynamic Stability and Performance of a Wedge Shaped Planing Hull. 1989.

Hoff, Jan Roger : Three-dimensional Green function of a vessel with forward speed in waves. 1990.

Rong Zhao : Slow-Drift of a Moored Two-Dimensional Body in Irregular Waves. 1990.

Løland, Geir : Current Forces and Flow through Fish Farms. 1991.

Krokstad, Jørgen R. : Second-order Loads in Multidirectional Seas. 1991.

Mørch, Hans J. B. : Aspects of Hydrofoil Design; with Emphasis on Hydrofoil Interaction in Calm Water. 1992.

Steen, Sverre : Cobblestone Effect on SES. 1993.

Kvålsvold, Jan : Hydroelastic Modelling of Wetdeck Slamming on Multihull Vessels. 1994.

Ulstein, Tore : Nonlinear Effects of a Flexible Stern Seal Bag on Cobblestone Oscillations of an SES. 1995.

Solaas, Frøydis : Analytical and Numerical Studies of Sloshing in Tanks. 1995.

Bratland, Anne K. : Wave-Current Interaction Effects on Large-Volume Bodies in Water of Finite Depth. 1995.

Herfjord, Kjell : A Study of Two-dimensional Separated Flow by a Combination of the Finite Element Method and Navier-Stokes Equations. 1995.

Pedersen, Egil : A Nautical Study of Towed Marine Seismic Streamer Cable Configurations. 1996.

Hansen, Edmond H. : A Discrete Element Model to Study Marginal Ice Zone Dynamics and the Behaviour of Vessels Moored in Broken Ice. 1998.

Haugen, Elin Marita : Hydroelastic Analysis of Slamming on Stiffened Plates with Application to Catamaran Wetdecks. 1999.

Tønnessen, Rune : A Finite Element Method Applied to Unsteady Viscous Flow Around 2D Blunt Bodies with Sharp Corners. 1999.

Haslum, Herbjørn Alf : Simplified Methods Applied to Nonlinear Motion of Spar Platforms. 2000.

Baarholm, Rolf Jarle : Theoretical and experimental studies of wave impact underneath decks of offshore platforms. 2001.

Greco, Marilena : A Two-Dimensional Study of Green-Water Loading. 2001.

Holmedal, Lars Erik : Wave-current interactions in the vicinity of the sea bed. 2002.

Rognebakke, Olav : Sloshing in rectangular tanks and interaction with ship motions. 2002-

Lader, Pål : Geometry and Kinematics of Breaking Waves. 2002.

Yang, Qinzheng : Wash and wave resistance of ships in finite water depth. 2002.

Ronæss, Marit : Wave Induced Motions of Two Ships Advancing on Parallel Course. 2002.

Chezhian, Muthu : Three-Dimensional Analysis of Slamming. 2003

Tregde, Vidar : Aspects of Ship Design; Optimalization of Aft Hull with Inverse Geometry Design . 2004

Wist, Hanne Therese : Statistical Properties of Successive Ocean Wave Parameters. 2004.

Ransau, Samuel : Numerical Methods for Slows with Evolving Interfaces. 2004.